

TRANSPORT AND THERMODYNAMICS OF WATER IN THE BIOSPHERE

A Dissertation

Presented to the Faculty of the Graduate School

of Cornell University

In Partial Fulfillment of the Requirements for the Degree of

Doctor of Philosophy

by

Michael Santiago

August 2016

© 2016 Michael Santiago

TRANSPORT AND THERMODYNAMICS OF WATER IN THE BIOSPHERE

Michael Santiago, Ph.D.

Cornell University 2016

Plants carry water through xylem, a vascular network that consists of low-resistance channels interconnected by high-resistance nanoporous membranes. We model how electrokinetic effects in the nanopores influence overall xylem hydraulic conductance, with respect to the concentration and identity of ions present in the perfusing water. Using published data on membrane composition and physiological values of ionic concentration, we predict that xylem hydraulic conductance changes nonmonotonically with ionic concentration; this effect can reduce conductance by up to 18% and is compatible with published experimental data. We propose experiments aimed at distinguishing electrokinetic effects from other proposed mechanisms.

In a wetted porous material, the curved meniscus at the liquid-vapor interface can hold a pressure difference and allow the liquid phase to (1) drop to pressures below zero—be under mechanical tension, and (2) equilibrate with subsaturated phases. Using this principle, we built a microfabricated device to place liquids under tension and measure their pressure. The device, called a microtensiometer, consists of a liquid reservoir that connects to the sensed environment through a nanoporous membrane, and a pressure-sensing diaphragm that measures the reservoir pressure. It was used to measure the cavitation pressures of water, acetone and methanol, and the water equation of state down to -15 MPa.

The microtensiometer was further miniaturized and packaged to become an in situ probe for water potential. Water potential measures the availability of water for physical and chemical processes. The probe was tested in 3 contexts: osmotic solutions, soil samples, and living plants. In osmotic solutions, the sensor measured water potential to an accuracy of ± 0.3 MPa. In soil, the use of microtensiometers in the Wind/Schindler evaporation method allowed for measurement of water retention curves over an unprecedented range of water potential. In an apple stem, the sensor measured the correct trend over the course of 10 days, but tensions measured were 2-4 times higher compared to the pressure bomb, possibly due to sensor-xylem temperature gradients.

BIOGRAPHICAL SKETCH

Michael was born and raised in Puerto Rico. He received a bachelor's degree in Mechanical Engineering from the University of Puerto Rico, Mayagüez. During this time, Michael interned at the National Institute of Standards and Technology, the University of Wisconsin at Madison, the Massachusetts Institute of Technology Sloan Automotive Lab, and the US Forest Service Airfire division. In the fall of 2010, he entered Cornell University to pursue a PhD in Mechanical and Aerospace Engineering. Michael is an Alfred P. Sloan fellow, and a National Science Foundation GRFP fellow.

Esta disertación va dedicada a mi bella y preciosa familia. Mil gracias por su apoyo. Y a Misty!

Espero podamos hablar español mas a menudo 😊

ACKNOWLEDGEMENTS

Thanks to National Science Foundation and Alfred P. Sloan foundation for support for these 6 years as a PhD. Also thanks to the entrepreneurship community here for introducing me to the world of business, including Tom Schryver, Brad Treat, Ken Rother, Steven Gal and Peter Cortle. Thanks to all the lab members of the Stroock group that I have collaborated with in one way or another. Past and present. David Sessoms, Vinay Pagay, Eugene Choi, I-tzu Chen, Erik Huber, Winston Black, Siyu Zhu, Hanwen Lu, William Bedell, Olivier Vincent, John Morgan, Anthony Diaz. Finally, thank you Misty for the unconditional support these (many) years. We are finally going to live together!

TABLE OF CONTENTS

1	Introduction.....	1
	Metastable phases of water	1
	Anomalies in water	1
	Water in porous materials	3
	Water potential.....	3
	Sensing water potential	5
	Bringing it all together: transport of water in xylem	5
	Study objectives and approaches	8
2	Impact of electroviscosity on the hydraulic conductance of the bordered pit membrane: a theoretical investigation.....	10
	Introduction.....	10
	The ionic effect: BPM-mediated response of xylem conductance to sap composition.....	11
	Current models of flow regulation through BPMs	12
	Motivation and overview	16
	Theory.....	17
	Surface electric charge and potential	17
	Electrokinetic matrix.....	20
	Electroviscosity.....	21
	Results.....	22
	Conductance as a function of ionic strength, density of chargeable sites and pore size	23
	Comparison to experiments: conductance vs. ionic strength.....	25
	Conductance as a function of pH and ionic strength	27
	Conductance as a function of ion identity and ionic strength.....	29
	Discussion.....	30
	Proposed experiments	32
	Ecophysical Implications	34
	Conclusions.....	35
	Methods	36
	Analytical approximation & numerical solution of $\varphi(r)$	39
	Zeta potential and surface charge	39
	Determination of Γ from experimental measurements	40
	Electroviscosity in nanochannels.....	42
	Acknowledgements.....	45
3	Microlaboratory to manipulate and study liquids at negative pressure	46
	Introduction.....	46
	Analysis of device.....	51
	Metastable vapor liquid equilibrium.....	51
	Nucleation mechanisms	52
	Channel structure and equilibration time.....	54
	Materials and methods.....	56

	Fabrication, calibration and use of sensor.....	56
	Measurement of liquid cavitation pressure.....	58
	Measurement of water EoS.....	58
	Calculation of IAPWS plot.....	60
	Results and discussion.....	62
	Cavitation pressure.....	62
	Equilibration time.....	64
	Measurements of water EoS.....	66
	Challenges and future work.....	69
	Acknowledgements.....	70
	Supplementary information.....	71
	Uncertainty Analysis.....	71
	Porosimetry.....	75
	Equation of state measurement data.....	75
4	Microtensiometer probe for in situ water potential measurements of complex media: solutions, soils, plants.	77
	Introduction.....	77
	Components of and instruments to measure water potential.....	81
	Methods.....	86
	Brief introduction to tensiometry.....	86
	Pressure diaphragm sensitivity.....	89
	Diaphragm breaking pressure.....	92
	Pressure equilibration time.....	92
	Diaphragm capacitance.....	93
	Porous membrane resistance and xylem-mimetic channels.....	94
	Platinum wiring.....	96
	Microfabrication.....	98
	Measurement in osmotic solutions.....	102
	Measurement in soil.....	103
	Measurement in plants.....	104
	Results and discussion.....	105
	Sensor characteristics.....	105
	Osmotic solutions.....	109
	Soils.....	111
	Plants.....	113
	Discrepancies in plant measurements.....	117
	Conclusions.....	121
	Acknowledgements.....	122
	Supplementary.....	123
5	Conclusion.....	124
	Limitations of the research.....	125
	Implications.....	126
6	Appendix.....	128
	Microtensiometer mask images.....	128

Microtensiometer process flow.....	132
7 References.....	139

LIST OF FIGURES

Figure 1.1: Predicted coexistence of two liquid phases in supercooled water.....	2
Figure 1.2: Dependence of fruit properties on water potential.	4
Figure 1.3: Vulnerability of plants to environment changes in water availability.....	5
Figure 1.4: Structure of the vascular network of plants.....	6
Figure 1.5: Osmotic refilling as a proposed mechanism for embolism repair in grapevine xylem.	7
Figure 2.1: Water transport through xylem.....	11
Figure 2.2: Hydrogel hypothesis as proposed by Zwieniecki et al. ⁵³	14
Figure 2.3: Idealized model of a BPM pore.....	19
Figure 2.4: The electroviscous effect.....	22
Figure 2.5: Relative conductance (K / K^0) vs. ionic strength for 1-10 nm pores, and density of chargeable sites Γ_{high} (A) and Γ_{low} (B).....	24
Figure 2.6: Relative hydraulic conductance (K_{xylem} / K_{xylem}^0) vs. ionic strength (I_c) for our theoretical predictions, van Doorn’s model, and published experimental data.	27
Figure 2.7: Relative hydraulic conductance (K / K^0) and zeta potential (ζ) vs. fluid pH in the BPM, for various ionic strengths.	28
Figure 2.8: Relative hydraulic conductance (K / K^0) vs. ionic strength for an electrolyte with monovalent cations (A) or divalent cations (B).....	30
Figure 3.1: Schematic diagram showing the metastable extensions of the phase diagram of water.	48
Figure 3.2: Microtensiometer sensor.	50
Figure 3.3: Cartoon representation of the measurement principle of our system: metastable vapor-liquid equilibrium.	52
Figure 3.4: Experimental setup to measure water equation of state.	61
Figure 3.5: Representative run of equation of state measurements ($P(a, T)$).....	61
Figure 3.6: Cavitation pressure of different liquids in tensiometer.	64

Figure 3.7: Comparison of equilibration time for a typical bare (black) and channeled (red) porous silicon device	66
Figure 3.8: Experimental measurements of water equation of state.	69
Figure 3.9: Porosimetry data on sample of porous silicon membrane used in microtensiometers for equation of state measurements.	75
Figure 4.1: Water potential (Ψ) in natural and technological contexts.	80
Figure 4.2: Illustration of conventional tensiometer and microtensiometer.	89
Figure 4.3: Xylem-mimetic channel network.	97
Figure 4.4: Sensor fabrication, simplified process flow.	102
Figure 4.5: Calibration data for sensor in pressure chamber	107
Figure 4.6: Microtensiometer equilibration time.	107
Figure 4.7: Calibration data for sensor platinum resistance thermometer (PRT).	109
Figure 4.8: Measurements of PEG 1450 MW osmotic solutions with microtensiometer.	111
Figure 4.9: Measurement of soil water retention curve using Wind/Schindler evaporation method with microtensiometers.....	113
Figure 4.10: Measurement of apple stem water potential (Ψ , solid red line) and temperature (T , solid blue line) compared with solar radiation data (solid black line).....	114
Figure 4.11: Measurements in apple and grape trunks over first day.....	116
Figure 4.12: Effect of stem-sensor temperature lag on water potential measurements.	121
Figure 4.13: Detailed sensor fabrication process flow.....	123
Figure 6.1: Water cavity with xylem structure (dark green). Patterned porous Si layer (transparent grey).....	128
Figure 6.2: SiO ₂ insulation (transparent blue) and polySi (red).....	129
Figure 6.3: Platinum wires (solid grey) and VIA openings (green).	130
Figure 6.4: Full wafer mask with all devices.	131

LIST OF TABLES

Table 2.1: Maximum values of surface potential (ζ) reported for plant materials.	17
Table 2.2: Parameters used in the analysis.	44
Table 2.3: Electrophoretic mobility of ions used in analysis.	44
Table 3.1: Cavitation data and comparisons with classical nucleation theory.	64
Table 3.2: Predictions and measured equilibration time constants (eq. 3.15) for plain devices and channeled devices.	66
Table 3.3: Comparison of EoS slope measured with IAPWS extrapolated values.	69
Table 3.4: Properties assumed in uncertainty analysis	71
Table 3.5: Sources of error in the system, from manufacturer data.	71
Table 3.6: Uncertainties calculated.	72
Table 3.7: Chi-squared for measurements at each temperature.	75
Table 3.8: Raw data of equation of state measurements.	76
Table 4.1: Comparison of instruments available to measure water potential (Ψ).	85
Table 4.2: Comparison of diaphragm sensitivity, equilibration time, and breaking pressure. ...	108

CHAPTER 1

INTRODUCTION

The macroscale, even planetary scale movement of fresh water is determined by its nanoscale interactions with and properties within porous materials. In the hydrological cycle, water moves downward by percolation through porous soil to underground rivers or travels on top as surface runoff; it moves upward by evaporation at the soil surface or by transpiration through the porous vascular system of plants. Water in these systems affects the viability of agricultural crops¹, the spread of contaminants², and the properties of the land itself³. In technological contexts, the presence of water affects the shrinkage and cracking of concrete⁴ and the texture⁵, aroma⁶ and shelf life⁷ of foods. It is thus important to understand the properties of water and the interactions that govern its behavior in porous systems.

Metastable phases of water

Liquid water at atmospheric conditions generally boils at 100 °C and freezes at 0 °C. In the absence of nucleation sites, it can be metastable and exist beyond these limits: liquid water can be superheated to 280 °C before boiling⁸, or supercooled near -42 °C before crystallization⁹. Liquid water can also be metastable with respect to pressure. Because liquids have attractive molecular forces, their pressure can drop below zero, where the liquid is under mechanical stress, or tension. In this case, if the tension is too large, the liquid will cavitate or boil and a bubble forms.

Anomalies in water

Water is an unusual liquid, and displays many anomalous properties when compared to other simpler liquids. Anomalies include the apparent divergence of the isothermal compressibility,

isobaric heat capacity and thermal expansion coefficient as the liquid is supercooled toward its homogeneous freezing temperature, $-42\text{ }^{\circ}\text{C}$ ¹⁰. It has been proposed that these divergences could be due to a second critical point where two different liquid ‘phases’ coexist¹¹. Computational models of water disagree on whether this critical point exists: Figure 1.1 shows a computational model that has a second critical point, but others argue that this finding is a computational artifact¹². Another open question on water is why the cavitation pressure of water, the pressure at which the liquid cannot hold more tension and breaks, theoretically should be around -140 MPa at 300 K , but only one experimental setup gets to these high tensions (mineral inclusions)¹³, whereas other methods only show values above -30 MPa ¹⁴. Thus metastable states are interesting to study because they shed light on the structure and behavior of water, and may eventually find or disprove the putative liquid-liquid critical point.

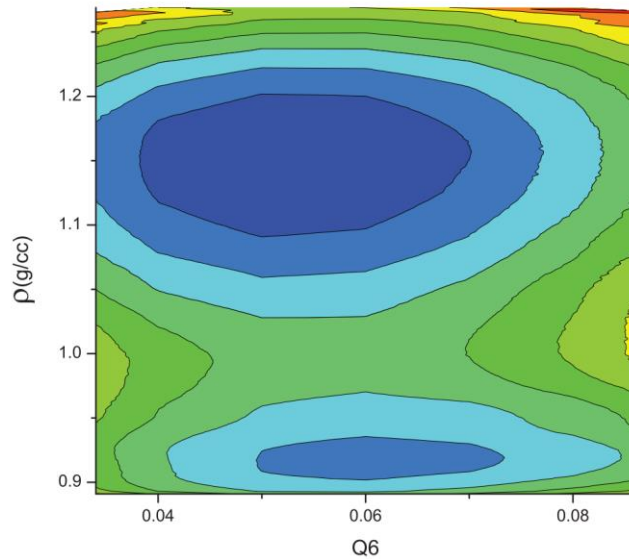


Figure 1.1: Predicted coexistence of two liquid phases in supercooled water. ST2 computational model of water shows coexistence of two distinct liquid phases with different densities in highly supercooled conditions. Plot shows free energy surface for plane of density (ρ) and an order parameter (Q_6) at $-44.5\text{ }^{\circ}\text{C}$ and 220 MPa . Reproduced from Liu et al.¹⁵

Water in porous materials

Porous materials allow liquid water to behave in ways not common macroscopically. The large surface to volume ratio within porous media means that interactions between the liquid and solid become dominant. For instance, water will ‘climb’ against gravity in a porous material because the solid material has a higher affinity for water than for the surrounding gas. Water will also preferentially condense first in smaller pores, a phenomena known as capillary condensation¹⁶. Of particular interest is that porous materials allow liquid water to exist at pressures below the surrounding pressure, even to the point of being under mechanical tension. This reduction in pressure is enabled by the meniscus that forms at the mouth of a pore: its curvature and surface tension holds the difference in pressure between the pore and the surrounding environment. This process is called meniscus pinning. Furthermore, interconnected pores produce hysteresis in the drying and wetting of porous materials¹⁷, and allow vapor and liquids under tension to coexist in the same matrix, unlike in a macroscopic container where one cavitation event precludes all the liquid volume from holding tension.

Water potential

The movement of water in porous media occurs along gradients of chemical potential or water potential. Water potential, Ψ , represents chemical potential in pressure units and is the preferred representation in plant science and hydrology. For instance, a gradient in water potential between the soil and the atmosphere drives flow through the plant xylem. This quantity includes the energies associated with all the forces that determine the movement of water, such as matric interactions, pressure, osmotic gradients, gravity, and electric forces. In a plant, water potential is influenced by the atmospheric humidity and temperature, the soil water content and salinity, and

the depth and locations of roots. In effect, water potential determines the availability of water for chemical and physical processes.

Water potential is the best measure of hydration in plants¹⁸ and soil water availability. It heavily influences produce quality, and defines the threshold for plant survival. For instance, grapevine water potential affects vegetative structures, berry growth, yield, fruit composition and final wine color¹⁹ (see Figure 1.2); water potential is also the best indicator for regulated deficit irrigation²⁰. Plants have developed complex mechanisms to deal with low water potentials²¹, though many plants may live close to the limit of the water stress they can sustain (see Figure 1.3).

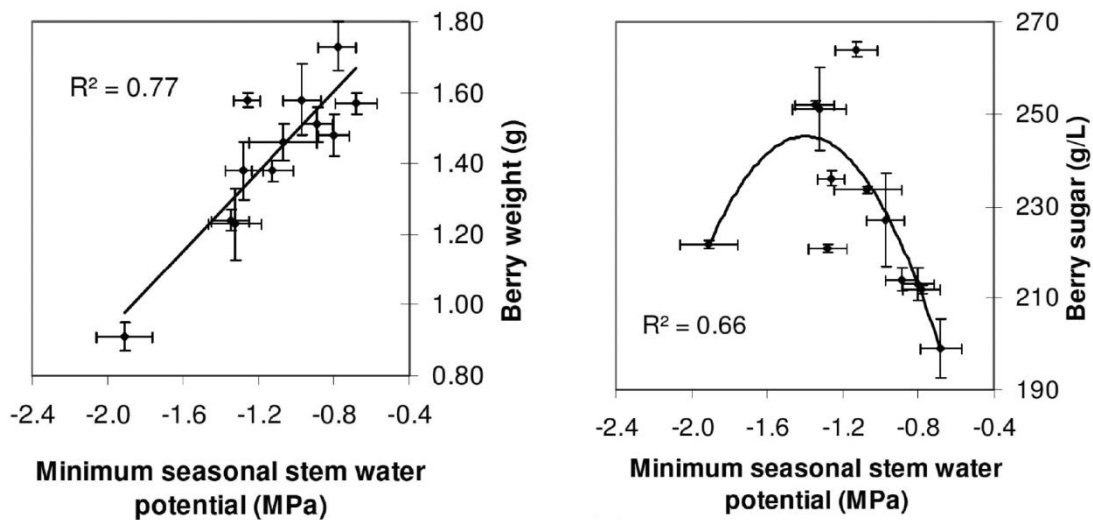


Figure 1.2: Dependence of fruit properties on water potential. Grape weight and sugar content depend on water potential (*Vitis vinifera* L. cv. Merlot, 2004-2007, Bordeaux). Figure modified from Leeuwen et al.²²

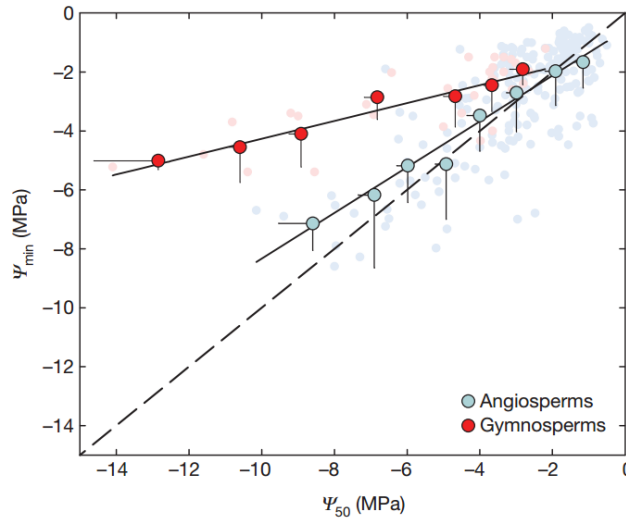


Figure 1.3: Vulnerability of plants to environment changes in water availability. Minimum xylem water potential measured in natural environment (Ψ_{min}) vs embolism resistance (Ψ_{50} , water potential that causes a 50% loss of conductivity) for variety of angiosperms and gymnosperm plants. Many of the species shown experience water potentials dangerously close to Ψ_{50} . Figure reproduced from Choat et al.²³

Sensing water potential

The term water potential was first explained in 1907, by Edgar Buckingham, in trying to describe the movement of water in unsaturated soil^{24,25}, but Buckingham had no way to measure Ψ . The term was a theoretical construct until the concept was implemented by Burton E. Livingston in the first instrument to measure Ψ —the tensiometer²⁶. Since then, instruments to measure water potential in the field have been used extensively in both research and applications in plant science, agriculture and hydrology, but have been hampered by poor range and low accuracy.

Bringing it all together: transport of water in xylem

A particularly important example of water in porous materials is the vascular network of plants: nature's finely tuned porous network (see Figure 1.4). During transpiration, plants transport water

from the roots to the leaves, powered by a gradient in water potential between the soil and the atmosphere. Water is transported through xylem, the vascular network of plants, a finely tuned porous material designed to transport and manage water under tension. Xylem has a bimodal pore structure that consists of large 10 – 50 μm vessels interconnected through nanoporous membranes known as pits. This structure minimizes the resistance to flow by moving liquid through large, high conductance vessels over macroscopic distances and through nanoporous membranes over microscopic distances, but also prevents cavitation events, or embolisms, from spreading in the xylem and stopping flow altogether. Although liquid water can travel through the pit membranes, gases cannot because of capillary pinning. Water in xylem is commonly found at negative pressures, and can reach pressures below -22 MPa in some desert plants²⁷. Under prolonged drought, vessels in the xylem cavitate (embolize), prevent the flow of water, and decrease the hydraulic conductance of the plant.

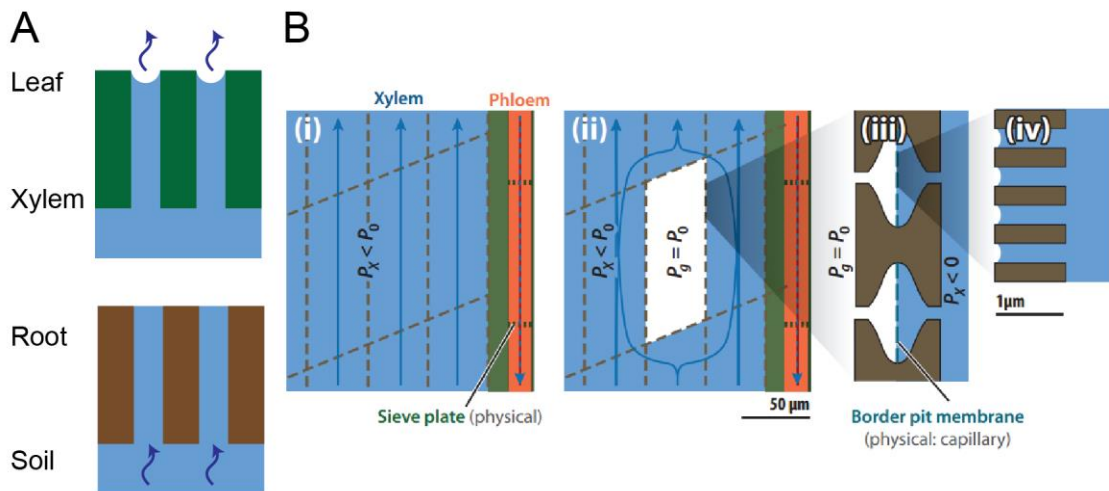


Figure 1.4: Structure of the vascular network of plants. (A) Water travels from the soil to the roots, through the xylem network and finally evaporates from the leaves. (B) The xylem network is composed of vessels interconnected by bordered pit membranes. The pit membranes allow passage of liquid, but not of gas. Figure modified from Stroock et al.²⁸

One open question is how do plants prevent and repair embolisms. There are suggestions that plants may be able to refill embolized vessels, even while transpiring water under tension²⁹. Particularly, recent synchrotron measurements show the spread of embolisms³⁰ and refilling of embolisms³¹ in vivo. However, how do plants reconnect the embolized vessel without the water being pulled by a nearby vessel under tension? How do they get rid of the gas or dissolve it? One proposed explanation is osmotic refilling, where cells surrounding a cavitated vessel secrete osmolites that drive water into the vessel and refill it (Figure 1.5). This problem is difficult to study in a complex living system, but it may be possible to study it in synthetic systems, such as synthetic trees³².

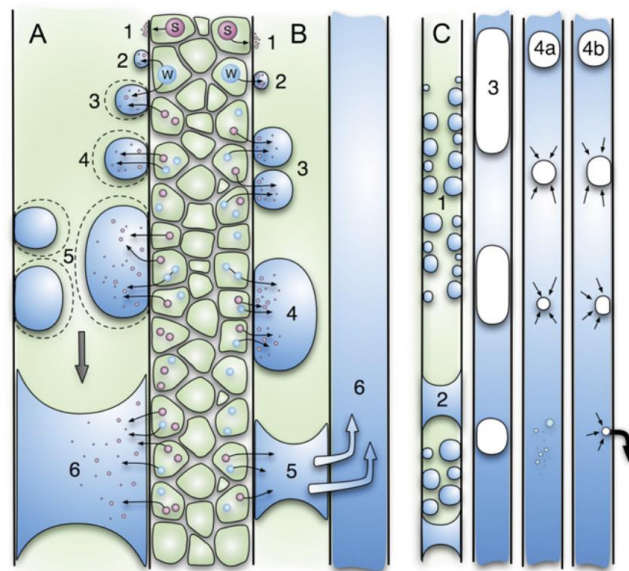


Figure 1.5: Osmotic refilling as a proposed mechanism for embolism repair in grapevine xylem. (A) Cells surrounding an embolized vessel secrete solutes that lower the water potential in said vessel, and drive water flow to refill it. (B) If the refilling water contacts a nearby vessel that is under tension, it will be sucked away. (C) Refilling continues until the whole vessel is full and the remaining vapor is dissolved or escapes through the vessel wall. Figure reproduced from Brodersen et al.³¹

Study objectives and approaches

Given the importance of water in natural and technological contexts involving porous media, in the studies presented here we focused on developing tools to better understand water, its interactions with porous materials, and its availability (water potential).

In chapter 2 we investigate the magnitude of the electrokinetic effects, specifically in plant xylem. We ask: do these effects make a measurable difference in the xylem water transport? Can plants use them to improve drought resistance? Can experiments differentiate between electrokinetic effects and other proposed hypotheses? Using published experimental data on the characteristics of xylem, we develop a model of electroviscosity in the xylem porous network, predict the maximum electrokinetic-derived decrease in flow and compare our predictions with published data.

In chapter 3 we use the fact that porous materials can hold liquids under tension to construct a sensor system that can place and hold a macroscopic volume of liquid under a desired amount of tension, and simultaneously measure its properties. We use this system to measure the properties of water under tension and measure the cavitation pressure of acetone, methanol and water. We analyze what causes cavitation in our system. This system can serve as a base to study other properties of liquids under tension.

In chapter 4 we use the principle of metastable vapor liquid equilibrium to go from measuring the properties of water under tension to instead have a sensor that measures water status (water potential) in complex systems such as soil and plants. The sensor created enables gathering

information on scientific questions about flow in complex media. It also serves as a technological breakthrough, allowing large range and high accuracy measurements of water potential. It can measure water potential to -8 MPa in field conditions and might enable new science insights into plant water relations and commercial applications in agriculture and industry.

CHAPTER 2

IMPACT OF ELECTROVISCOSITY ON THE HYDRAULIC CONDUCTANCE OF THE BORDERED PIT MEMBRANE: A THEORETICAL INVESTIGATION

Plant Physiology **2013**, *163*, 999–1011. Copyright American Society of Plant Biologists.

Introduction

During transpiration, sap flows along a gradient in water potential through the vascular conduits of xylem (Fig. 1A), moving both axially through tracheids and vessel elements of macroscopic cross-section (10-700 μm in diameter), and transversally through intertracheid and intervessel structures known as bordered pits (Fig. 1 B-D)³³. In this vascular network, pits can contribute more than 50% of xylem's total hydraulic resistance^{34,35}. Pits in angiosperms comprise a nano-porous membrane—the bordered pit membrane (BPM)—enclosed by a channel that connects two xylem vessels; this membrane is formed from the primary cell wall and intervening middle lamella³⁶, and is covered by a matrix of thin, plaque-like material of unknown composition³⁷ (Fig. 1C, D). Pits redistribute flux to bypass immature vessels in young shoots³⁸ and local emboli (Fig. 1B)³⁹, and function as valves between adjacent vessels, allowing the passage of sap while preventing the spread of embolisms⁴⁰⁻⁴² and pathogens⁴³. Pit characteristics also play a role in poorly understood phenomena, such as how embolisms spread between vessels⁴⁴, and how vessels are actively refilled, i.e. during transpiration,⁴⁵. Although pits are ubiquitous, it is hard to study their characteristics directly because of their small size; therefore, indirect methods such as stem perfusion experiments are often used.

Figure 1

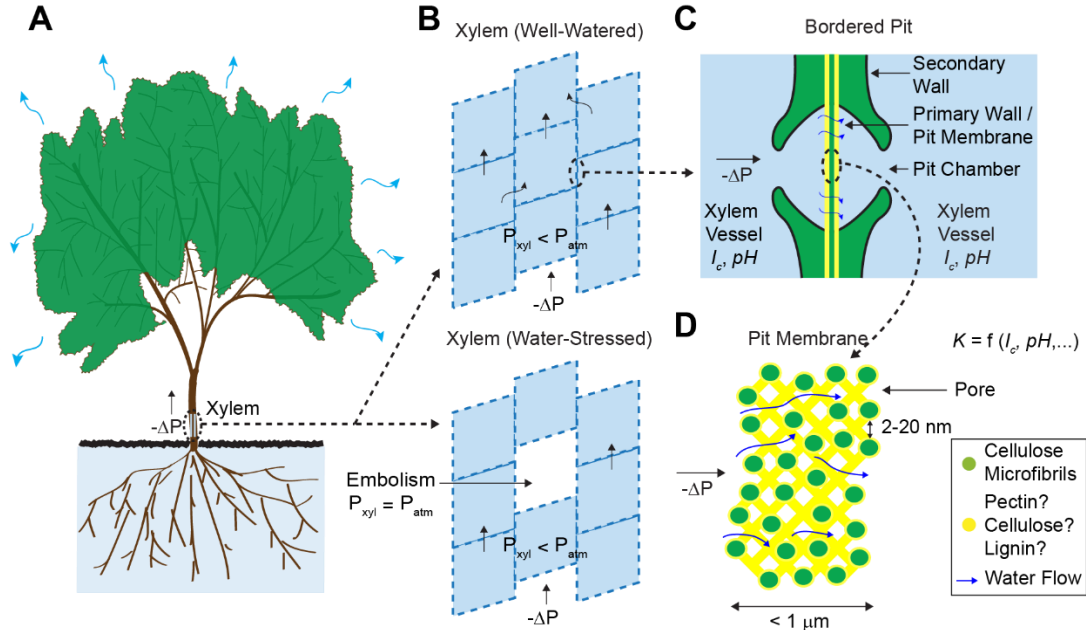


Figure 2.1: Water transport through xylem. (A) Global view. (B) Segmented architecture of xylem, with both axial and radial flow of sap. (C) Cross-sectional view of a pit and its membrane. (D) Cross-sectional view of the BPM, and its interconnected pore network through which sap flows. The effective hydraulic conductance of an individual pore (K) depends on its own properties and those of the sap.

The ionic effect: BPM-mediated response of xylem conductance to sap composition

Experiments over the previous three decades have challenged the view that xylem forms an inert conduit whose structure solely determines its sap-carrying characteristics; these experiments have provided clues as to the structure and possible functions of pits in regulating flow. The conductance of xylem (K_{xylem}) has been shown to change rapidly in response to changes in the composition of sap. To the best of our knowledge, Zimmermann⁴⁶ first reported this phenomena. In a study on stem segments of sugar maple (*Acer saccharum* Marsh.), he found that K_{xylem} decreased more than 50% upon initial perfusion with distilled water and returned to its original value upon perfusion with tap water or upon reversal of direction of flow. More recent studies using well-defined aqueous solutions confirm that K_{xylem} may vary in response to changes in fluid ionic strength (I_c

)^{34,35,47–54}, composition with respect to specific cations^{53–55}, pH⁵³, and concentration of proteins and polysaccharides⁵⁶. Further studies indicate that the magnitude^{53,57} and direction^{54,58} of the change in K_{xylem} depend on the species studied and the range of I_c considered. Here, we refer to this overall phenomenon as the ‘ionic effect’. In *Laurus nobilis*, perfusion experiments through segments with and without passages through pits suggest that these changes are mediated by pits⁵³.

Although experiments on stem segments clearly show the ionic effect, questions remain as to whether it occurs *in planta*, its possible physiological role, and its mechanism. Studies suggest that plants may exploit the ionic effect to regulate K_{xylem} actively by exchanging ions between xylem and phloem⁵⁹, a mechanism that may help maintain flow in the presence of emboli⁶⁰. Still, concerns exist that the ionic effect may be an experimental artifact due to the use of deionized water, an artificial fluid devoid of ions normally present in sap^{61,62}. This fluid can permanently decrease K_{xylem} in stem segments and decrease fresh weight in cut flowers⁵⁷.

Notwithstanding whether this effect occurs *in vivo*, here we explore why it happens and what it reveals about the structure and function of pits. Let us now introduce two mechanisms previously proposed to explain the ionic effect: (1) the swelling and shrinking of hydrogels within the BPM, and (2) electroviscosity in the pores of the BPM.

Current models of flow regulation through BPMs

BPM swelling-shrinking hypothesis

Zimmermann⁴⁶ suggested that the ionic effect could be caused by the swelling or shrinking of hydrogels covering the surface of BPM pores. Swelling could decrease the size of pores traversing

the BPM, thus decreasing the pit conductance (K) and therefore K_{xylem} as well (Figs. 1D and 2A). This swelling-shrinking behavior of the BPM was later attributed to the Donnan effect that describes changes in the hydration status of polyelectrolytic gels (e.g. pectin)⁵⁸. At low I_c , polyelectrolyte gels swell because of the long-range repulsion between bound charges. In the architecture suggested in Figs. 1D and 2, this swelling could reduce the effective hydrodynamic radii of pores in the BPM (Figs. 1D and 2A), decreasing K . At high I_c , polyelectrolyte gels collapse because ions in the fluid screen the bound charges and reduce the distance over which their mutual repulsion acts; this shrinking could increase the effective pore radius (Fig. 2B), increasing K . This model can also explain the observed response to pH: at high pH, the number of charged groups in the gel increases because more bound acids deprotonate, the gel swells, and K decreases; at low pH, the acids are neutralized, the gel collapses, and K increases. Lee et al.⁶³ observed a swelling-shrinking response to changes of ionic strength on individual BPMs of tobacco plants (*Nicotiana tabacum* L.) using an atomic force microscope. We note though, that based on their observations, they suggest an alternative architecture to the one shown in Fig. 2: rather than gel lining the pores in the membrane, they suggest a layer of gel on the surface of the membrane. We are not aware of a simple explanation for how the swelling of the gel in this alternative architecture would affect the conductance of the membrane.

The gel-swelling hypothesis is incompatible with some observations. First, in some species, K_{xylem} has been observed to decrease as I_c increases⁵⁸, a behavior opposite of that predicted. Second, various studies question whether pectin hydrogels actually exist in the BPM, as reviewed by van Doorn et al.⁶⁴. Third, uncertainties about the distribution of the gels within the membrane make it

difficult to predict how swelling should impact conductance⁶³. These arguments suggest that we may need to invoke other phenomena to explain the ionic effect.

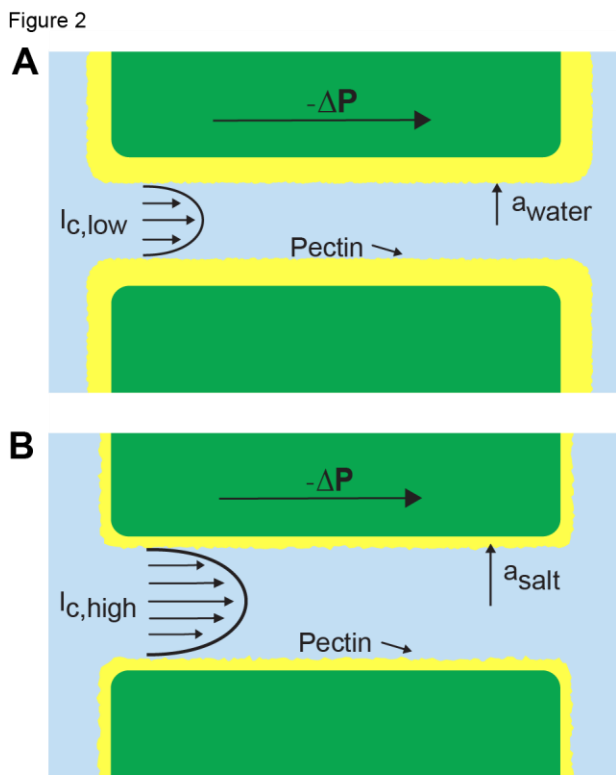


Figure 2.2: Hydrogel hypothesis as proposed by Zwieniecki et al.⁵³. (A) When deionized water ($I_{c,low}$) flows through a BPM pore, the pectin layer swells, decreasing both the effective pore radius (a_{water}), and the overall conductance. (B) When an ionic solution flows, e.g. KCl ($I_{c,high}$), the pectin layer shrinks, increasing both the effective pore radius ($a_{salt} > a_{water}$) and the overall hydraulic conductance.

Electrokinetic flow model

Under equivalent conditions, liquid flow through an electrically charged channel is always less than flow through an uncharged one⁶⁵. This effect is often called the electroviscous effect, or electroviscosity, because the viscosity of the fluid appears to increase. In reality, electroviscosity is an electrokinetic effect in which ions in the fluid cause the observed change in conductance⁶⁶.

Electroviscosity occurs as follows: (1) when submerged in water, most materials develop a net ionic charge on their surface due to the exchange of ions with the solution; (2) this surface charge then attracts counter-ions from the liquid and creates a layer of mobile net electric charge in the fluid near the surface (called the Debye layer, DL); (3) finally, the ions in this layer produce a drag on the uncharged fluid flowing through the channel and decrease the overall flow for a given pressure drop (see Method section for complete description). The strength of this drag depends mainly on two parameters: the electric potential—or voltage—at the surface (usually called the zeta potential, ζ), and the I_c of the fluid. Stronger potentials produce more drag while an increased I_c may increase or decrease drag, depending on the ratio between channel size and DL thickness at the particular I_c .

Several observations suggest electroviscosity could be important in the BPM. Measurements show that materials believed to line the BPM surface, such as pectin and lignin⁶³, present moderate to large electric potentials (Table I); though we note there is much controversy as to the presence of non-cellulosic components in the BPM^{41,67,68}. Nonetheless, this conclusion is supported by measurements of streaming potentials in xylem, a related electrokinetic phenomenon⁶⁶ that occurs when pressure-driven flow in a charged channel convects ions and creates an electrical potential difference between the ends of the channel^{69–71}. Previous researchers have mentioned electroviscosity as a possible explanation for the ionic effect^{72,73}. For instance, van Doorn et al.⁶⁴ proposed an analysis of electroviscosity in BPMs. We believe that the analysis of van Doorn et al. errs in its treatment of the electrokinetic processes that lead to electroviscosity by assuming the Debye layer is immobile. As we will show (Fig. 6), their predictions are qualitatively correct at high I_c , but strongly over-predict the decrease in flow due to the electroviscous effect.

Motivation and overview

The purpose of this paper is to develop a complete model of electroviscosity in the BPM and ask if this mechanism can explain the available experimental observations of the ionic effect. Specifically, we ask: Is electroviscosity consistent with the observed response of K_{xylem} to I_c , pH, and ionic identity of the sap? To answer this question, we model electrokinetic effects in an idealized model of the BPM and examine how the properties of sap affect the conductance of individual pores in the BPM. We model the pore surface as presenting a number of chemically-identical chargeable sites per unit area (Γ), where these sites may dissociate and become electrically charged. A surface with a larger Γ will thus develop a larger net charge and produce stronger electroviscosity. We calculate Γ for two materials that represent the low and high end of reported values of ζ for plant materials: cellulose fiber ($\zeta = -15$ mV, $\Gamma_{low} = 6,900/\mu\text{m}^2$), and sugar beet pectin ($\zeta = -60$ mV, $\Gamma_{high} = 120,000/\mu\text{m}^2$), see Table I. Regardless of their presence in the BPM, these two materials cover an expected range of electroviscosity in the BPM: from weak effects (cellulose) to strong effects (pectin).

Subsequently, we assume that the BPM presents the limiting hydraulic resistance in xylem^{34,35}, such that $K_{xylem} \approx K$, and compare our predictions with experimental measurements from the literature. Our results thus represent the maximum decrease in K_{xylem} expected due to electroviscosity, for cellulose and pectin individually; experimental results above this threshold cannot be explained by electroviscosity. This analysis suggests that electroviscosity would produce similar changes in K_{xylem} in the physiological range of composition of the sap as those predicted

by the swelling-shrinking hydrogel hypothesis. Therefore, we propose various experiments that could differentiate between these two phenomena in the BPM. We conclude by discussing the possible implications of electrokinetic effects, if they are important in plants, for the management of flow and refilling of embolisms in xylem.

Material	$-\zeta$ (mV)	Reference
Sugar beet pectin ^a	48, 60	74,75
Kraft lignin ^a	45	76
Citrus pectin ^a	33	77
Cellulose fibers ^a	15	78
Xylem	14	69

Table 2.1: Maximum values of surface potential (ζ) reported for plant materials.^aValues shown are for materials processed in acidic or basic solutions at elevated temperatures; these processes likely increase ζ over its value *in vivo*. We did not find experimental data on ζ for these materials in unprocessed conditions. In this study, we take materials ‘sugar beet pectin’ and ‘xylem’ to represent the upper and lower bounds on the magnitude of the surface potential *in vivo*.

Theory

This section presents a brief overview of electrokinetic phenomena implicated in the hypothesis of electroviscosity in xylem. We explain how surfaces develop electric charge in water and how this charge affects the fluid. Subsequently, we introduce four interrelated electrokinetic phenomena: electroosmosis, electroviscosity, streaming current and streaming potential.

Surface electric charge and potential

Solid surfaces in aqueous solution usually develop net electric charge (Fig. 3). At equilibrium with solution, chargeable sites exchange ions with the fluid and may produce an excess electric charge

on the surface (q'' [C/m²]). For instance, carboxylic acids present in certain plant materials are chargeable sites: they are more likely to lose a proton and become negatively charged (COOH → COO⁻ + H⁺) as the fluid pH rises above their dissociation constant (pK_a ~ 3.5). For simplicity, we model a surface as having only one type of chargeable site, a corresponding pK_a and a density of chargeable sites per unit area Γ (m⁻²), as shown in Fig. 3. On such a surface, the surface charge density is proportional to the number of sites that have liberated a proton (Γ_{A^-} [m⁻²]) and their charge ($-e$):

$$q'' = -e\Gamma_{A^-}, \quad 2.1$$

where $e = 1.6022 \times 10^{-19}$ C is the elementary charge⁷⁹. The specific magnitude of q'' thus depends on the number of ions that dissociate, and is a function of the properties of both the surface and the fluid. For all else equal, a surface with more chargeable sites will have higher surface charge density. Similarly, an increase in pH will increase q'' for acid groups, since more chargeable sites will deprotonate and Γ_{A^-} will increase.

A charged surface attracts counterions from solution. It creates a layer of net ionic charge—the DL—and a corresponding electric potential in the fluid (ϕ [V]). Both the fluid and the ions in the DL are mobile. The volume density of ionic charge, ρ_e [C m⁻³], is largest near the surface, and decays toward zero away from it. The characteristic length over which ρ_e decays is called the Debye length (λ [m]), and is usually taken to be the thickness of the DL. The DL thickens with increases in solution temperature (T [K]) and permittivity (ε [C V⁻¹ m⁻¹]), and decreases in solution I_c . Its thickness is given by⁶⁶:

$$\lambda = \frac{1}{\beta\sqrt{I_c}} \quad 2.2$$

where $\beta = \sqrt{2F^2 / \varepsilon RT}$, $F = 96,485 \text{ C mol}^{-1}$ is Faraday's constant and $R = 8.314 \text{ J mol}^{-1} \text{ K}^{-1}$ is the universal gas constant. For example, at room temperature $\lambda \sim 10 \text{ nm}$ for $I_c = 1 \text{ mM}$, and $\lambda \sim 1 \text{ nm}$ for $I_c = 100 \text{ mM}$. The I_c of the solution depends on the concentration of ions in solution ($c_{i,\infty}$ [mol/m³]) and their valence (z_i):

$$I_c = \frac{1}{2} \sum_i c_{i,\infty} z_i^2 . \quad 2.3$$

As with ρ_e , the potential φ is largest near the surface and decreases to zero over the length λ . The potential at the surface is commonly called the zeta potential, or ζ [V].

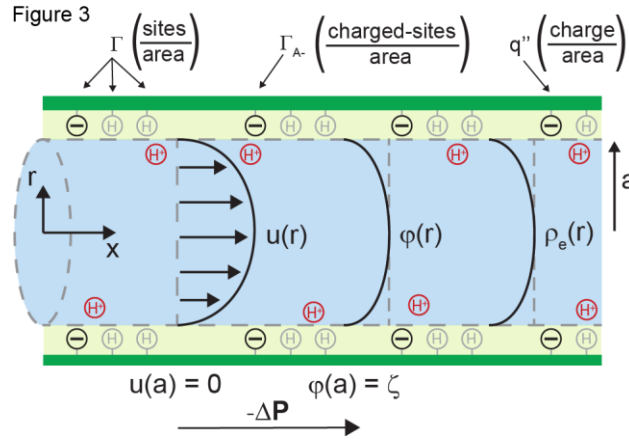


Figure 2.3: Idealized model of a BPM pore. A pressure difference ΔP applied between the ends of the cylindrical channel drives fluid flow. The velocity (u), electric potential (φ), and charge density (ρ_e) in the fluid vary across the radial coordinate (r), but are constant along the axial direction (x). At the surface, the velocity is zero ($u(a) = 0$) and the electric potential is maximum ($\varphi(a) = \zeta$). The surface contains a density of chargeable sites (Γ), some of which lose a proton (H^+) and become negatively charged (Γ_{A^-}), thereby producing a net electrical charge at the surface (q'').

Electrokinetic matrix

In a channel with electrically charged walls, the fluid flow, Q [m^3/s], electrical current, I [A], pressure gradient, $\Delta P / L$ [Pa/m] and electric field, $\Delta V / L$ [V/m] are coupled by the electrokinetic matrix⁶⁶:

$$\frac{Q}{A} = \chi_{11} \left(-\frac{\Delta P}{L} \right) + \chi_{12} \left(-\frac{\Delta V}{L} \right) \quad 2.4$$

$$\frac{I}{A} = \chi_{21} \left(-\frac{\Delta P}{L} \right) + \chi_{22} \left(-\frac{\Delta V}{L} \right). \quad 2.5$$

where the coefficients χ_{ij} (members of the electrokinetic matrix) capture the interplay between the surface and fluid properties, and are derived in the Method section. When an electric field is applied between the ends of a charged channel, it drives the ions in the DL across the channel; these charges drag neutral fluid molecules and create net fluid flow ($\Delta P = 0$ in Eqs. 2.4 and 2.5). This effect is known as electroosmosis. Conversely, when a pressure gradient is applied, it creates a net fluid flow; this flow convects the charges in the DL and creates a flow of electrical current known as the streaming current ($\Delta V = 0$ in Eqs. 2.4 and 2.5). If there exists an electrical path between the ends of the channel, distinct from the ionic path created by the electrolyte that fills the channel, then the convection of charge by a pressure-driven flow will lead to a net streaming current. If there is no electrical path between the ends, then the charges convected by a pressure-driven flow will accumulate downstream and produce an electric potential (ΔV). This potential, called the streaming potential, drives an ionic current against the convection such that there will be no net ionic current ($I = 0$ in Eqs. 2.4 and 2.5).

Electroviscosity

Fig. 4 presents the interplay of these electrokinetic processes in defining the electroviscous effect. As fluid flows through a charged channel without a closed electrical circuit, the resulting streaming potential decreases the permeability of the channel, K , a phenomena known as electroviscosity. Macroscopically, the channel appears to present a lower K than predicted by Hagen-Poiseuille for the radius of the conduit and the viscosity of the fluid. From Eqs. 2.4 and 2.5, setting $I = 0$, the net volumetric flow in a cylindrical channel, taking into account electroviscosity, is given by:

$$\frac{Q}{A} = \left(\chi_{11} - \frac{\chi_{12}\chi_{21}}{\chi_{22}} \right) \left(-\frac{\Delta P}{L} \right). \quad 2.6$$

In Eq. 6, we can identify K as:

$$K = \chi_{11} - \frac{\chi_{12}\chi_{21}}{\chi_{22}}. \quad 2.7$$

The maximum conductance (K^0), which occurs in an uncharged channel ($\zeta = 0$), is given by the Hagen-Poiseuille equation for a cylinder:

$$K^0 = \chi_{11} = \frac{a^2}{8\eta}, \quad 2.8$$

where a is the cylinder radius. Dividing Eq. 2.7 by Eq. 2.8, the conductance of a charged channel relative to an uncharged one is:

$$\frac{K}{K^0} = 1 - \frac{\chi_{12}\chi_{21}}{\chi_{11}\chi_{22}}. \quad 2.9$$

We will use the ratio in Eq. 9 as a measure of the magnitude of electroviscosity in the channel. If there is no surface charge the relative conductance is one.

We use standard electrokinetic theory⁶⁶ to calculate the electrokinetic coefficients, χ_{ij} . One important note is that we account for the dependence of ζ on the properties of the fluid (pH, I_c , T), the properties of the surface material (pK_a , Γ), and the radius of the channel⁷⁹. This calculation is necessary because the value of ζ strongly influences the magnitude of electrokinetic effects, and—as will be seen in the results— ζ varies substantially with the fluid and surface properties and channel radius.

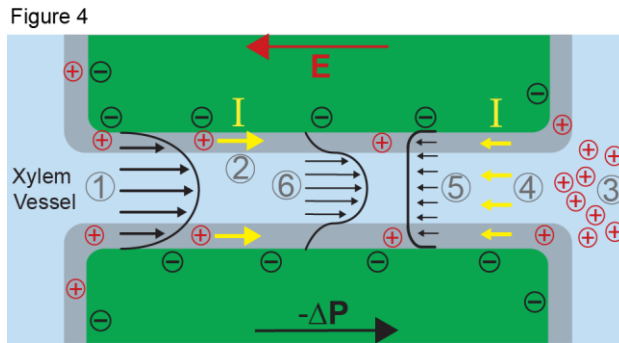


Figure 2.4: The electroviscous effect. Pressure-driven flow (1) sweeps cations in the Debye layer (grey region, 2), and creates a buildup of positive charges at the distal end of the pore (3). Accumulated positive charges produce an electric field (E) that drives an ionic current, I , opposite to the direction of pressure-driven flow (4). These charges drag fluid molecules as they move, creating an opposing electroosmotic flow (5) and decreasing net forward flow through the pore (6). This effect is commonly called electroviscosity.

Results

We now exploit the model described in the previous section to explore the ionic effect on flow through a BPM pore. We discuss the dependence of K on I_c , pH, Γ , a , and ionic identity. We then compare these predictions with experimental measurements from the literature. In the discussion section, we use these predictions to propose experiments and further comparisons with data from the literature.

Conductance as a function of ionic strength, density of chargeable sites and pore size

With our model, we first explore how conductance varies as a function of I_c for the high and low limits of the expected density of acid groups on the walls of the pore (Γ) and for various pore sizes. We use the properties of a simple, one-to-one electrolyte (KCl) previously exploited in many experiments^{54,58}. Fig. 5 presents our predictions for relative conductance (K/K^0), surface potential (ζ) and convected current as a function of I_c . These results are shown for both materials with Γ_{high} (5A) and Γ_{low} (5B), and pores of radii of 1, 5 and 10 nm; these radii cover the range reported from colloidal gold perfusion studies^{80,81}. We note the following: the higher density of chargeable sites (Γ_{high}) leads to larger variations in conductance with I_c (Fig. 5A) than does the lower density (Γ_{low} ; Fig. 5B); and K/K^0 varies non-monotonically for both cases with minima the depths of which grow with increasing radius and positions of which move to lower I_c with increasing pore radius. Although, in general, K/K^0 varies non-monotonically with I_c , it increases monotonically with I_c in the physiological range of I_c (2 to 50 mM⁸²⁻⁸⁴) for the larger pore sizes.

In looking for insights into this behavior, we first turn to the surface potential (Fig. 5, second row). This potential shows much weaker dependence on the density of surface charge than does K/K^0 and it grows monotonically with decreasing ionic strength. On the other hand, the variations of convected current (“2” in Fig. 4) mirror those of the electroviscous effect and thus help elucidate its origins (Fig. 5, bottom row). Firstly, for Γ_{high} , the net charge in the DL is higher such that more charge is convected with the pressure-driven flow than for Γ_{low} ; the convection of

more charge leads to a stronger electroviscous drag. At sufficiently large I_c , the DL is more densely charged but very thin, such that the little charge is convected. Furthermore, at high I_c , the electrical conductance of the solution increases to the point that it significantly reduces the streaming potential (i.e., it acts as a short circuit). At low I_c , the DL is thick compared to the radius of the pore ($\lambda \gg a$), but contains a sparse distribution of charge: the flow convects little charge and produces minimal electroviscous resistance. The minimum of conductance and the maximum of convected current occur when the thickness of the DL is approximately equal to the pore radius ($\lambda \approx a$).

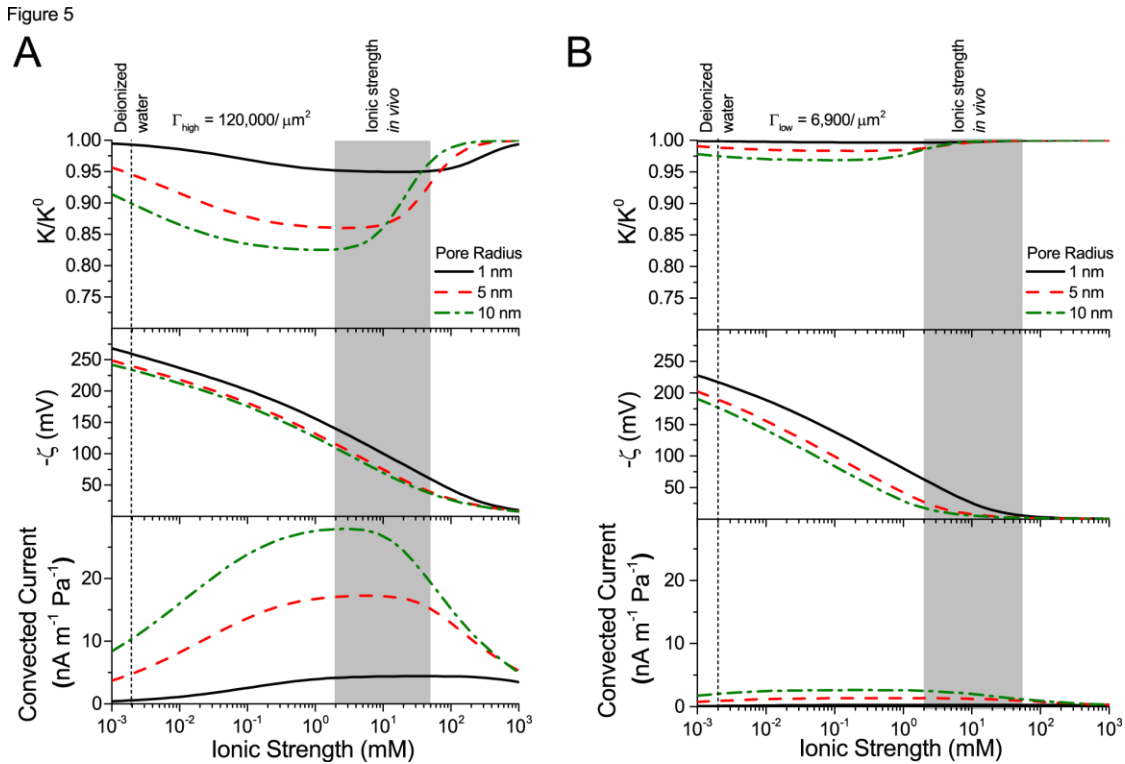


Figure 2.5: Relative conductance (K / K^0) vs. ionic strength for 1-10 nm pores, and density of chargeable sites Γ_{high} (A) and Γ_{low} (B); the corresponding zeta potential (ζ) and convected current are also shown. Properties used: KCl electrolyte in pure water; $pH = 7$; $\Gamma_{high} = 120,000 \mu\text{m}^{-1}$; and $\Gamma_{low} = 6,900 \mu\text{m}^{-1}$.

Comparison to experiments: conductance vs. ionic strength

We now compare our theoretical predictions with experimental data from the literature. By assuming that bordered pits form the limiting hydraulic resistance in xylem, such that $K / K^0 \approx K_{xylem} / K_{xylem}^0$, we calculate the maximum decrease in K_{xylem} expected due to electroviscosity. Fig. 6 presents our predictions for K / K^0 of BPM pores with Γ_{high} and Γ_{low} , alongside theoretical predictions by van Doorn et. al⁶⁴, and data from experimental studies. Measurements shown are for angiosperms for studies in which K_{xylem} was measured across a range of I_c . We selected representative data from each reference (given in caption). We begin by remarking that the model by van Doorn et al. (black dash-dot line)⁶⁴ qualitatively captures the drop in K_{xylem} with decreasing I_c that was observed in some studies, but predicts a larger drop in K / K^0 than observed experimentally for $I_c < 10$ mM. Our model (black solid line for Γ_{low} and black dashed line for Γ_{high}) also captures this decrease of K_{xylem} with decreasing I_c across the physiological range, consistent with the results of van Doorn and co-workers. Indeed, within this range, the trend reported for *L. nobilis* (purple triangles)⁵³, *Chrysanthemum* (red squares)⁵⁴, and *Quercus robur* (green circles)⁵² are compatible in both trend and magnitude with our predictions, given a value of Γ between Γ_{high} and Γ_{low} . These experimental studies are reviewed in Nardini et al.⁷³, where 28 out of 35 experiments on different species, made by various research groups, show a response that falls within, or close to, our predicted range ($K_{xylem} / K_{xylem}^0 > 0.80$), with 5 out of 7 outliers showing $K_{xylem} / K_{xylem}^0 > 0.75$. In general, our predictions are consistent with the experimental data at physiologically relevant values of I_c but are incompatible with various

experimental measurements outside of this range: *L. nobilis* shows $K_{xylem} / K_{xylem}^0 \approx 0.55$ for $I_c \leq 0.1$ mM, while *Conocarpus erectus* (blue triangles)⁴⁷ shows $K_{xylem} / K_{xylem}^0 \approx 0.75$ for deionized water and K_{xylem} / K_{xylem}^0 drops to ~ 0.65 for $I_c = 500$ mM. In all of these cases, the reported responses were significantly larger than we predict based on the electroviscous effect.

Our model can also explain the three distinct responses of K_{xylem} —increase, decrease and no effect—to an increase in I_c reported in literature⁵⁸. Consider a hypothetical BPM with the characteristics of Γ_{high} in Fig. 6: an increase from 2 mM (‘b’ in figure) to 10 mM KCl (#3) produces an increase in K_{xylem} ; a change from deionized water (‘a’) to 10 mM KCl (‘c’) produces no difference in K_{xylem} ; and an increase in I_c from deionized water (‘a’) to a 2 mM KCl solution (‘b’) produces a decrease in K_{xylem} .

Figure 6

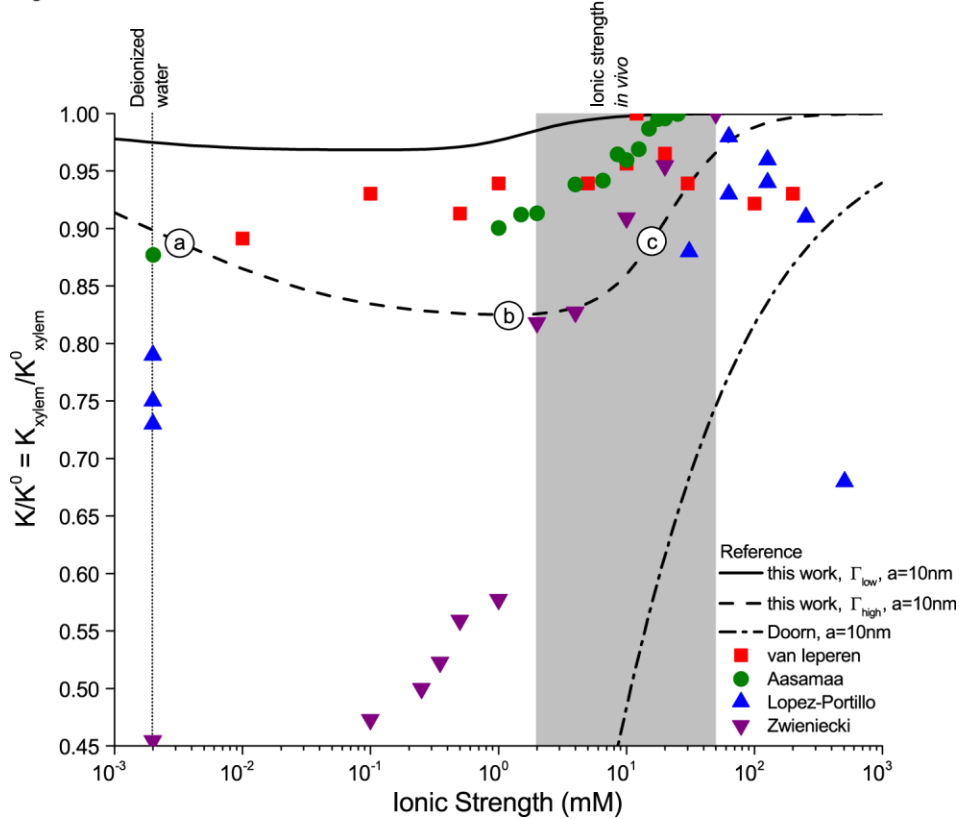


Figure 2.6: Relative hydraulic conductance (K_{xylem} / K_{xylem}^0) vs. ionic strength (I_c) for our theoretical predictions, van Doorn's model, and published experimental data. Theoretical models shown (10 nm pore radius, KCl electrolyte): this work, density of chargeable sites Γ_{low} (solid line); this work, Γ_{high} (dashed line); and van Doorn's model (dash dot line)⁶⁴. Experimental data shown (species, electrolyte, figure in reference): (1) *Chrysanthemum*, KCl, (Fig. 3 in ⁵⁴) (red squares); (2) *Quercus robur* with petioles, various salt solutions, (Fig. 1A in ⁵²) (green circles); (3) *Conocarpus erectus*, NaCl, (Fig. 3 in ⁴⁷) (blue triangles); (4) *L. nobilis*, KCl, average value of K_{xylem} , (Fig. 1C in ⁵³) (purple triangles). Experimental data was normalized to the largest measured conductance in the particular species and report.

Conductance as a function of pH and ionic strength

The hydraulic conductance of xylem has been shown to increase in response to a decrease in pH of the perfusing solution⁵³. We find that electroviscosity presents a similar behavior: conductance is maximum at low pH and decreases to a minimum for pH > 7 (Fig. 7). For $a = 10$ nm and Γ_{high}

, this minimum is $K / K^0 \approx 0.82$. The surface potential follows an opposite trend: it is near zero at low pH, but saturates to its maximum value at $\text{pH} > 7$ (Fig. 7). As the pH is increased, surface chargeable sites deprotonate, producing a larger ζ , a denser ionic layer, and a stronger electroviscous decrease in K . This effect is pronounced at low pH, yet for *in vivo* values of I_c (1 mM, 10 mM) and pH (5.8 – 8)⁸⁵, changes in pH produce only small changes in K / K^0 (~2%). These predictions are qualitatively consistent with experiments, but are too small to explain the large responses observed experimentally. For example, in the study by Zwieniecki et al.⁵³, K_{xylem} at $\text{pH} = 7.5$ was 75% of its value at $\text{pH} = 2.5$.

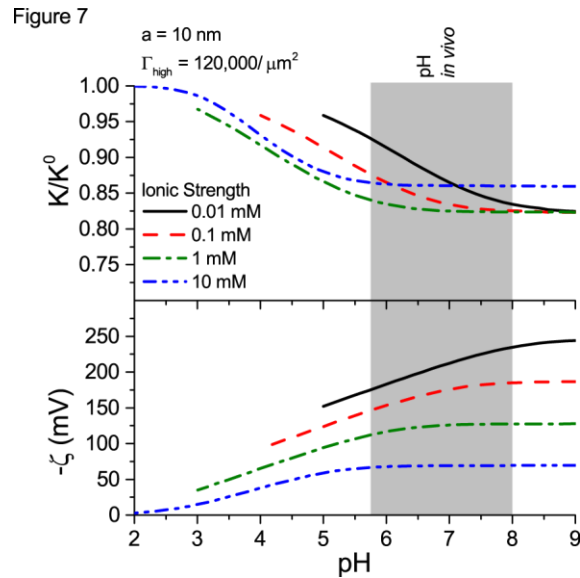


Figure 2.7: Relative hydraulic conductance (K / K^0) and zeta potential (ζ) vs. fluid pH in the BPM, for various ionic strengths. Properties used: KCl electrolyte in pure water; Γ_{high} density of chargeable sites; $a = 10 \text{ nm}$.

Conductance as a function of ion identity and ionic strength

The identity of ions in the sap in perfusion experiments has been shown to affect K_{xylem} ^{53–55}. We now examine this behavior from an electrokinetic perspective. We look at how both the electrophoretic mobility (μ) and valence of ions in the electrolyte affect K . Fig. 8 shows K / K^0 vs. I_c for a solution with various monovalent (A) or divalent (B) cations. As before, K / K^0 shows a non-monotonic relationship with I_c . Conductance is higher for cations with larger mobility, yet is nearly independent of anion mobility or valence. Due to the negative surface charge, cations outnumber anions in the solution within the pore, and therefore the overall electrical conductivity of the solution—and its influence on electroviscous drag—is largely determined by the characteristics of the cations. Cations with larger mobilities increase the solution electrical conductivity and thus decrease both the streaming potential and the electroviscous drag. For instance, K / K^0 for a solution of LiCl is lower than K / K^0 for a solution of KCl at all values of I_c ($\mu_{Li^+} < \mu_{K^+}$). Divalent cations (Fig. 8B) show a similar trend to that of monovalent cations (Fig. 8A), but K is minimum below $I_c < 2$ mM. These predictions, that higher mobility ions decreases flow more, have been reported in some studies, while others report no effect. In *L. nobilis*, perfusion of a 100 mM KCl solution increased flow by 35% over deionized water, whereas 100 mM NaCl increased flow by only 22%⁵⁵, where $\mu_{K^+} > \mu_{Na^+}$. In contrast, a study in *Chrysanthemum* reported negligible difference in K_{xylem} between solutions of 10 mM KCl, NaCl, K₂SO₄, MgSO₄ and CaCl₂⁵⁴. Regardless of the ionic identity, in the physiologically-relevant range, K increases with an increase in I_c for the pore size (10 nm) and pH (7) chosen in our model.

Figure 8

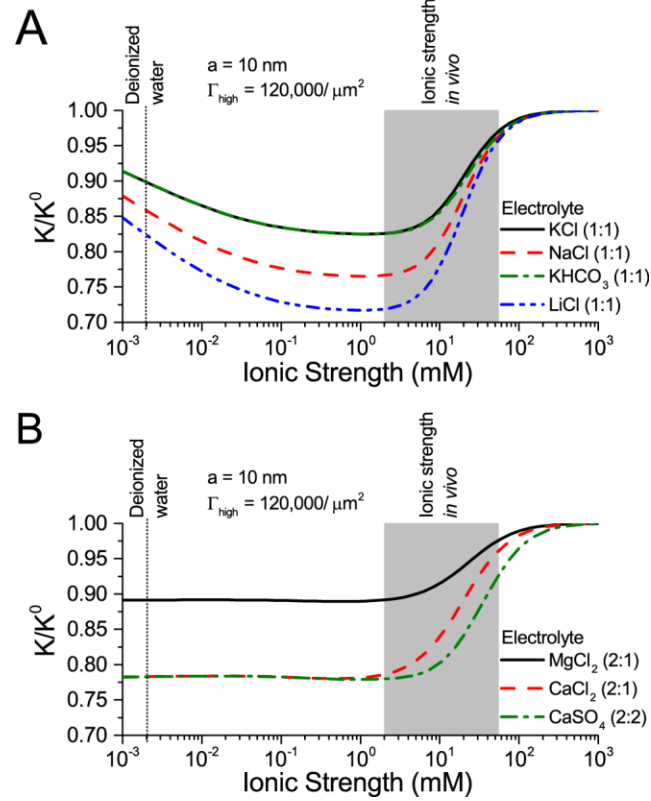


Figure 2.8: Relative hydraulic conductance (K / K^0) vs. ionic strength for an electrolyte with monovalent cations (A) or divalent cations (B). Properties used: given electrolyte in pure water; Γ_{high} density of chargeable sites; $\text{pH} = 7$; pore radius $a = 10$ nm. The electrophoretic mobilities of the cations (μ) are related as follows: $\mu_{K^+} > \mu_{Mg^{2+}} > \mu_{Na^+} > \mu_{Li^+} > \mu_{Ca^{2+}}$. Anion mobilities have negligible effect on K .

Discussion

Our comparisons with available measurements indicate that electroviscosity is compatible with the qualitative trends of most studies in the physiological range of I_c and pH , and shows reasonable quantitative agreement with some experiments. Outside this range, experimental reports diverge both qualitatively (monotonic vs. non-monotonic) and quantitatively; thus we cannot draw any definitive conclusions regarding their compatibility with our predictions. We hypothesize various reasons for these discrepancies: experimental artifacts, model idealizations, and competing effects.

Two experimental artifacts may exaggerate the ionic effect. First, wounding responses in perfusion experiments (i.e. from cutting or perforating the stem) may gradually obstruct xylem vessels with parenchyma-cell outgrowth and secretions⁸⁶, producing an exaggerated decrease in K_{xylem} . Second, various published experiments use deionized water as a baseline measurement of K_{xylem} ; this fluid has an I_c far below plant sap and may cause an exaggerated ionic effect unlikely to exist *in vivo*⁶¹. Because it lacks dissolved ions, deionized water purges naturally present ions from the xylem surface and promotes deprotonation; consequently, its perfusion may increase the surface charge and ζ , thus producing stronger electroviscosity—lower K —than predicted by our model of constant surface composition. This removal of ions could explain why K_{xylem} continues to decrease over time as deionized water is perfused through stems^{46,53,58}, and the pH of this solution is higher upon exiting the stem⁸⁷. On the other hand, K_{xylem} stabilizes when a solution with higher I_c (5 – 10 mM KCl)⁴⁶, or low pH⁸⁸ is used. In a charged channel, a solution with large I_c does not strip ions from the walls to the same extent, and thus keeps ζ constant; a solution with low pH discourages deprotonation and thus lowers ζ , eliminating the electroviscous resistance. In both circumstances flow is stable, close to its maximum value.

In our analysis, the pores of the BPM are modeled as rigid, perfect cylinders, but this geometry may not accurately represent the complex and variable structure of the BPM. First, a recent study imaged a BPM using atomic force microscopy suggests that a BPM may be better modeled as a bundle of fibers, the surface of which is covered with a layer of gel⁶³. This distinct architecture (i.e., from that depicted in Fig. 1D) could change the magnitude and dependence on ionic strength of the effect. Second, studies suggest that theoretical calculations tend to under-predict the

magnitude of electroviscosity in porous media⁸⁹. Third, our analysis predicts that large surface potentials are created at low I_c (Fig. 5). In a real system, this potential would cause the pore walls to repel each other and therefore increase the overall pore size⁶⁴, an effect not accounted for in our model.

We cannot exclude the possible role played by other mechanisms in defining the observed trends. In particular, the hypothesis of gel swelling (Fig. 2) could lead to the same trends in the physiological range, and increase the overall ionic response. For instance, pectin could show both strong electroviscosity and hydrogel-swelling. Permeability might then be influenced by a combination of these effects.

Proposed experiments

Exploiting our theoretical predictions, we now propose three experiments the outcomes of which should be either compatible or incompatible with an electrokinetic origin of the ionic effect. In these experiments, we propose changes in parameters that should not affect the hydration state of hydrogels such that the presence or absence of changes in the ionic effect could be attributed to electrokinetics and not to swelling of hydrogels. We aim to decrease electroviscosity by varying the following parameters: (1) the viscosity of the DL, (2) the electrophoretic mobility of the cations, and (3) the streaming potential. According to Figs. 5 and 7, electroviscosity produces the greatest decrease in flow at $\text{pH} > 6$ and $I_c \sim 2\text{--}3$ mM; therefore, these experiments should be performed in this range to produce the strongest response.

(1) Perfuse a stem segment with a 2 mM KCl solution at constant pressure until flow rate stabilizes. At this point, change the solution to 2 mM KCl with 0.4 wt. % methylcellulose. Experiments in synthetic channels indicate that methylcellulose increases the viscosity near the channel surface and consequently reduces both the amount of charge convected and the electroviscous resistance⁹⁰. Although the overall viscosity of the fluid increases, flow rate should increase if the reduced conductance is due to electroviscosity. Methylcellulose is a neutral molecule, so it will not change the ionic strength of the fluid and should not affect the swelling of hydrogels in the BPM.

(2) Perfuse a stem segment with a 2 mM LiCl solution at constant pressure until flowrate stabilizes. At this point, change the solution to 2 mM KCl. The electrophoretic mobility of K^+ is larger than that of Li^+ ; therefore, the KCl solution is more conductive, produces a weaker streaming potential, and should increase flow rate. From Fig. 8A, we predict that $K_{KCl} > K_{NaCl} > K_{LiCl}$ for any given I_c , and that flow rate should be independent of the identity of anions in solution. This cation-dependent conductance has been shown previously in synthetic systems⁸⁹. Cations with larger valence, e.g. Ca^{2+} and La^{3+} , may confound the results because of their larger tendency to bind to the surface⁹¹.

(3) Perfuse a stem segment with a 2 mM KCl solution at constant pressure until flow rate stabilizes. At this point, create an electrical short circuit in the segment by providing an external electrical path through which the convected charges return to the source reservoir. Because charges can flow freely through the external conductive path, there should be little streaming potential in the stem segment, so the electroviscous resistance should diminish, and flow should increase. This short circuit is used in the microfluidics literature to measure the streaming current by forcing the

streaming potential to be zero ($E = 0$ in Eq. 2.4;⁹²). We note that complete elimination of the streaming potential is challenging due to the polarization of the electrodes, but any observed increase in flow with addition of this external electrical path would provide evidence that electroviscosity is at least partially responsible for the reduction of flow.

Ecophysical Implications

Our analysis suggests that plants may use several mechanisms to enhance sap transport through BPMs in an active manner, possibly in response to emboli. First, by locally increasing the sap's I_c in the physiologically relevant range of 2 to 20 mM, conductance through the BPM could increase by up to 15% (Fig. 5). This increase could occur if voltage-gated ion channels such as outward K^+ rectifiers released K^+ from adjacent cells, thereby increasing K^+ concentration locally in the sap. Similarly, Ca^{2+} could be released into the xylem by calcium-permeable channels that are activated by plasma membrane depolarization⁹³. Second, plants may be able to alter the ionic composition of sap to increase conductance through the pore (Figs. 5 and 7). This increase might be accomplished by selective ion loading into the pore from adjacent parenchyma cells, or via coupling to the phloem. Evidence from stem perfusion studies highlight the importance of BPM to ion-mediated flow; these studies suggest that plants may be able to alter the ionic composition of sap to mitigate the decreased conductance resulting from embolisms⁵⁵. This mechanism would allow plants to maintain sap transport capacity and, consequently, photosynthesis, during prolonged drought conditions.

As BPM surfaces may be electrically charged, the various electrokinetic effects discussed in the theory section may play a role in other plant functions. For instance, changes in flow upon

embolization may lead to changes in distributions of streaming potentials around embolized vessels and serve to trigger refilling^{94,95}. Take a typical BPM that is 130 nm thick and 5 μm in diameter⁹⁶, with 10 nm pores and 0.5 porosity. Assuming sap with $I_c = 1 \text{ mM KCl}$, a pressure drop of 100 Pa across this BPM⁹⁷ produces a flowrate of ~ 0.1 picoliters/s and a streaming potential of 8 μV in our model (Eqs. 2.4 and 2.5). The local change in this streaming potential upon embolization might be sufficient to trigger a refilling program in adjacent parenchymal cells. We also note that, if plants could generate a small electric field across the pit (e.g., based on active membrane processes in adjacent parenchymal cells), it would create electroosmotic flow across the BPM, an effect that could be used to drive sap back into embolized vessels. The possibility that electric potentials in plants may generate flow has been previously proposed for phloem sieve plates as a way to drive water flow through the xylem network^{98–100}. Taking the previously discussed scenario, a modest 10 mV voltage difference across a BPM would create a flowrate of ~ 50 picoliters/s; this flow could refill a typical xylem segment⁴⁹ in 1 minute to 33 hours. We further note that this refilling mechanism could change the constraints on models of vessel refilling previously proposed⁹⁴.

Conclusions

This study presents a rigorous model of the ionic effect based on electrokinetic processes in the BPM. Comparisons of the predictions of this model with available experimental data show qualitative agreement in the physiological range of I_c and pH. The large quantitative differences in experimental measurements across species and the lack of exact, species-dependent knowledge of the properties (pore size, structure, and surface chemistry) of BPMs make it impossible to test this proposed mechanism definitively. Future experiments should aim at the thorough

characterization of each species of interest, and employ manipulations that specifically affect the physical basis of a given hypothetical mechanism (e.g., electrokinetic or swelling of hydrogels). We suggest three such experiments to test the electrokinetic hypothesis. We emphasize that more than one mechanism may underlie the observed behavior. Finally, we point to the possibility that electrokinetic effects described by our model may be involved in other processes within the xylem, distinct from the ionic effect. We hope that this exposition on possible electrokinetic processes in xylem may help in the development of clear, testable hypotheses for the operation of these phenomena *in planta*.

Methods

In this paper, we develop a model of the BPM to investigate how electroviscosity may influence the membrane's hydraulic conductance (K). The BPM hydraulically connects two adjacent vessels, transporting sap through its irregular network of pores. Two models have been proposed for the structure of the membrane: (1) as a permeable gel through which sap diffuses⁶³ or (2) as traversed by a number of discrete pores through which sap flows⁵³ (Fig. 1D). We take perspective (2) and idealize the BPM as comprised of many identical, straight, rigid, cylindrical pores through which sap is driven by a pressure gradient (Fig. 4). This model can be modified to account for the irregularity of BPMs by using data on tortuosity and pore size distribution¹⁰¹. These assumptions overlook the deformation of pores due to hydrogel-swelling⁵³ or electrostatic surface-repulsion⁶⁴. Nevertheless, electroviscosity will be present in nanometer channels regardless of their specific geometry, and we believe that these assumptions capture the dominant characteristics of this phenomenon.

In the following sections we determine the electroviscosity-induced change in K as follows: we (1) derive the electric potential distribution ($\varphi(r)$) and charge density distribution ($\rho_e(r)$); (2) determine the relationship between surface charge (q'') and zeta potential (ζ); (3) extract approximate values for the density of chargeable sites (Γ) from experimental data on plant derived materials; and (4) numerically solve for the electrokinetic matrix coefficients (Eqs. 2.4 and 2.5) to calculate K/K^0 . The parameters used are presented in Table I (general parameters) and Table II (electrophoretic mobilities).

We assume that: (1) the electric field in both axial and azimuthal directions is small compared to the radial field; (2) the fluid properties are constant throughout the channel with the values for bulk liquid water (viscosity and permittivity); (3) the electrophoretic mobilities of the ions are constant and independent of the solution I_e ; and (4) the liquid is incompressible, and the flow is in the Stokes (or creeping flow) regime.

Surface charge and electric potential

Under standard electrokinetic assumptions, the electric field ($\varphi(r)$) and charge distribution ($\rho_e(r)$) in the channel are related by the Poisson equation, which in 1-D cylindrical coordinates simplifies to:

$$\frac{1}{r} \frac{d}{dr} \left(r \frac{d\varphi}{dr} \right) = -\frac{\rho_e(r)}{\varepsilon}. \quad 2.10$$

The charge density at a specific location is given by summing over the concentration of ionic species ($c_i(r)$) and their valence (z_i),

$$\rho_e(r) = \sum_i c_i(r) z_i F, \quad 2.11$$

where the ionic concentration is given by the Boltzmann distribution:

$$c_i(r) = c_{i,\infty} \exp\left(-\frac{z_i F \varphi(r)}{RT}\right). \quad 2.12$$

The charge density (Eq. 2.11) and the Boltzmann distribution (Eq. 2.12) together become:

$$\rho_e(r) = F \sum_i c_{i,\infty} z_i \exp\left(-\frac{z_i F \varphi(r)}{RT}\right). \quad 2.13$$

The charge distribution (Eq. 2.13) is substituted into the Poisson equation (Eq. 2.10) to get the Poisson-Boltzmann (PB) equation, a differential equation that describes $\varphi(r)$ in the channel,

$$\frac{1}{r} \frac{d}{dr} \left(r \frac{d\varphi(r)}{dr} \right) = -\frac{F}{\varepsilon} \sum_i c_{i,\infty} z_i \exp\left(-\frac{z_i F \varphi(r)}{RT}\right). \quad 2.14$$

This equation is solved by enforcing charge neutrality in the bulk

$$\sum_i c_{i,\infty} z_i = 0, \quad 2.15$$

and using two boundary conditions: (i) a wall potential,

$$\varphi(a) = \zeta, \quad 2.16$$

and (ii) symmetry at the channel center,

$$\left. \frac{d\varphi}{dr} \right|_{r=0} = \varphi'(0) = 0. \quad 2.17$$

The PB equation (Eq.2.14) is non-linear and generally must be solved numerically. Here, this equation is first solved for $\varphi(r)$ using an analytical approximation, and this approximate solution is used as an initial guess to solve the PB equation (Eq.2.14) numerically.

Analytical approximation & numerical solution of $\varphi(r)$

In a cylindrical channel with a monovalent electrolyte ($z_+ = |z_-| = 1$) and a small surface potential ($|\zeta| \leq 25$ mV) the PB equation is approximated well by the Debye-Hückel (DH) approximation⁶⁵:

$$\varphi(r) = \zeta \frac{I_0(r/\lambda)}{I_0(a/\lambda)}. \quad 2.18$$

The derivative of Eq. 2.18 is:

$$\varphi'(r) = \frac{\zeta}{\lambda} \frac{I_1(r/\lambda)}{I_0(a/\lambda)}, \quad 2.19$$

where I_0 and I_1 are the zeroth-order and first-order modified Bessel functions of the first kind, respectively. Using Eqs. 2.18 and 2.19 as an initial guess, the PB equation (Eq. 2.14) is solved for $\varphi(r)$ and its derivative $\varphi'(r)$ using a numerical solver for boundary value problems, together with the two boundary conditions in Eqs. 2.16 and 2.17. The symmetry boundary condition is applied at an offset from zero ($\epsilon = 10^{-16}$) to avoid ‘division by zero’ errors. The numerical value of the boundary condition ζ is determined in the next section.

Zeta potential and surface charge

We proceed to determine ζ through both a chemical and an electrical balance between surface and solution in the channel. For the chemical balance, we adapt an analysis for the interaction between a silicon surface and a dilute electrolyte⁷⁹ to represent the dissociation of charges and the surface potential in our model:

$$\zeta = -\frac{k_B T}{e} \left(\ln \left(\frac{e\Gamma + q''}{-q''} \right) + (\text{pH} - \text{pK}_a) \ln(10) \right) - \frac{q''}{C}, \quad 2.20$$

where $k_B = 1.38 \times 10^{-23} \text{ J K}^{-1}$ is Boltzmann's constant, pK_a is the surface dissociation constant and C (F/m^2) is the Stern layer capacitance. Here we use $\text{pK}_a = 3.5$ for a carboxylic acid, and disregard the contribution of the capacitance of the Stern layer because it is negligible for carboxyl surface groups⁷⁹. Another necessary relationship between ζ and q'' comes from electroneutrality: the net charge at the surface must be balanced by the net charge in the fluid. Per unit axial-length of the channel wall, this relationship is

$$q'' = -\frac{1}{a} \int_0^a \rho_e(r) r dr, = \varepsilon \varphi'(a); \quad 2.21$$

commonly known as the Grahame equation¹⁰², where we substituted $\rho_e(r)$ from Eq. 2.10. Eqs. 2.20 and 2.21 together become:

$$\zeta = -\frac{k_B T}{e} \left(\ln \left(\frac{e\Gamma + \varepsilon \varphi'(a)}{-\varepsilon \varphi'(a)} \right) + (\text{pH} - \text{pK}_a) \ln(10) \right). \quad 2.22$$

Eq. 2.22 is solved using a numerical equation solver that takes an initial guess ζ_0 and, together with the method for numerical solution of $\varphi(r)$ and $\varphi'(r)$ explained in the previous section, iteratively solves for ζ .

Determination of Γ from experimental measurements

To calculate ζ for a particular material and fluid combination, we first need to determine the material's density of chargeable sites per unit area (Γ). Because values of Γ for plant materials were not found in the literature, we derive approximate values for Γ from experimental measurements of ζ in the literature. For a particular material, we use a value of ζ measured at (1) an elevated pH, e.g. $\text{pH} > \text{pK}_a$, and (2) at elevated I_c , e.g. $I_c > 10 \text{ mM}$. Under condition (1),

most of the surface chargeable sites are deprotonated, and the amount of surface charge is approximately

$$q'' \approx -e\Gamma. \quad 2.23$$

Under condition (2), ζ is small and the DH approximation applies. Therefore, Eq. 2.19 is inserted into Eq. 2.21 to give:

$$q'' = \zeta \frac{\varepsilon I_1(a/\lambda)}{\lambda I_0(a/\lambda)}. \quad 2.24$$

In addition, under condition (2) the Bessel terms in the surface charge approximation (Eq. 2.24) become:

$$\frac{I_1(a/\lambda)}{I_0(a/\lambda)} \approx 1. \quad 2.25$$

Finally, we combine the DL definition (Eq. 2.2) and Eqs. 2.23 to 2.25, to give:

$$\Gamma \approx \frac{-\varepsilon\zeta\beta I_c^{1/2}}{e}. \quad 2.26$$

The value of Γ approximated this way allows us to determine ζ for any fluid properties, through the chemical and electrical equilibrium (Eq. 2.22) and the numerical solution of the PB equation (Eq. 2.14).

We verified the accuracy of our derivation of Γ and numerical solutions by comparing the values we calculate for ζ against the data of ζ vs. I_c for sugar beet pectin⁷⁵ ($\Gamma = \Gamma_{high}$) and for cellulose⁷⁸ ($\Gamma = \Gamma_{low}$). We find good agreement between our predictions and the experimental data.

Electroviscosity in nanochannels

This analysis of flow is based on a paper by Bowen and Jenner¹⁰³, but without the assumption that the electrolyte is symmetrical. Here the coupling coefficients for the electrokinetic matrix (Eqs. 2.4 and 2.5) are determined. The relative conductance can then be calculated from these coefficients (Eq. 2.9).

Once ζ is known, the total flow in the channel is determined through the Stokes equation:

$$0 = -\frac{\Delta P}{L} + \frac{\eta}{r} \frac{d}{dr} \left(r \frac{du(r)}{dr} \right) + \rho_e(r) \left(-\frac{\Delta V}{L} \right). \quad 2.27$$

This equation is a steady state force balance for a fluid element. It balances the forces due to pressure (first term), viscous friction (second term), and electric fields (third term). We substitute $\rho_e(r)$ from Eq. 2.10 into Eq. 2.27, and integrate the resulting equation with the following boundary conditions: no-slip ($u(a) = 0$), symmetry ($u'(0) = 0$, $\varphi'(0) = 0$), and wall potential ($\varphi(a) = \zeta$). Subsequently, the velocity profile is:

$$u = \frac{(a^2 - r^2)}{4\eta} \left(-\frac{\Delta P}{L} \right) + \frac{\varepsilon(\varphi(r) - \zeta)}{\eta} E. \quad 2.28$$

We integrate the velocity profile over the channel to get the flow per unit area:

$$\frac{Q}{A} = \frac{1}{a^2} \int_0^a u(r) r dr. \quad 2.29$$

Using the notation of the electrokinetic matrix (Eq. 2.4), this integral gives the coupling coefficients for flow:

$$\chi_{11} = \frac{a^2}{8\eta} \quad 2.30$$

$$\chi_{12} = \frac{2\varepsilon}{a^2\eta} \int_0^a (\varphi(r) - \zeta) r dr. \quad 2.31$$

Next, the coupling coefficients for the electrical current are determined. The electrical current through a particular radial location is the sum of the current convected by the flow (first term) and the current conducted by the electric field (second term):

$$i(r) = u(r)\rho_e(r) + E\sigma(r), \quad 2.32$$

where the electrical conductance is given by the density of ions, their mobility and their valence:

$$\sigma(r) = F \sum_i c_i(r) \mu_i z_i. \quad 2.33$$

We substitute Eq. 2.12 in the previous equation to get:

$$\sigma(r) = F \sum_i c_{i,\infty} z_i \mu_i \exp\left(-\frac{z_i F \phi(r)}{RT}\right) \quad 2.34$$

Eqs. 2.32 and 2.33 show that the current at a specific location depends on the density of charge (ρ_e , $c_i z_i$) and the driving force (u , $EF\mu$). The electrical current is integrated over the channel cross section to find the average current per unit area:

$$\frac{I}{A} = \frac{1}{a^2} \int_0^a i(r) r dr = \frac{2}{a^2} \int_0^a u(r) \rho_e(r) r dr + \frac{2}{a^2} E \int_0^a \sigma(r) r dr. \quad 2.35$$

Eqs. 2.10 and 2.28 are then substituted into Eq.2.35; after integration by parts twice, the coupling coefficients for electric current are:

$$\chi_{21} = \frac{2\varepsilon}{a^2 \eta} \int_0^a (\phi(r) - \zeta) r dr \quad 2.36$$

$$\chi_{22} = \frac{2\varepsilon^2}{\eta a^2} \int_0^a \phi'(r)^2 r dr + \frac{2}{a^2} \int_0^a \sigma(r) r dr. \quad 2.37$$

The numerical values of coupling coefficients were calculated by numerically integrating the expressions presented here, where the previously discussed numerical solution for $\phi(r)$ was used.

Our calculations of electroviscosity were compared against the numerical solution proposed in ref

72 and good agreement was found. The MATLAB code used to calculate all the properties presented is available upon request from the authors.

Parameter	Value
Temperature	$T = 298 \text{ K}$
Viscosity of water	$\eta = 8.9 \cdot 10^{-4} \text{ Pa s}$
Permittivity of water	$\varepsilon = 7.08 \cdot 10^{-10} \text{ F/m}$
pH of water	$\text{pH} = 7$
I_c of deionized water at room conditions ^a	$2 \times 10^{-3} \text{ mM}$
Surface dissociation constant ^b	$\text{p}K_a = 3.5$
Number of chargeable sites, cellulose	$\Gamma_{low} = 6,900 / \mu\text{m}^2$
Number of chargeable sites, sugar beet pectin	$\Gamma_{high} = 120,000 / \mu\text{m}^2$

Table 2.2: Parameters used in the analysis.

^aDeionized water exposed to the atmosphere absorbs carbon dioxide (CO_2) from the air. The CO_2 dissolves in the water and dissociates by $\text{CO}_2 + \text{H}_2\text{O} \rightarrow \text{HCO}_3^- + \text{H}^+$ and $\text{HCO}_3^- \rightarrow \text{H} + \text{CO}_3^{2-}$; in equilibrium $I_c = 0.002 \text{ mM}^{104}$. ^bRepresentative value of $\text{p}K_a$ for a carboxylic acid.

Ion	Electrophoretic mobility $ \mu_{ep} \cdot 10^8 \text{ (m}^2 \text{ V}^{-1} \text{ s}^{-1}\text{)}$
Ca^{2+}	3.1
Li^+	4.0
SO_4^{2-}	4.1
HCO_3^-	4.6
Na^+	5.2
Mg^{2+}	7.3
K^+	7.6
Cl^-	7.9

Table 2.3: Electrophoretic mobility of ions used in analysis.

Acknowledgements

Thanks to Maciej A. Zwieniecki, N. Michelle Holbrook, and Fulton Rockwell for helpful discussions on the experimental aspects of measuring the ionic effect, and to Brian J. Kirby for his valuable comments on this manuscript.

CHAPTER 3

MICROLABORATORY TO MANIPULATE AND STUDY LIQUIDS AT NEGATIVE PRESSURE

Michael Santiago^{1*}, *Eugene Choi*², *Erik J. Huber*¹, *Zachary M. Sherman*³, and *Abraham D. Stroock*^{2*}

1. School of Mechanical and Aerospace Engineering, 2. School of Chemical and Biomolecular Engineering, Cornell University, Ithaca, NY 14853, USA, 3. Department of Chemical Engineering, Massachusetts Institute of Technology, Cambridge, MA 02139, USA.

*E-mail: ms2343@cornell.edu and ads10@cornell.edu;

Introduction

Due to attractive intermolecular forces, liquids can hold mechanical tension, analogous to a stretched spring. This tensile state is common in nature and of importance in technological applications. Desert plants commonly transpire water at -4 MPa¹⁰⁵, Sequoiadendron trees transport water at -1.6 MPa to a height above 90 meters¹⁰⁶ and octopus suckers can momentarily pull liquid water to -0.168 MPa¹⁰⁷. Liquids under tension also occur in soil¹⁰⁸, mineral inclusions¹⁰⁹ and drying concrete⁴. If the tension is too large, the liquid will ‘break’—a process known as cavitation. The cavitation pressure of a particular liquid is of technological importance to avoid damage to propellers¹¹⁰, in creating faster ‘supercavitating’ torpedoes¹¹¹, and sonication¹¹². In natural contexts, cavitation is used by pistol shrimp to stun prey¹¹³, and cavitation resistance is a vital part of plant survival in dry regions⁴⁹.

A number of questions also surround liquids under tension, such as: how plants with embolized vessels refill them even under tension⁹⁴, does water have a liquid-liquid transition at negative pressure¹¹⁴, why does water cavitate at lower tensions than predicted by classical nucleation theory in all experimental setups except one¹³, what causes cavitation in other experimental setups¹⁴? A large part of the phase diagrams of liquids is underexplored with respect to both scientific and technological contexts (Figure 3.1). Potential applications for liquids under tension include the transport of liquids against gravity by pulling—nature’s record of pulling water over 90 m dwarfs the human record for pulling water up 17 meters¹¹⁵—and heat transfer against gravity and acceleration¹¹⁶. We need better understanding of liquids under tension and tools with which to manipulate them to answer these questions and develop novel applications. For instance, data on the equation of state (EoS) of water at negative pressures in the most widely used numerical EoS for water—the International Association of the Properties of Water and Steam (IAPWS)—has only been refined based on measurements at positive pressures¹¹⁷, but we note that recent measurements of the EoS were made down to -120 MPa¹¹⁸.

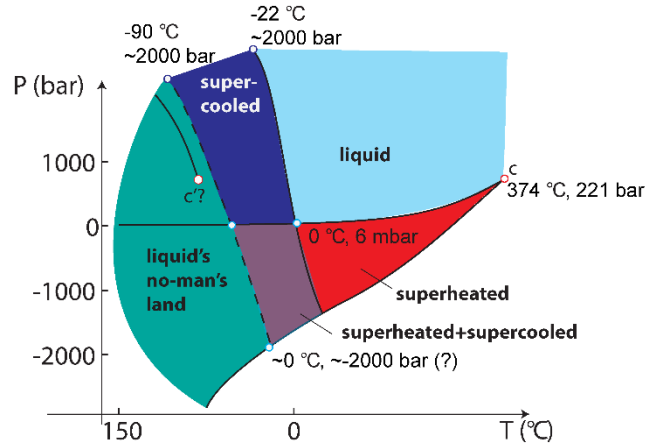


Figure 3.1: Schematic diagram showing the metastable extensions of the phase diagram of water. A liquid can be metastable with respect to temperature and pressure: below the freezing temperature (supercooled, dark blue), above the boiling temperature (superheated, red), below the boiling pressure (superheated, red), or both below the freezing temperature and below the boiling pressure (superheated and supercooled, purple). No man’s land denotes area where freezing generally occurs too rapidly for experimental measurements.

Liquids under tension are hard to manipulate because of they are metastable, tending to cavitate due to thermal fluctuations, mechanical disturbances, and pre-existing nuclei trapped in surfaces or impurities. Various techniques have been developed to study the properties of liquids under tension, particularly the cavitation pressure¹¹⁹. We discuss four. First, is the acoustic method: using acoustic waves to generate a cycle of compression and then tension on a small liquid volume. This technique has the advantage of being highly repeatable and capturing many data points in succession. It has been used to study both cavitation^{120,121} and measure the EoS of water under tension¹²². This method can only produce tension in a microscopic volume $(100\ \mu\text{m})^3$, for a short time $(100\ \text{ns})$ ¹¹⁹. Second, the Berthelot tube method: a volume of liquid and its vapor coexist in a rigid container, the liquid is heated until it expands to fill the volume completely, then subsequently it is cooled down along an isochore to develop tension^{13,123}. When performed in a quartz inclusion, this method holds the record for the largest measured tension in water $(-140\ \text{MPa})$ ¹³; no other

method has come close to measuring tensions this large¹¹⁹. Difficulties with this method include creating inclusions with the desired optical and mechanical properties, a process involving up to 1000 °C and 1.5 GPa for quartz inclusions¹²⁴, or otherwise glass blowing a complex glass helical capillary¹²³. A limitation of this method is that each sample can only follow a specific isochoric line: there is no way to add or remove liquid to study other densities, except with a different sample. Third, the centrifuge method: a volume of liquid in a Z-shaped tube is spun around such that centrifugal forces create tension in the liquid¹²⁵. Unfortunately the pressure set at the tube middle is averaged, making it difficult to impose precise conditions within the liquid, and there are numerous experimental challenges, such as modeling the deformation of the tube in calculating the liquid density^{126,127}. Overall, these 3 methods lack the capability to place macroscopic, static volumes of liquid under tension, and to easily vary the liquid density and change its composition.

In this paper, we developed a system that uses a fourth method—metastable vapor liquid equilibrium (MVLE)³²—discussed in the following section, to study and manipulate liquids under tension. This method, based on the mechanism plants use to transport water¹²⁸, has been used previously to study liquids under tension, such as butane in glass capsules¹²⁹ and water in a suction probe¹⁰⁸. Our system evolved from previous work in our group with hydrogels³², and is based on a previously published sensor, the silicon-membrane microtensiometer (Figure 3.2)¹³⁰. Here we demonstrate its use to study multiple liquids, cavitation pressure, and measurement of the water EoS, in a macroscopic volume of liquid. We now proceed to discuss the working principle behind the microtensiometer: metastable vapor liquid equilibrium.

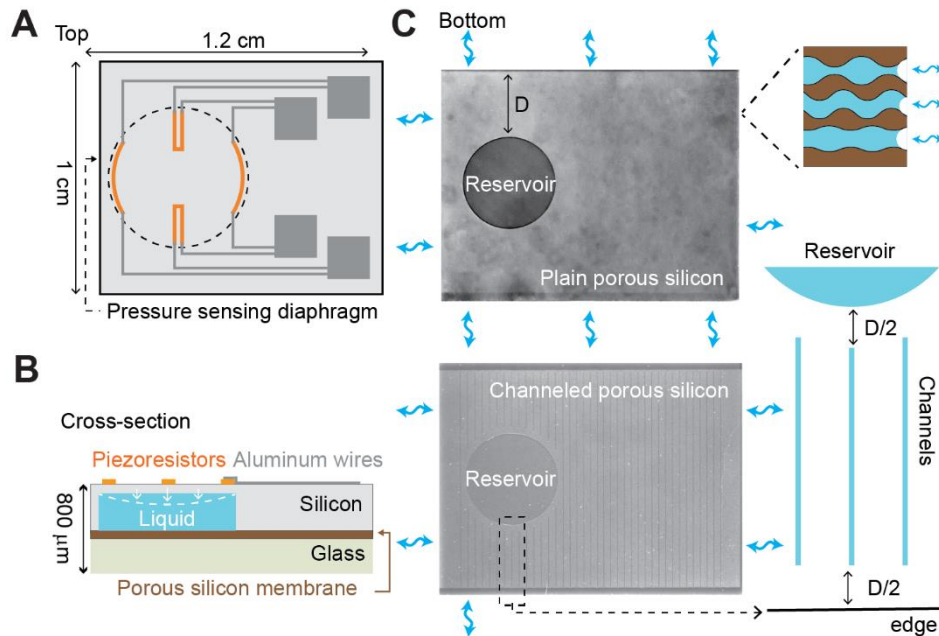


Figure 3.2: Microtensiometer sensor. (A) Illustration of the top-view of the sensor showing the pressure sensing diaphragm—itsself made from 4 piezoresistors (orange lines) in a Wheatstone bridge configuration and aluminum wiring (grey lines). (B) Illustration of the cross-sectional view of the sensor, showing the water-filled reservoir etched in the silicon (blue rectangle), nanoporous silicon membrane (brown layer), and bottom glass part (green layer). The water reservoir is connected to the outside through the layer of nanoporous silicon. As water evaporates from the edges, the diaphragm atop the water reservoir deflects, creates strain in the piezoresistors and changes the balance of resistance around the Wheatstone bridge such that the pressure difference across the membrane can be measured as a change in voltage across the bridge. Note that depth of reservoir is greatly exaggerated relative to thickness of silicon wafer in this diagram. (C) Micrograph showing bottom-view of the sensor with cavity and porous silicon membrane visible. Upper micrograph shows plain porous silicon membrane with only the circular reservoir. Bottom micrograph shows channeled porous silicon that includes the reservoir and vertical channels etched to decrease overall resistance to water flow between reservoir and edge. In both designs, water travels a characteristic length ‘D’ through the porous silicon, between the reservoir and the outside. $D = 1.5 \text{ mm}$ for the plain porous silicon device (no channels) shown, $D = 200 \text{ }\mu\text{m}$ for the channeled porous silicon device. An illustration of the meniscus at the edge of the porous silicon is also shown.

Analysis of device

Metastable vapor liquid equilibrium

The metastable vapor liquid equilibrium method consists of equilibrating a liquid volume with a vapor phase through a porous membrane (Figure 3.3). In a bulk liquid volume exposed to a subsaturated vapor, normally the liquid will evaporate completely, but the porous membrane allows the liquid to come to metastable equilibrium at a reduced pressure relative to the vapor. The resulting pressure difference between the liquid and environment is held by the meniscus curvature at the pore edge (see expanded view in Figure 3.3); the liquid is thus pinned at the pore mouth and prevents the flow of gas into the device. In this method, the liquid chemical potential (μ_{liq} [J/mol]) is set by the vapor chemical potential (μ_{vap}) at equilibrium:

$$\mu_{liq} = \mu_{vap} \quad 3.1$$

$$\mu_0 + \int_{P_{sat}}^{P_{liq}} v_{liq}(P, T) dP = \mu_0 + \int_{P_{sat}}^{P_{vap}} v_{vap}(P, T) dP \quad 3.2$$

Where μ_0 is the reference water potential, P_{liq} [Pa] is the liquid pressure, P_{sat} is the saturated vapor pressure, v_{liq} [m³/mol] is the molar volume of liquid water, v_{vap} is the molar volume of water vapor, $R = 8.314$ J/mol.K is the universal gas constant, T [K] is temperature, P is pressure, $a_{vap} = P_{vap} / P_{sat}$ is the vapor activity and P_{vap} is the vapor pressure. If we assume the liquid is incompressible ($v_{liq}(P, T) = \text{constant}$) and the gas is an ideal gas ($v_{vap}(P, T) = RT / P$), we get the following approximate relation upon solving for the change in pressure induced in the liquid:

$$P_{liq} - P_{sat} = \frac{RT}{v_{liq}} \ln(a_{vap}) \quad 3.3$$

The liquid chemical potential (eqs. 3.1 and 3.2) thus set by the temperature and activity of the vapor, the liquid pressure (eq. 3.3) can be measured to completely define the liquid EoS:

$$P_{liq}(a_{vap}, T).$$

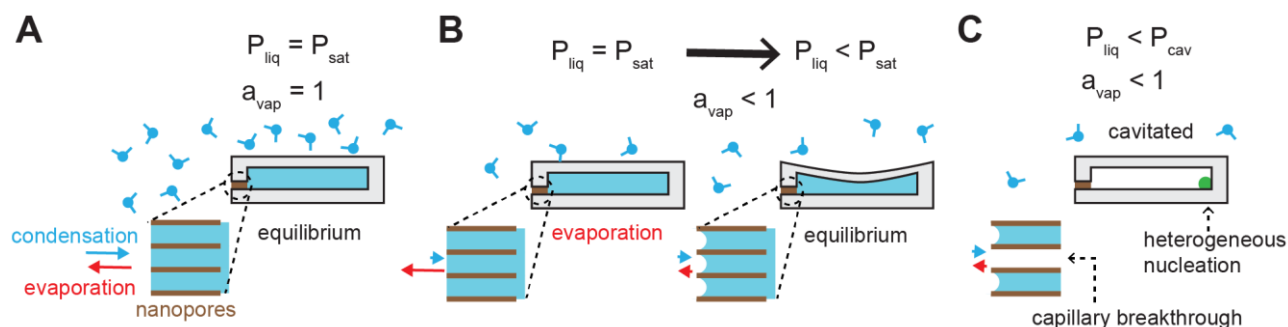


Figure 3.3: Cartoon representation of the measurement principle of our system: metastable vapor-liquid equilibrium. (A-B) In these 3 diagrams, a container holds liquid water (blue) and the outside environment is at a given water vapor activity (a_{vap} , vapor molecules represented by blue circles).

A nanoporous membrane (brown) connects the liquid water to the outside vapor and allows the exchange of water molecules between the liquid and vapor (evaporation and condensation, shown as arrows). Expanded view illustrates nanopores and the shape of the meniscus. (A) In a saturated vapor ($a_{vap} = 1$), the internal liquid and the vapor are at equilibrium at the saturation vapor pressure, P_{sat} .

(B) If the atmosphere is subsaturated ($a_{vap} < 1$), water molecules evaporate from the liquid, decreasing the amount of liquid and lowering its pressure and chemical potential. Liquid continues to evaporate until the liquid pressure drops to the point where it is at equilibrium with the external vapor phase (eq. 3.3) and there is no net condensation or evaporation. (C) If the liquid pressure drops below the cavitation threshold (P_{cav}), the liquid cavitates and the reservoir empties. The system can fail because of capillary breakthrough, heterogeneous nucleation or homogeneous nucleation (not shown).

Nucleation mechanisms

Holding of tension in the liquid reservoir can fail in 3 main ways: meniscus invasion, homogeneous nucleation, and heterogeneous nucleation. When water in a porous material is exposed to a

sub saturated atmosphere, the pressure in the liquid drops as it evaporates and the difference in pressure between the liquid and the atmosphere is held by the curvature of the meniscus at the pore end. If the radius of curvature needed to hold a given pressure difference is smaller than the pore radius, then the meniscus will recede, allowing air in, and preventing the liquid inside the reservoir from holding tension. The pressure at which a meniscus will recede is given by the largest pore that crosses from the environment to the reservoir. In a cylindrical pore, it is given by:

$$P_{liq} - P_0 < \frac{2\gamma \cos \theta}{r_{p,max}} \quad 3.4$$

Where γ is the liquid-vapor surface tension, $r_{p,max}$ is the radius of the largest pore connecting the reservoir to the environment, and θ is the contact angle between the liquid and pore.

Homogeneous nucleation happens when the liquid breaks within its bulk due to thermal fluctuations. This process is predicted well by classical nucleation theory (CNT) for some simple liquids at higher temperatures—such as ethanol and heptane, but for others the observed cavitation pressure (P_{cav}) is much higher (less negative) than predicted—such as dimethyl sulfoxide and water^{8,131}. For instance, CNT states that liquid water can hold tensions above 100 MPa, but most experiments find cavitation at tensions below 30 MPa. Heterogeneous nucleation happens when cavitation in the liquid is nucleated by a boundary or impurity in contact with the liquid. This nucleation can be due to hydrophobic patches in the reservoir, gas held in crevices in the reservoir walls, dissolved gas in the liquid, or contaminants in the liquid¹³². According to CNT, nucleation pressure is modeled as¹³²:

$$P_{cav} = P_{sat} - \left(\frac{16\pi\gamma^3 F}{3k_B T} \frac{1}{\ln(\Gamma_0 V t_c / \ln 2)} \right)^{1/2} \quad 3.5$$

Where k_B is the Boltzmann constant, V is the liquid volume under study, t_c is the measurement duration, and $F = (2 + 3 \cos \theta - \cos^3 \theta) / 4$ where θ is the equilibrium contact angle of water with the reservoir surface. The variable Γ_0 is a prefactor approximated by:

$$\Gamma_0 \approx \left(\frac{4}{3} \pi r_c^3 \right)^{-1} \frac{k_B T}{h} \quad 3.6$$

Where h is Planck's constant and $r_c = 2\gamma / (P_{sat} - P_{liq})$ is the critical radius of a vapor bubble above which it will nucleate cavitation.

Channel structure and equilibration time

In this study, we have characterized a sensor that differs from the one previously published¹³⁰ in only one characteristic: in addition to etching the reservoir in the bottom side of the silicon, channels were also etched to decrease the overall resistance to liquid flow between the reservoir and the environment. See Figure 3.2C and compare the plain porous silicon with the channeled porous silicon. By decreasing the resistance to flow, we can decrease the time for sensor equilibration with a sensed environment. We proceed to analyze the response time of the sensor with these additional channels and compare it to the original design without channels.

Flow of water between reservoir and sensed environment (Q) is a function of the difference in pressure between the reservoir and the pore edges (ΔP) and the hydraulic resistance (R [Pa.s/m³]):

$$Q = \frac{\Delta P}{R} \quad 3.7$$

We approximate R as

$$R = \frac{D}{2\pi r_r d \kappa} \quad 3.8$$

Where D is the characteristic distance water travels through the low permeability porous silicon, r_r is the reservoir radius, $d = 5 \mu\text{m}$ is the thickness of the porous Si and $\kappa = 2 \times 10^{-17} \text{m}^2/(\text{Pa}\cdot\text{s})$ is the Darcy permeability of the porous silicon; the value of permeability was measured in a related experimental system with porous silicon formed by the same procedure as here¹³³. We use a pseudo steady state approximation, because the pressure profile in the porous silicon membrane equilibrates much faster than the pressure in the reservoir. We further assume that the resistance of the channels is negligible relative to flow through the porous silicon and that there is no boundary limitations to vapor flux at the device edge.

The system can be modeled as an electrical RC system, which has a characteristic time (τ) of:

$$\tau = RC \quad 3.9$$

where C is the system capacitance. The capacitance is a sum of the capacitance from stretching the water and stretching the diaphragm:

$$C = \left(\frac{1}{B_r} + \frac{1}{B_w} \right) V_w \quad 3.10$$

where B_w [Pa] is the bulk modulus of water, V_w is the volume of water in the system (neglecting water in porous silicon)

$$V_w = h\pi r_r^2 \quad 3.11$$

and $h = 25 \mu\text{m}$ is the reservoir depth.

The variable B_r represents the effective bulk modulus for the diaphragm, and can be approximated from the definition of bulk modulus $B_r = V_w dP / dV \approx V_w \Delta P / \Delta V_d$. For a given pressure difference between the diaphragm and the outside, the water displaced compared to zero deflection is

$$\Delta V_d = \pi r_r^2 w_{avg} . \quad 3.12$$

Where w_{avg} is the average deflection in the diaphragm, given by¹³⁴

$$w_{avg} = \frac{(1-\nu^2) r_r^4 \Delta P}{16Et^3} . \quad 3.13$$

Here, $\nu = 0.27$ is the poisson ratio of silicon, E is the Young modulus of silicon, and t is the diaphragm thickness. Putting eqs. 3.11-3.13 together with the definition of bulk modulus we get:

$$B_r = \frac{16Et^3}{\pi r_r^6 (1-\nu^2)} V_w \quad 3.14$$

Finally, combine eqs. 3.8-3.11 with eq. 3.14 to get an expression for the characteristic time:

$$\tau = \frac{Dr}{2d\kappa} \left(\frac{h}{B_w} + \frac{r^4 (1-\nu^2)}{16Et^3} \right) . \quad 3.15$$

Materials and methods

Fabrication, calibration and use of sensor

Fabrication and calibration steps for the microtensiometer are discussed in detail in our previous paper¹³⁰. Briefly, the sensors are fabricated on a silicon wafer. First, silicon oxide and doped polysilicon are deposited and patterned to create a Wheatstone bridge of piezoresistors. Second, a reservoir is etched on the silicon underside, followed by an electrochemical etch of the porous silicon membrane. Third, the silicon wafer is anodically bonded to a glass wafer. Fourth, wiring is made on top of the silicon with a layer of aluminum, followed by a passivation layer. Relative to

our previous version, the sensor presented here was changed by adding channels to the reservoir mask to decrease equilibration time (see Figure 3.2, channeled porous silicon).

A custom-built jig (CorSolutions) made of an acrylic top and aluminum bottom was used to make electrical connection with the sensor during calibration and measurements. The jig held in place four gold-plated spring pins (0.075" probe, Interconnect Devices, Inc.) that make electrical contact with the four electric pads on the sensor. The sensor was powered by a constant 200 μ A current source (REF200, Texas Instruments), and its voltage output read with a digital multimeter (34401A, Agilent).

Before use, the sensor needed to be calibrated and then filled with water. For calibration, the microtensometer chip is placed in water for 15 minutes to wet the porous membrane and prevent air from entering the reservoir. Then the sensor is mounted on the CorSolutions jig, placed in a high pressure chamber system (OC pressure reactor, High Pressure Equipment Company) and compressed air was used to apply positive pressures. A pressure gauge (TJE 5000 psig, Honeywell Sensortec, Columbus, OH) was used to monitor the pressure in the chamber. Four different pressures were applied sequentially, and the sensor output at each pressure is written down to create a calibration curve. For filling, the bare sensor chip was placed in an impermeable, flexible bag (Bitran S bags, VWR) filled with the liquid of interest, and the bag was placed in a high pressure chamber that was filled with water. The water was then pressurized to 1000 psi with a high pressure generator (Model 37-6-30, High Pressure Equipment Company) for 24 – 48 hours to fill the sensor. After filling, the sensor was removed from the pressure chamber and visually inspected to check that the reservoir was full.

Measurement of liquid cavitation pressure

We measured the liquid cavitation pressure (P_{cav}) for methanol, acetone and water. For each measurement, the microtensiometer chip was filled with the solution being measured as explained above. Once full, the sensor was interrogated with the CorSolutions jig and allowed to equilibrate with the dry ambient air. The experiment was kept running until the measured tension reached a maximum value and dropped to zero. Three measurements were taken for methanol and water, and two measurements for acetone. These measurements specifically were made with one device that had very low permeability porous silicon to decrease the possibility of meniscus invasion. Hence, as will be seen in the results, the devices took much longer to cavitate than expected from eq. 3.15. We also note that we tried filling the sensor with isopropanol, but even after a week at 1000 psi the isopropanol did not go through the porous silicon membrane and the reservoir remained empty.

Measurement of water EoS

To measure the water EoS, we built a system to control the temperature and water activity around the microtensiometer sensor (see Figure 3.4). The system contained a custom-built vacuum chamber (machined aluminum cylinder, 11 cm diameter \times 10 cm height, 1.5 cm wall thickness), a glass water reservoir, and a vacuum pump (TRIVAC NT5, Leybold). The sensor sat in the vacuum chamber and the CorSolutions jig was used to power and read it; a custom made feedthrough was added to the chamber to contact the power and signal wires from the jig. The chamber also contained a thermometer and pressure gauge (ASD 2002, Adixen). The vacuum chamber was connected to a water reservoir on one side and on the other side to a vacuum pump. A custom-

made computer controlled valve (made from a modified metering valve—SS-4L-MH, Swagelok— and a stepper motor connected to an Arduino microcontroller) between the reservoir and chamber controlled the flux of water vapor by following a custom LabVIEW proportional controller. A set of manual valves between the chamber and the vacuum pump served to throttle the amount of vacuum pulled. The vacuum chamber and water reservoir were kept in two separate isothermal baths (Isotemp 3006P, Fisher Scientific), with the water reservoir set at a temperature 5 °C higher than the vacuum chamber. We desired to have a slightly hotter water reservoir to have a larger vapor pressure and be able to condense water in the vacuum chamber. The vacuum chamber was kept at a constant temperature by the isothermal water bath, but the accurate control of activity was an active process.

To start a run, the vacuum chamber was opened, a microtensiometer was connected to the feedthrough inside, a few milliliters of water were added to increase the humidity in the chamber and prevent the microtensiometer from cavitating, and the chamber was closed. The vacuum pump was turned on and both the valves were opened to get a constant flux of water vapor going from the reservoir through the vacuum chamber to the vacuum pump. After 60 minutes, enough time for most of the air to be flushed out from the system, we proceeded to measure P_{sat} . The valve to the vacuum pump was closed and the valve to the reservoir was opened completely for a few minutes to allow enough vapor to create condensation in the vacuum chamber. Afterwards, the valve to the reservoir was also closed completely to isolate the vacuum chamber. At this point, the water vapor pressure in the chamber increased to P_{sat} , and this value was measured by the vacuum gauge. Measuring this value, instead calculating it from the chamber temperature, allowed us to

ameliorate problems with drift in the pressure gauge (for details, see uncertainty analysis in the supplementary information).

After P_{sat} was measured, we proceeded through set steps of vapor activity in the chamber and measure the corresponding P_{liq} (Figure 3.5). The pressure in the chamber was kept at the desired P_{vap} by the proportional controller connected to the water reservoir valve. Briefly, if P_{vap} was greater than desired, the stepper motor closed the valve slowly until P_{vap} reached the desired value; if P_{vap} was lower than desired, the stepper opened the valve. This process usually reached equilibrium within a few minutes. The chamber was kept at the desired P_{vap} long enough for P_{liq} to plateau.

Calculation of IAPWS plot

To compare our EoS measurements with the IAPWS extrapolated EoS, we rearrange eq. 3.2 into the following equation (assuming vapor is an ideal gas):

$$a = \exp\left(\frac{1}{RT} \int_{P_{sat}}^{P_{liq}} \frac{1}{\rho_{liq}} dP\right) \quad 3.16$$

Where the liquid density (ρ_{liq}) is the inverse of the liquid molar volume ($v_{liq} = 1/\rho_{liq}$). The pressure of the liquid is given as a function of ρ_{liq} and T by the IAPWS EoS¹¹⁷, and we use an interpolating function to get $\rho(P_{liq}, T)$. Vapor pressure data was obtained from Murphy and Koop¹³⁵ and NIST¹³⁶. Eqn 3.16 was then integrated numerically to get $a(P_{liq}, T)$ for Figure 3.8.

An uncertainty analysis and χ^2 test were run to compare our measurements with the IAPWS EoS; details are in the supplemental data.

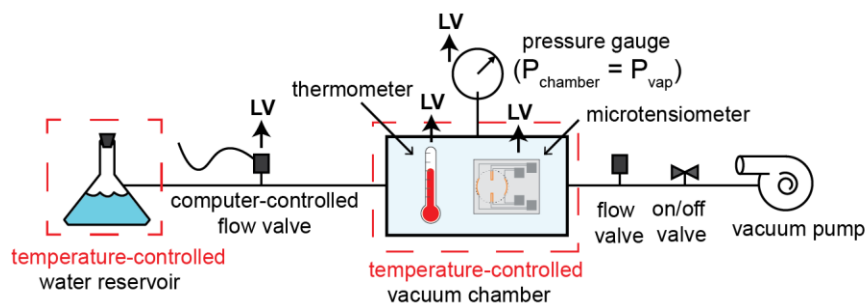


Figure 3.4: Experimental setup to measure water equation of state. The system consists of a vacuum chamber with controlled temperature and activity. Water was continuously pulled from the water reservoir through the vacuum chamber and the flow was modulated by a computer-controlled flow valve to set the water vapor pressure in the chamber. A microtensiometer, thermometer and pressure gauge sat inside the vacuum chamber during measurements. ‘LV’ denotes data sent to LabVIEW. Temperature control was done in an isothermal bath.

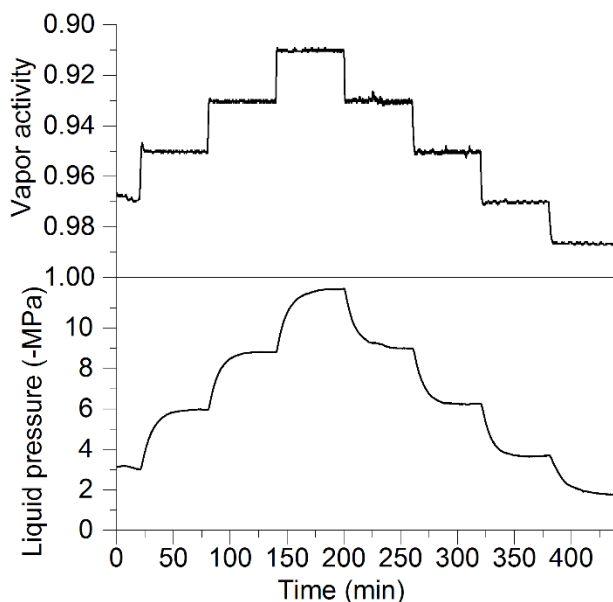


Figure 3.5: Representative run of equation of state measurements ($P(a, T)$). We set vapor activity (top) inside the chamber, then measure the resulting liquid tension (bottom) inside the microtensiometer. The plateau value of vapor and liquid values after each step change, in conjunction with temperature data, made up one data point of $P(a, T)$ (eq. 3.2).

Results and discussion

Cavitation pressure

Figure 3.6 shows our measurements of P_{cav} for water, methanol and acetone, and comparisons with expected values according to CNT. We find that devices filled with water achieved the lowest pressures and cavitate fastest, followed in speed by methanol then acetone. Measured P_{cav} are substantially above those expected by CNT for all three substances, but the difference in water is highest: -15.7 MPa measured P_{cav} vs. an expected -140 MPa.

Table 3.1 shows the liquid surface tension and average P_{cav} . These values are compared with the expected cavitation pressures from CNT, and the decreased surface tension that could explain why measured P_{cav} is higher than expected (eq. 3.5). The last row shows the calculated pore size needed to explain the decreased P_{cav} as a meniscus invasion. We find that for all these variables, methanol and acetone act very similarly, both having a P_{cav} about 40% of the expected value.

What sets the values of P_{cav} for these solutions? We rule out homogeneous nucleation, since the measured P_{cav} values for all liquids were substantially smaller magnitude than predicted by CNT (~38% for methanol and acetone, ~11% for water, eq. 3.5) and than those measured in previously in related systems based on MVLE^{137,138} or by other methods¹¹⁹. We note that acoustic cavitation experiments show cavitation tensions ~65% of CNT expectations for liquids of similar surface tension to methanol and acetone: ethanol and helptane¹³⁹. Cavitation in acetone and methanol could be produced by either meniscus invasion or heterogeneous nucleation due to hydrophobic patches, particulates, or trapped air. Although the average pore radius in our system is 2 nm,

porosimetry measurements of porous silicon samples show that $\sim 0.1\%$ of the pore space is of pores larger than 4 nm in radius (see Supplementary info); therefore some of these pores may connect the reservoir and outside environment and allow meniscus breakthrough (eq. 3.4). On the other hand, if cavitation were caused by meniscus invasion, P_{cav} would be well defined for a given solution and we expect to see little scatter. Values of P_{cav} measured in methanol varied by ~ 2.3 MPa from the largest to the smallest. For water, the data suggests cavitation was not caused by meniscus invasion. If we consider break through of the menisci as a mechanism, a pore 4.6 nm in radius connecting the reservoir with the outside could explain the discrepancy in acetone and methanol, but a 9 nm radius pore would be needed to explain the discrepancy in water.

Testing with other solutions of intermediate γ would help find the method by which cavitation happens in this system. Although we could not fill this microtensiometer with isopropanol, we believe it will be compatible with the usual porous silicon larger pore sizes we use to form these devices.

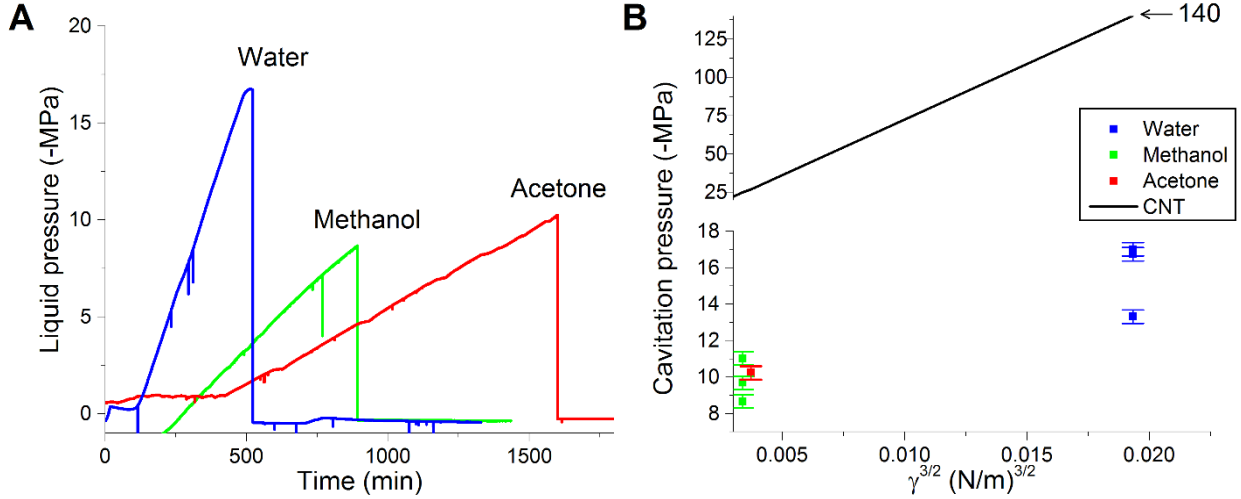


Figure 3.6: Cavitation pressure of different liquids in tensiometer. (A) Time plot of tensiometer filled with liquid and exposed to ambient. Shows liquid tension increasing to a maximum value where the liquid cavitates and sensor measures zero tension. (B) Cavitation pressure measured for methanol, acetone, water, plotted against surface tension raised to the three-halves power as it appears in eq. 3.5 for the classical nucleation theory (CNT) prediction. Black line is prediction from CNT, plotted on a different y axis to fit the figure.

Liquid	P_{cav} (-MPa)	$P_{cav,CNT}$ (-MPa)	γ (mN/m)	$\gamma_{reduced}$ (mN/m)	$r_{p,max}$ (nm)
Methanol	9.8 ± 1	25	22.5	12.2	4.6
Acetone	10.2 ± 0.4	27	24	12.5	4.7
Water	15.7 ± 1.7	140	72	16.7	9

Table 3.1: Cavitation data and comparisons with classical nucleation theory. Liquid cavitation pressure (P_{cav}) measured, cavitation pressure predicted by classical nucleation theory ($P_{cav,CNT}$), bulk surface tension (γ), decreased surface tension ($\gamma_{reduced}$) that would explain the measured P_{cav} according to CNT with the measured average pore size, and pore size ($r_{p,max}$) that would explain measured P_{cav} as a meniscus invasion with the bulk surface tension.

Equilibration time

Figure 3.7 shows a measurement with a plain porous silicon device and a channeled device of the same diaphragm size. The measured value of τ decreased by a factor of 2 - 16 with the addition of the channels. We note that equilibration times seemed to vary considerably between devices of

the same pore radii. Equilibration times also varied considerably even while using the same device in different runs, up to a 4x difference from one run to the next. These variations in equilibration time might be caused by contaminants that obstruct the membrane and accumulate over time—for instance, oils blocking the pores.

Table 3.2 shows predictions and measurements of τ in plain and channeled porous silicon devices of different reservoir radii. Measurements in plain devices were taken from our previous paper¹³⁰. For plain devices, the predictions are up to 6 times lower than measured values in devices with diaphragms with 0.7 mm and 1 mm radius, but the predictions become accurate for the larger devices of 2 mm and 3.4 mm. For the channeled devices, our predictions are again lower than the measured values, but by a larger factor. We did not measure τ in channeled devices with diaphragm radii other than 1 mm. Although the channels helped speed up measurements, they did not help as much as we predicted.

The discrepancies in predicted vs measured τ might be explained by a number of factors. The calculation of τ involves 2 components, resistance and capacitance (eq. 3.15). Discrepancies in R could be caused by an erroneous value of κ : the value used here was measured in a system of porous silicon bonded to patterned glass with cavities¹³³. In our system, the cavities are formed on the porous silicon side, which could affect the permeability of the porous silicon. Discrepancies in C arise partially from our neglecting the amount of water held in the porous silicon pores, an effect that becomes more important for devices with smaller water reservoirs.

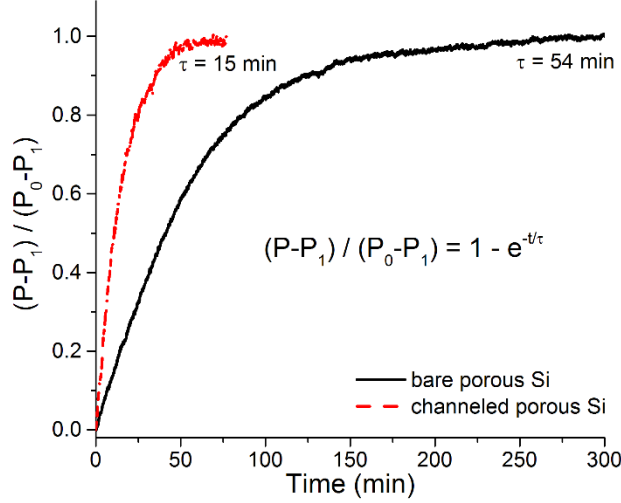


Figure 3.7: Comparison of equilibration time for a typical bare (black) and channeled (red) porous silicon device, with a 1 mm radius diaphragm. Data for bare device is from previous publication¹³⁰.

r (mm)	τ (min)			
	Plain		Channeled	
	Prediction	Measured ¹³⁰	Prediction	Measured
0.7	4	18	0.2	-
1	10.5	66	0.5	4 to 30
2	166	200	11	-
3.4	1200	1200	153	-

Table 3.2: Predictions and measured equilibration time constants (eq. 3.15) for plain devices and channeled devices.

Measurements of water EoS

Figure 3.8 shows our measurements of the water EoS compared with IAPWS extrapolated data at five different temperatures. These results agree with the IAPWS EoS within experimental error, with a good fit ($\chi^2 = 0.42$). In general, measured values for liquid tension were larger than expected by 0.3 to 0.5 MPa, and this discrepancy became larger for measurements at lower activities. For each set of measurements at a particular temperature, the slope (dP/da) was larger than predicted by IAPWS (Table 3.3). All the slopes measured are within 3% of that predicted by IAPWS, with the exception of measurements taken at 20 °C that show a ~8% difference.

These systematic errors were likely caused by the addition of errors in a number of elements in our system: systematic errors in sensor calibration—a miscalibrated pressure gauge and non-equilibrium temperature in the pressure bomb; systematic errors in setting the vacuum chamber activity—a miscalibrated vacuum pressure gauge and overestimation of the vapor saturation pressure; systematic errors in the chamber or sensor temperature—a consistent higher temperature in the sensor due to ohmic heating or poor sensor-chamber thermal contact. Unfortunately, the origin of these discrepancies is difficult to find due to the large sensitivity of the measured liquid pressure to uncertainties in measured P_{vap} , P_{sat} and T . According to our uncertainty analysis, the largest contributors to the error in our system are (1) errors in setting and measuring the vapor pressure in the vacuum chamber and (2) errors in applying a constant current to power the sensor. It is conceivable that errors (1) could be minimized with a better designed and calibrated system, both vacuum chamber and gauge, and errors (2) could be minimized by using a more stable current or voltage power supply.

Comparison with recent measurements of the water EoS

The technique presented here for measuring the EoS of water under tension can reliably measure the EoS following an isothermal trajectory, in a bulk volume of water, for temperatures above 0 °C and pressures down to -15 MPa. Its measurements agree with IAPWS predictions. Because of the way we are measuring the EoS, this method tends to smoothen out features in the water EoS. It uses an integral of the molar volume (eq. 3.2). Deviations from the IAPWS are expected to be larger for larger tensions and lower temperatures, but both of these directions would cause experimental problems in our setup. Unfortunately, the microtensiometers tend to cavitate at

pressures below -15 MPa, and measurements below 0 °C would suffer from problems with ice formation in the vacuum chamber from deposition of water vapor. The system is also limited to temperatures below ~25 °C because of the vacuum pump's limited tolerance for higher values of water vapor pressure.

The water EoS has been previously measured by at least three different methods. First, Stephen and Henderson¹⁴⁰ used a Berthelot tube modified with a helix and mirror to measure the temperature of maximum density in stretched water. They measured both temperature and pressure in a bulk volume of liquid trajectory of constant mass, spanning temperatures from -20 °C to 90 °C and pressures down to -20 MPa. Unfortunately, their estimates of liquid volume were less reliable than those given by extrapolations from the IAPWS due to the complex variations in the volume of the helix as a function of pressure. Second, Davitt et al¹²² used focused acoustic waves in combination with Brillouin light scattering and a fiber optic hydrophone to repeatedly place microscopic volumes of liquid under tension and simultaneously measure the liquid temperature, speed of sound and density. All measurements were made isothermally at room temperature (23.3 °C) and pressures were measured down to -26 MPa. Their measurements agreed with the IAPWS extrapolated EoS to within experimental uncertainty. Third, Pallares et al^{114,118} used a microscopic Berthelot tube combined with Brillouin light scattering to measure liquid temperature and sound velocity under isochoric conditions. Their measurements spanned from -15 °C to 60 °C, and by fitting their data they created an experimental equation of state down to -120 MPa. These researchers found that their measurements of speed of sound diverged from IAPWS extrapolations at temperatures near 0 °C and below.

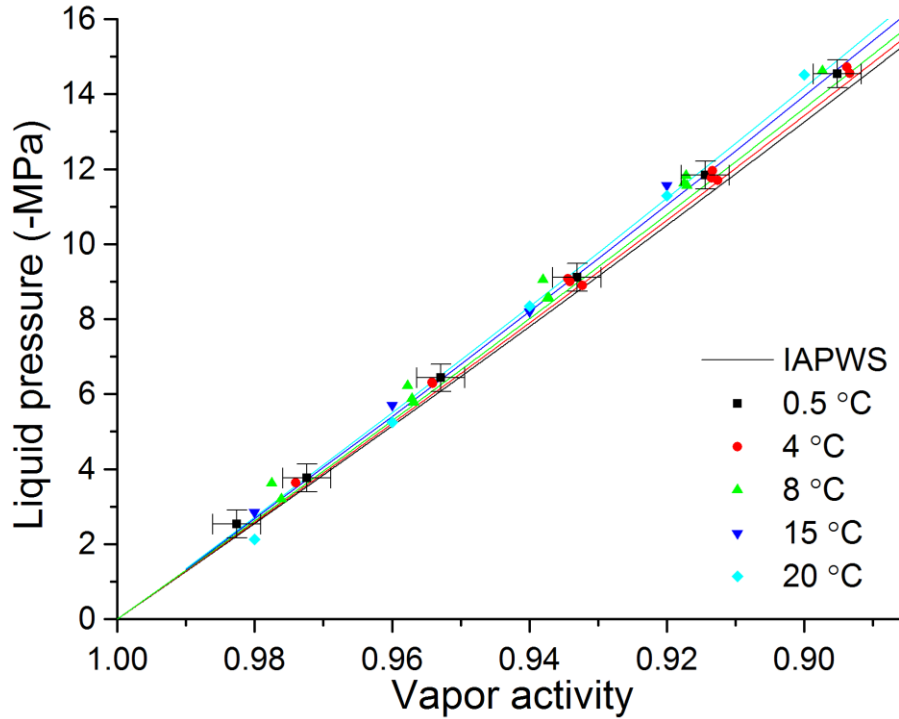


Figure 3.8: Experimental measurements of water equation of state. Measurements of liquid tension vs. vapor activity for various temperatures (symbols), compared with the expected values from the IAPWS extrapolated equation of state (solid lines). For simplicity, error bars only shown for $T = 0.5 \text{ }^\circ\text{C}$.

Temperature ($^\circ\text{C}$)	dP/da (MPa)		Difference (%)
	Measured	IAPWS	
0.5	138.0 ± 2.6	133.7	3.3
4	136.6 ± 2.6	135.3	0.9
8	140.9 ± 2.8	137.3	2.6
15	143.2 ± 29.7	140.9	1.6
20	154.2 ± 4.3	143.2	7.7

Table 3.3: Comparison of EoS slope measured with IAPWS extrapolated values.

Challenges and future work

There were a few experimental challenges with our experimental system. Unfortunately, the electrical connection between the sensor and jig would break down if there was condensation in the chamber and this caused problems with measuring P_{sat} . Sensors themselves tended to stop

working over time as they were exposed to humid environments: the thin, 300 μm -wide, aluminum wiring in the sensor would oxidize and corrode in the presence of humidity. Even before they stopped working, the sensor's offset would change, a problem likely due to the corrosion of the aluminum wiring and changes in the contact resistance between the jig spring pins and the sensor. We are exploring the use of corrosion resistant metals for wiring (see Ch. 4 for discussion of an updated design). The vacuum gauge drifted from experiment to experiment such that P_{sat} had to be measured before every run. With the current setup it is easy to inadvertently flood the chamber with water condensation; adding a viewport to the chamber would help determine when water is condensing inside.

This platform could be improved and built upon to perform a variety of experiments. We are testing different membrane materials, such as deposited SiO_2 or modifications to the current porous silicon membrane morphology, to find membranes that are more permeable or can hold higher tensions. Our preliminary experiments using the MVLE technique with porous silicon membrane indicate that tensions of 60-70 MPa can be achieved with certain samples (private communication from Eugene Choi). We are also trying to create membranes that are even less permeable, and thus create a sensor that can do pseudo-isochoric measurements. Finally, the sensor and setup presented here could be used to study a large variety of liquids under tension and measure their cavitation pressure.

Acknowledgements

This work is supported by the NSF Graduate Research Fellowship under Grant DGE-1144153 (MS) and Alfred P. Sloan scholarship (MS), the National Science Foundation (CBET-0747993

and CHE-0924463), the Air Force Office of Scientific Research (FA9550-09-1-0188), the National Institute of Food and Agriculture, U.S. Department of Agriculture (under agreement no. 2010-51181-21599). It was performed in part at the Cornell NanoScale Facility, a member of the National Nanotechnology Coordinated Infrastructure (NNCI), which is supported by NSF (Grant ECCS-15420819); and made use of the Cornell Center for Materials Research Shared Facilities which are supported through the NSF MRSEC program (DMR-1120296), and the Nanobiotechnology Center shared research facilities at Cornell.

Supplementary information

Uncertainty Analysis

Source	
Overall bridge resistance	$R = 3 \text{ k}\Omega$
Excitation current	$i = 200 \text{ }\mu\text{A}$
Average voltage output	$V_{out} = 25 \text{ mV}$
Residual resistance due to unbalanced bridge (approximated from $R_0 = \frac{V_{out}}{i} @ P = 0$)	$R_0 = 125 \text{ }\Omega$
Slope for 2mm sensor @ $i = 200 \text{ }\mu\text{A}$	$m = 3 \text{ MPa/mV}$

Table 3.4: Properties assumed in uncertainty analysis

Source	Error (\pm)
Honeywell ETJ Pressure gauge (calibration)	$\delta P_{gauge} = 35 \text{ kPa}$
Agilent 34401 Multimeter, 100mV range	$\delta V_{MM} = 4.5 \text{ }\mu\text{V}$
REF200 Power supply	$\delta i = 1 \text{ }\mu\text{A}$
PRT	$\delta T_{PRT} = 0.15 \text{ K}$
Adixen ASD 200x vacuum gauge	$\delta P_{vacuum} = 0.0025 P_{vacuum}$

Table 3.5: Sources of error in the system, from manufacturer data.

Source	Error (\pm)
Calibration voltage output, measured voltage	$\delta V = 125 \mu\text{V}$
Measured pressure in tensiometer	$\delta P = .37 \text{ MPa}$
Measured activity	$\delta a \approx 0.35\%$
χ_{red}^2 for EoS measurement at 20 °C	$\chi_{red}^2 = 0.42$

Table 3.6: Uncertainties calculated

The EoS ($P(a,T)$) at a given point depends on the measurement of the liquid pressure with the tensiometer, the vapor pressure with a vacuum gauge, and the temperature with a platinum resistance thermometer, and errors from these 3 measurements each contribute to a total uncertainty.

Liquid pressure: The error in pressure (δP) is a function of the tensiometer characteristics, and the instruments used to excite and read it.

Calibration (voltage) uncertainty: During calibration, a pressure was applied and the voltage output from the sensor was measured. For this analysis we neglected sensor drift ($\delta R \approx 0$, insufficient data) and sensor sensitivity to temperature (it was small). The pressure uncertainty was given by the pressure gauge specs δP_{gauge} . The sensor voltage output uncertainty was a combination of uncertainties in (1) the input current (δi), and the voltage readout in the multimeter (δV_{MM}):

$$\delta V = \sqrt{\left(\frac{dV}{di} \delta i\right)^2 + \delta V_{MM}^2} \quad 3.17$$

Assuming the change in resistance in the sensor is small compared to the total resistance ($\Delta R / R \approx 0$), we take $V \approx iR_0$, and eq. 3.17 becomes:

$$\delta V = \sqrt{(R_0 \delta i)^2 + \delta V_{MM}^2} = \sqrt{125^2 + 4.5^2} \mu\text{V} = 125 \mu\text{V} \quad 3.18$$

Pressure uncertainty: During operation, the tensiometer measured the pressure in its water reservoir, and this value was read as a voltage. Using a linear calibration

$$P = mV + b, \quad 3.19$$

the pressure uncertainty was a combination of pressure gauge uncertainty and voltage readout uncertainty:

$$\delta P = \sqrt{\delta P_{gauge}^2 + \left(\frac{\partial P}{\partial V} \delta V \right)^2} \quad 3.20$$

Taking the typical sensor response ($m = 3 \text{ MPa/mV}$), and using eq. 3.19 and eq. 3.20, we get

$$\delta P = \sqrt{\delta P_{gauge}^2 + (m\delta V)^2} = \sqrt{0.035^2 + 0.37^2} \text{ MPa} = 0.37 \text{ MPa} \quad 3.21$$

Temperature uncertainty: Given by the PRT manufacturer, $\delta T = 0.15 \text{ K}$.

Activity uncertainty: We begin with the equation for activity, which depends on the vapor pressure (p_{vap}) and the saturation pressure inside the chamber (p_{sat}); both of these variables were measured with the vacuum gauge. We take the temperature in the chamber to be constant.

$$a = \frac{P_{vap}}{P_{sat}(T)} \quad 3.22$$

Then the activity uncertainty was given by the combination in errors of these two quantities

$$\delta a = \sqrt{\left(\frac{\partial a}{\partial P_{vap}} \delta P_{vap} \right)^2 + \left(\frac{\partial a}{\partial P_{sat}} \delta P_{sat} \right)^2} \quad 3.23$$

Since both P_{vap} and P_{sat} were measured with the vacuum gauge, and were within 10% of each other, we took these uncertainties to be equal, and given by the gauge specifications:

$$\delta P_{vap} \approx \delta P_{sat} = 0.0025 P_{sat} \quad 3.24$$

We also assumed that activity is close to one ($a \approx 1$).

Taking the derivative of eq. 3.22, and combining it with eqs. 3.23 and 3.24 gives

$$\delta a = \sqrt{\left(\frac{1}{P_{sat}} \delta P_{vapor}\right)^2 + \left(-\frac{a}{P_{sat}} \delta P_{sat}\right)^2} \approx \sqrt{2} \delta P_{sat} = 0.0035 \quad 3.25$$

Total uncertainty in each measurement, in terms of pressure: Add up both uncertainties in chamber activity and tensiometer pressure

$$\delta P_{total} = \sqrt{(\delta P)^2 + \left(\frac{dP}{da} \delta a\right)^2} = \sqrt{(\delta P)^2 + \left(\frac{RT}{\tilde{v}} \delta a\right)^2} = \sqrt{0.37^2 + 0.47^2} \text{ MPa} = 0.60 \text{ MPa} \quad 3.26$$

Chi-squared: To evaluate the compatibility of our data with the extrapolated IAPWS and the appropriateness of our estimated uncertainties, we calculated chi-squared (χ_{red}^2), given by

$$\chi_{red}^2 = \frac{\chi^2}{\nu} = \frac{1}{\nu} \left(\frac{(x_1 - \mu_1)^2}{\sigma_1^2} + \frac{(x_2 - \mu_2)^2}{\sigma_2^2} + \dots \right) \quad 3.27$$

Where x is the measured value, μ is the expected value, $\sigma = \delta P_{total}$ is the uncertainty in the measurement, and ν is the number of degrees of freedom:

$$\nu = N - \rho - 1 \quad 3.28$$

N is the number of observations and $\rho = 0$ the number of fitted parameters. $\chi_{red}^2 > 1$ means that the experiment does not agree with the theory, and $\chi_{red}^2 < 1$ implies that the error has been overestimated. For the set of measurements presented in Figure 3.8 the average value of Chi-squared across all temperatures was $\chi_{red}^2 = 0.42$.

Porosimetry

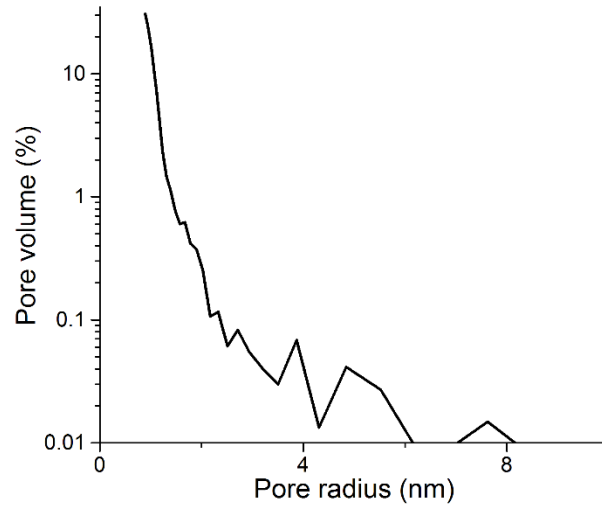


Figure 3.9: Porosimetry data on sample of porous silicon membrane used in microtensimeters for equation of state measurements.

Equation of state measurement data

Temperature (°C)	χ^2_{red}
0.5	0.64
4	0.23
8	0.57
15	0.37
20	0.38

Table 3.7: Chi-squared for measurements at each temperature.

Temperature (°C)	Vapor activity	Pressure (-MPa)
0.5	0.983	2.54
0.5	0.972	3.76
0.5	0.953	6.43
0.5	0.933	9.12
0.5	0.914	11.84
0.5	0.895	14.54
4	0.974	3.63
4	0.954	6.31
4	0.954	6.29
4	0.934	9.08
4	0.934	9.00
4	0.932	8.89
4	0.914	11.77
4	0.913	11.96
4	0.913	11.69
4	0.894	14.72
4	0.893	14.56
8	0.978	3.62
8	0.976	3.20
8	0.958	6.22
8	0.957	5.88
8	0.957	5.77
8	0.938	9.05
8	0.937	8.56
8	0.937	8.56
8	0.918	11.63
8	0.917	11.82
8	0.917	11.56
8	0.897	14.62
15	0.98	2.86
15	0.96	5.71
15	0.94	8.21
15	0.92	11.57
20	0.98	2.86
20	0.96	5.71
20	0.94	8.21
20	0.92	11.57

Table 3.8: Raw data of equation of state measurements.

CHAPTER 4

MICROTENSIOMETER PROBE FOR IN SITU WATER POTENTIAL MEASUREMENTS OF COMPLEX MEDIA: SOLUTIONS, SOILS, PLANTS.

Michael Santiago^{1*}, Winston L. Black², Siyu Zhu², Erik J. Huber¹, Adriana C. Mulero^{1,5},
Andrew M. Bryan³, Alan N. Lakso⁴ and Abraham D. Stroock^{2*}

1. School of Mechanical and Aerospace Engineering 2. School of Chemical and Biomolecular
Engineering, 3. School of Electrical and Computer Engineering, 4. Emeritus at Plant Science,
Cornell University, Ithaca NY, USA, 4. Chemical Engineering, University of Puerto Rico,
Mayagüez, PR

*E-mail: ms2343@cornell.edu and ads10@cornell.edu;

Introduction

Water generally moves along gradient of water potential, towards regions of lower potential. In a given phase—solution, vapor, or hydrated solid—water potential (Ψ [Pa]) defines the thermodynamic availability of water for physical, chemical and biological processes. Water potential is defined as the potential energy of water per unit volume with respect to pure water

$$\Psi = \frac{\mu - \mu_0}{v_l} \quad 4.1$$

where μ [J/mol] is the chemical potential of water in the system, μ_0 is the chemical potential of pure, unbound water at the same temperature and v_l is the water molar volume. The status of water influences processes in natural and technological contexts, such as biology, construction, agriculture and geology (Figure 4.1). In liquid solutions, Ψ is related to the osmotic pressure, and gradients of Ψ drive the movement of water across membranes—such as in plants, animals, cells

and synthetic osmotic membranes; these processes are of technological importance in desalination¹⁴¹, energy production¹⁴² and medical diagnostics^{143,144}. In concrete, Ψ specifies water availability for the curing reaction, and affects shrinkage⁴, cracking^{145,146}, strength, durability, porosity and pore size distribution¹⁴⁷. In foodstuffs, Ψ determines viability of bacteria and fungi growth¹⁴⁸, shelf life⁷, and properties such as texture⁵ and aroma⁶. In an agricultural context, gradients in Ψ drive water flow from soil to roots to leaves, with Ψ in the soil determining water availability for plants¹⁴⁹; in plants themselves Ψ determines produce quality and yield^{22,150}, and is the best measure of hydration²⁸, serving as a useful basis for saving water through deficit irrigation^{20,151}. Measurement of Ψ is thus very important throughout these contexts, but this variable has proven difficult to measure accurately in situ under conditions near saturation ($\Psi = 0$ MPa).

Water potential always expresses the chemical potential as the pressure of a pure liquid in equilibrium with the phase of interest. One can also express chemical potential as the RH of a vapor in equilibrium with the phase of interest. As a rule of thumb, in ambient conditions near RH = 100%, a difference of 1% RH translates to ≈ -1.4 MPa (discussed in the next section). We distinguish between four ranges of interest for Ψ measurements (see Figure 4.1): ambient humidity of air (0 – 100% RH, -1000 – 0 MPa), biological (60 – 100% RH, -70 – 0 MPa), osmotic solutions and plants (95 – 100% RH, -7 – 0 MPa), and soil (99 – 100% RH, -1.5 – 0 MPa). For reference in each of these contexts, ideal humidity for human-occupied buildings is 40 to 60% RH (-130 to -70 MPa)¹⁵²; microbial growth occurs between 60 to 100% RH (-70 – 0 MPa) and generally stops completely below 60% RH (-70 MPa)¹⁵³; seawater is $RH \approx 98\%$ ($\Psi \approx -3$ MPa), and concrete must be kept at $RH > 85\%$ ($\Psi > -23$ MPa) to cure properly; apple trees

experiencing $RH \approx 98.5\%$ ($\Psi \approx -2$ MPa) grow fruit half the size versus fully hydrated trees¹⁵⁴; the permanent wilting point of soil is commonly defined as $RH \approx 0.99\%$ ($\Psi = -1.5$ MPa)¹⁵⁵.

Similar to choosing a pressure gauge, where the decision depends on the pressure range of interest and the system measured, no universal probe for Ψ exists and instruments available are tailored to a particular range and system (Table 4.1). In the humidity and biological ranges, both in situ and ex situ instruments are available to measure Ψ accurately. In the ranges near saturation—solutions, plants, soil—benchtop instruments, such as the dewpoint hygrometer and vapor pressure osmometer are accurate and simple to use, but current in situ methods are hampered by low accuracy, errors due to large temperature sensitivity, small range, or difficulty of use. Therefore, measurements of water status in complex media near saturation are currently difficult to perform.

In this study, we proceed to fill this gap by developing an in situ probe, a microtensiometer designed with adequate accuracy and range for measurements near-saturation in solutions, plants, soils and other complex media. We report on measurements performed with this microtensiometer said probe in osmotic solutions, soil, and plants. The sensor presented here is a miniaturized tensiometer, which brings a number of advantages relative to conventional tensiometers: larger range, smaller sensitivity to temperature gradients, and compatibility with in-situ point measurements. This sensor is based on the previously published microtensiometer (Ch. 3)¹³⁰, but has been redesigned and made into an embeddable probe. The probe thus designed has dimensions of 20 mm \times 7 mm \times 2 mm, accuracy comparable to laboratory instruments (0.3 MPa), takes continuous analog measurements, equilibrates in 15-20 minutes, is robust enough for field measurements, and has range over 80 \times of common tensiometers (-8 MPa).

This paper is organized as follows. First, we review the components that make up Ψ and the variety of instruments available to measure it, then briefly introduce tensiometry—the working principle behind our sensor. Second, we overview the sensor design and functioning, do a thorough analysis of various aspects of the sensor, and describe in detail the process of sensor fabrication, calibration and use in various contexts. Third, we present and discuss results of the sensor characteristics and measurements performed in osmotic solutions, soil, and plants (apple and grape stems).

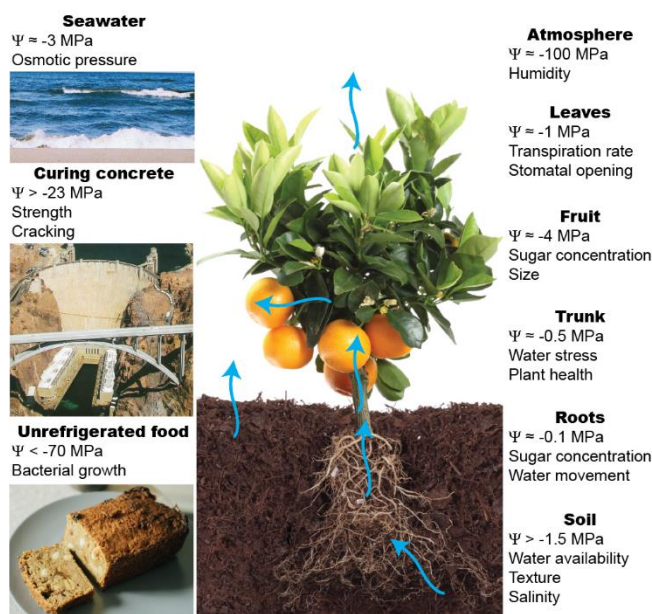


Figure 4.1: Water potential (Ψ) in natural and technological contexts. Ψ represents the availability of water for chemical and physical processes in contexts such as the sea, concrete, food, and the soil-plant-atmosphere continuum. Typical values shown for each context. Blue arrows depict water movement due to gradients in Ψ . Orange tree figure © Filipe Varela | Dreamstime.com

Components of and instruments to measure water potential

The value of Ψ combines multiple components that together determine the partial molar free energy of water at a given point. For a liquid phase, Ψ is the sum of components due to pressure ($\Psi_{pressure}$), osmolites ($\Psi_{osmotic}$), gravity ($\Psi_{gravity}$) and solid-liquid interactions (Ψ_{matric}):

$$\begin{aligned}\Psi &= \Psi_{pressure} + \Psi_{osmotic} + \Psi_{gravity} + \Psi_{matric} \\ \Psi_{pressure} &= P - P_0 \\ \Psi_{osmotic} &= -\frac{RT}{v_l} \ln(a_w) \\ \Psi_{gravity} &= \rho g z\end{aligned}\tag{4.2}$$

Where P [Pa] is the liquid pressure, P_0 reference pressure [Pa], $R = 8.314$ J/(mol.K) the ideal gas constant, T [K] temperature, v_l [m³/mol] water molar volume, a_w water activity, ρ [kg/m³] fluid density, $g = 9.81$ m²/s the gravitational constant and z [m] height. The Ψ_{matric} component is a catch-all term that describes interactions between water and its host medium, such as capillary interactions in porous materials or the chemical interactions that define swelling behavior in hydrogels.

For a gas, Ψ is the sum of humidity ($\Psi_{humidity}$) and gravity components:

$$\begin{aligned}\Psi &= \Psi_{humidity} + \Psi_{gravity} \\ \Psi_{humidity} &= \frac{RT}{v_l} \ln(RH)\end{aligned}\tag{4.3}$$

where $\Psi_{gravity}$ is the same as for the liquid (eq. 4.2).

Multiple instruments have been developed to measure Ψ (Table 4.1). The most common method to measure Ψ is through the Ψ_{matric} component, in which a calibrated porous or gel-like material

has properties—electrical capacitance or resistivity or thermal conductivity—that change with Ψ . As Ψ drops, the material gradually releases water, its properties change, and this change is measured by electrical circuitry and compared against tabulated Ψ values. Unfortunately, these sensors typically provide accuracy ($\Delta\Psi > 0.7$ MPa)¹⁵⁶ that is sufficient for important contexts such as soil and plants.

Second class of tools—chilled mirror dew point hygrometry or psychrometry—measure a sample's water potential via the dew point depression in a gas with which it is at equilibrium. The gas RH is measured through methods such as chilled mirror dew point hygrometry or wet bulb depression (psychrometry). A challenge with these methods is that $\Psi_{humidity}$ is exceptionally sensitive to temperature: at ambient conditions when measuring across a vapor gap, an uncorrected temperature difference between the sensor and measured media of 1 °C leads to an error of ~8 MPa because of the temperature dependence of p_{sat} ($\Psi_{humidity}$ term in eq. 2)¹⁵⁷.

For comparison, the permanent wilting point of soil is commonly defined as $\Psi = -1.5$ MPa¹⁵⁵, and for apple trees under deficit irrigation with $\Psi \approx -2$ MPa, their fruit grow half as much as fully irrigated apple trees¹⁵⁴. Therefore, to achieve an accuracy of ~5% on Ψ in this range (0.1 MPa), these methods necessitate temperature control or measurement to an accuracy of 0.01 °C. Available *in situ* psychrometers require specialized electronics and exhibits scatter and systematic errors at $\Psi > -1$ MPa¹⁵⁸, factors that have limited its use outside of research contexts.

Osmometers are a third class of tools for measuring Ψ . These devices measure colligative properties of solutions such as freezing point, boiling point and osmotic pressure to assess $\Psi_{osmotic}$

. In freezing point osmometry, the sample is quickly cooled until it freezes, then slowly heated until it melts at the Ψ -depressed melting point¹⁵⁹. This technique is limited to low viscosity liquids, and can only measure Ψ at the freezing point, whereas Ψ in a solution varies with temperature¹⁶⁰. In membrane osmometry, a fluid sample is equilibrated with a known solution through a semi-permeable membrane; after a suitably long time for equilibration, the pressure at the sample side is measured to give the osmotic pressure¹⁶¹. This technique is generally slow, and is limited to osmolytes that are compatible with the membrane (do not damage it) and larger than the membrane pores. Both methods also necessitate handling the fluid in a controlled environment and thus are generally limited to benchtop instruments.

A fourth class of techniques isolate $\Psi_{pressure}$ which can be measured as a mechanical pressure. This method has potential for the highest accuracy, since small changes in water status correspond to large, easily measured pressures. For instance, at 25 °C a drop in gas RH or liquid activity (a_w) from 100% to 99% corresponds to a change in pressure of -1.4 MPa (eq. 4.2); since inexpensive pressure transducers commonly have accuracy better than 0.01 MPa, pressure methods make it in theory possible to measure changes in humidity down to accuracy better than 0.01%. Methods that measure Ψ as a pressure include the pressure bomb¹⁶², the pressure plate¹⁶³ and tensiometry¹⁶⁴. In the bomb method, a leaf cut at the stem is placed in a pressure chamber with the stem sticking out and air pressure is applied to the leaf to ‘balance’ the negative Ψ that existed in the leaf before excision; when liquid water begins to come out of the stem the negative of the applied pressure is interpreted as the value of Ψ ¹⁶². This method has proven useful for agriculture, but is labor-intensive—requiring manual measurements, often before dawn or at solar noon. In the pressure plate method, a soil sample is taken from the site of interest, is fully hydrated, and is placed in a

large pressure chamber with a porous ceramic plate at the bottom. Then, one applies air pressure within the chamber to simulate a desired Ψ in the sample and squeeze out water from the soil through the ceramic plate; the resulting change in water content of the soil is measured at each applied pressure based on the volume of water exuded. Unfortunately this method takes days to equilibrate for each measurement point (water stops flowing), can only be performed with disturbed soil samples (not in situ), is inaccurate for $\Psi < -0.2$ MPa¹⁶⁵, and does not directly measure Ψ , but instead measures the soil water retention for a particular value of Ψ . In the tensiometry method, an enclosed volume of pure liquid water equilibrates with the sensed environment through a wettable porous membrane, and the liquid pressure drops until it reaches the value of Ψ in the surrounding environment. The range of this method is generally limited to $\Psi > -0.1$ MPa by boiling of the reference liquid water. We note that tensiometers and membrane osmometers both measure Ψ as a difference in pressure across a membrane, but have the following differences: (1) the reference liquid in a membrane osmometer is a large-molecule solution of known activity (not pure water) and (2) the membrane for osmometry is impermeable to the osmolytes of interest (the tensiometer membrane is indiscriminate to osmolytes). The sensor developed here is based on the tensiometry method and thus this method is analyzed in more detail in the next section.

Instrument	Range (MPa)	Accuracy (\pm MPa)	Measure time (min)	in situ	Ψ technique	Usual context	Comments
Capacitive ¹⁶⁶⁻¹⁶⁸ or resistive humidity probe ¹⁶⁹	0 to -1000	0.7 to 3	1	Y	Ψ_{matric}	atmospheric, soil	Poor accuracy, low cost.
Chilled mirror hygrometer ¹⁷⁰	-0.1 to -300	0.05	15	N	Ψ_{humidity}	solutions, food, soil	Expensive, inaccurate near saturation, large range.
Vapor pressure osmometer ¹⁷¹	0 to -9	0.005	1.5	N	Ψ_{humidity}	solutions	Not good for volatile solutes.
Stem psychrometer ¹⁷²	0 to -10	0.1	1	Y	Ψ_{humidity}	atmospheric, plants	Expensive, requires a nano voltmeter with precise temporal control of excitation and measurement.
Freezing point depression osmometer ¹⁷³	0 to -10	0.005	2 - 3	N	Ψ_{osmotic}	solutions	Expensive, limited to dilute and low-viscosity liquid samples.
Membrane osmometer ¹⁷⁴	0 to -25	0.03	> 20	N	Ψ_{osmotic}	solutions	Can measure concentrated solutions.
Soil tensiometer ¹⁷⁵	+0.1 to - 0.08	0.0005	< 1	Y	Ψ_{pressure}	soil	Highest available sensitivity near saturation, limited to small range near saturation.
Microtensiometer (this paper)	0 to -8	0.3	20	Y	Ψ_{pressure}	solutions, soil, plants	Small form factor, requires filling under high pressure before use.
Pressure plate ¹⁷⁶	-0.01 to - 1.5	-	days	N	Ψ_{pressure}	soil	Large form factor, very slow, equilibrates soil to desired Ψ .
Scholander pressure chamber ¹⁷⁷	0 to -10	0.2	1	Y	Ψ_{pressure}	plants	Requires skilled operator, manual measurement, destroys a leaf.
Hanging column ¹⁷⁶	0 to -0.08	-	days	N	Ψ_{gravity}	soil	Large setup, equilibrates soil to desired Ψ .

Table 4.1: Comparison of instruments available to measure water potential (Ψ). Range and accuracy specifications converted to Ψ from osmolality or relative humidity.

Methods

Brief introduction to tensiometry

Tensiometers use the equilibrium between the sensed sample and an internal volume of pure water to measure Ψ as a pressure difference. Tensiometers consist of (1) a macroscopic reservoir of pure liquid water, (2) a pressure transducer that measures the pressure of this reservoir, and (3) a porous membrane that allows the exchange of water between the reservoir and the sample (see Figure 4.2a). As Ψ drops in the sample, water leaves the tensiometer reservoir through the porous membrane such that the pressure in the liquid reservoir ($P_{reservoir}$) drops as well, and the measured pressure difference at equilibrium (ΔP_{tensio}) equals the drop in pressure from atmospheric (P_{atm}):

$$\Delta P_{tensio} = P_{reservoir} - P_{atm} = \Psi. \quad 4.4$$

In effect, the tensiometer translates the sample Ψ into a pressure ($\Psi_{pressure}$) that it can then measure ($\Psi = \Psi_{pressure}$) as a mechanical pressure difference, ΔP_{tensio} .

This pressure difference is maintained by capillary sealing in the membrane, as liquid water in the pores prevents the invasion of air in the reservoir (expanded view at bottom of Figure 4.2A). Air from the outside can penetrate through the pores when the pressure difference is larger than the pores can hold, a process known as capillary breakthrough. The maximum pressure difference a porous membrane can hold is set by the largest pore connecting the reservoir and the outside by the Young-Laplace equation:

$$|\Delta P_{tensio}| < \frac{4\gamma \cos \theta}{d_{p,max}} \quad 4.5$$

where γ [J/m²] is the surface tension of water, θ the contact angle of water in the pores, and $d_{p,max}$ is the diameter of the largest pore connecting reservoir and sensed environment. For example, a 1

μm diameter pore limits measurements to $\Delta P_{tensio} > -0.3 \text{ MPa}$, and a 30 nm diameter pore limits measurements to $\Delta P_{tensio} > -10 \text{ MPa}$.

Out of all methods to measure Ψ , tensiometry has a demonstrated accuracy that can be tenfold higher (0.0005 MPa) than any other technique (Table 4.1), is compatible with small form factors and in situ measurements, and is used commercially as an in situ probe for measuring soil Ψ . Unfortunately, most tensiometry is handicapped by its very narrow working range of 0 to -0.1 MPa. To measure $\Psi < -0.1 \text{ MPa}$, the liquid inside the reservoir must be under mechanical tension ($P_{reservoir}$), a metastable state that is difficult to maintain. The measurement range is thus set by a combination of two factors in the reservoir water: capillary breakthrough and boiling nucleation. Reported capillary breakthrough pressures in tensiometer porous ceramic membranes are 0.43 – 0.8 MPa¹⁷⁸, corresponding to pore diameters of ~300 to 700 nm. Generally, a liquid will boil when its pressure decreases below p_{sat} , but this process needs a nucleation site, such as gas bubbles or non-wettable impurities. To prevent boiling and perform measurements below -0.1 MPa, boiling nucleation sites in the reservoir must be eliminated by completely degassing the liquid, thoroughly polishing and cleaning the surfaces contacting the water, and using purified water. Unfortunately, in the large volume of water contained in common tensiometers, it is impossible to eliminate all nucleation sites, so these steps often only allow measurements down to -0.1 MPa before the reservoir water boils¹⁷⁵.

Overview of sensor components and function

The microtensiometer contains the same components as a soil tensiometer, with modifications (Figure 4.2B-E): (1) pressure-sensing diaphragm, (2) serpentine platinum resistance thermometer

(PRT), (3) water-filled reservoir, (4) water-channel network and (5) nanoporous membrane that provides a continuous liquid connection between the water reservoir and the sensed environment. The sensor consists of a piece of silicon onto which all the components are deposited or etched. The water reservoir and porous membrane system are etched on the bottom side of the silicon and a borosilicate glass wafer is bonded to this side, sealing the reservoir (see Figure 4.3). The resulting silicon-glass sandwich sits on a custom printed circuit board (PCB), and is encapsulated with epoxy with either a flat (shown in Figure 4.2) or cylindrical form factor. The silicon top side has four polysilicon piezoresistors connected by platinum wires in a Wheatstone bridge configuration that make up a pressure gauge¹⁷⁹. During measurements, the pressure in the reservoir drops relative to atmospheric pressure, this pressure difference causes the diaphragm to deflect and produces strain in the piezoresistors. Under strain, the piezoresistors' electrical resistance changes, and this leads to a change in voltage across the Wheatstone bridge, which we measure with a multimeter.

The microtensiometer was built using microfabrication in a cleanroom, a process that enabled various improvement over conventional tensiometers: 1) miniaturization of the sensor over 100× in linear dimension; 2) reduction in the water volume in the reservoir to ~20 nL (vs ~mL volumes); and 3) incorporation of a nanoporous membrane with pores 2 – 4 nm in diameter¹³³ (vs ~100 nm diameter). Furthermore, microfabrication in a cleanroom minimizes contaminants in the internal volumes, and after sealing, the internal cavity is protected from entry of most impurities (larger than ~4 nm) by the passage of water through the nanoporous Si membrane. These features minimize nucleation sites and enable the sensor to operate down to $\Psi \approx -8$ MPa or lower¹³⁰.

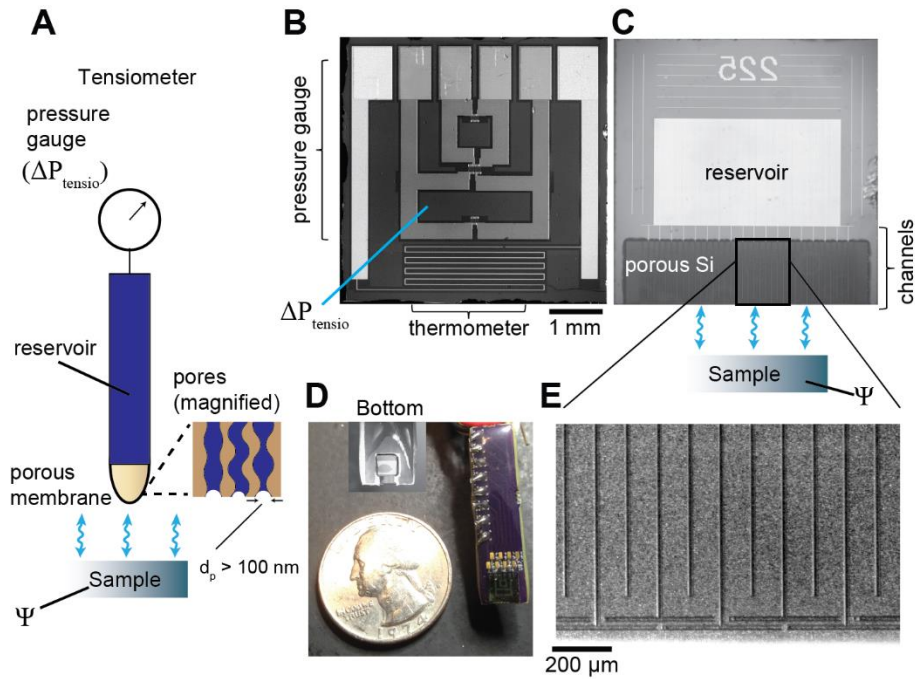


Figure 4.2: Illustration of conventional tensiometer and microtensiometer. (A) Conventional tensiometer holds a volume of water that decreases in pressure (ΔP_{tensio}) until it reaches the sample water potential (Ψ). (B) Microtensiometer top view shows wiring and bond pads for Wheatstone bridge pressure gauge and platinum resistance thermometer (PRT). Piezoresistors are placed vertically along the horizontal center of the diaphragm. (C) Microtensiometer bottom view shows water-filled reservoir, the array of channels connected to it, and porous silicon membrane. Sensors are individually numbered. Porous silicon membrane is patterned to only connect with the front edge of the sensor. (D) Chip is wirebonded to a custom circuit board and this setup is encapsulated with epoxy; the front side is not covered by encapsulant to allow water exchange. (E) Channel array built to improve water transport between reservoir and sample. Straight channels are connected to the main reservoir and ‘T’ shaped channels approach but are not connected to the sensing edge.

Pressure diaphragm sensitivity

We followed design recommendations from the extensive literature on diaphragm pressure sensors to decide on the diaphragm-piezoresistor configuration^{180–182}. Compared to circular or square diaphragms, a rectangular diaphragm gives the largest stress response per unit area and reduces diaphragm deflection¹⁸³; this characteristic is beneficial for response time (discussed below). Four

different diaphragm sizes were used in this study: 1 mm × 2 mm, 1.5 × 3 mm, 2 × 3.5 mm, 3.5 × 4 mm. As will be seen below, devices with larger diaphragms provide better sensitivity to Ψ , but have longer equilibration times. For doped-polysilicon resistors, placement on the diaphragm's horizontal center produces the largest signal, since the orientation of stress concentration coincides with the strongest piezoresistor response orientation (lengthwise)¹⁸⁰. Piezoresistors were doped to $6 \times 10^{19} / \text{cm}^3$ to achieve large signal, while keeping low temperature sensitivity¹⁸⁰. The piezoresistor resistance was chosen to be 2 k Ω (relative to the conventional 300 Ω used in diaphragm pressure sensors) to minimize energy use, ohmic heating, and sensitivity to lead and contact resistances.

For a rectangular diaphragm, the maximum deflection (w_{center}) occurs in the center. The maximum tensile (σ_{center}) and compressive stresses (σ_{max}) occur along the middle of the rectangle's length, σ_{center} in the center of this line, σ_{max} where this line intercepts the diaphragm edge. These quantities are given by¹⁷⁹:

$$w_{center} = \frac{\alpha \Delta P_{tensio} b^4}{E t_d^3} \quad 4.6$$

$$\sigma_{center} = \frac{\beta_2 \Delta P_{tensio} b^2}{t_d^2} \quad 4.7$$

$$\sigma_{max} = \frac{\beta_1 \Delta P_{tensio} b^2}{t_d^2} \quad 4.8$$

Where a and b are the diaphragm length and width respectively, α , β_1 and β_2 are tabulated values depending on the length to width ratio of the diaphragm (a/b), $E = 107,000$ MPa is the Young modulus for Si, and $t_d \approx 300$ μm is the diaphragm thickness. Note that for an expected

maximum pressure difference expected (ΔP_{max}), the reservoir underneath the diaphragm must be etched a depth (w_{etch}) of at least (from eq. 4.6)

$$w_{etch} > \frac{\alpha \Delta P_{max} b^4}{Et_d^3} \quad 4.9$$

Otherwise, the diaphragm will touch the reservoir bottom as it deflects and this will give erroneous results.

The change in resistance ($\Delta R_{res} / R_{res}$) of a single piezoresistor is given by:

$$\begin{aligned} \frac{\Delta R_{res}}{R_{res}} &= \pi_l \sigma_x + \pi_t \sigma_y \\ \pi_l &= \frac{K_l}{E}; \pi_t = \frac{K_t}{E} \end{aligned} \quad 4.10$$

Where $K_l = 21$ and $K_t = -8$ are the longitudinal and transversal gauge factors for polysilicon doped with co-deposited boron¹⁸⁴, $\pi_l = 2 \times 10^{-4} \text{ MPa}^{-1}$ and $\pi_t = 0.7 \times 10^{-4} \text{ MPa}^{-1}$ are the longitudinal and transversal piezoresistive coefficients for polySi respectively, and σ_x and σ_y are the longitudinal and transversal stresses respectively. Given our placement of piezoresistors vertically along the diaphragm's horizontal middle, the transversal stresses are small and can be neglected. For the edge resistors, the change in resistance ($\Delta R_{res,1} / R_{res}$) is:

$$\frac{\Delta R_{res,1}}{R_{res}} \approx \pi_l \sigma_{max}, \quad 4.11$$

and for the center resistors, the change in resistance ($\Delta R_{res,2} / R_{res}$) is :

$$\frac{\Delta R_{res,2}}{R_{res}} \approx \pi_l \sigma_{center}. \quad 4.12$$

Then the Wheatstone bridge signal (V_{out}) per applied current (i_{in}) is given by:

$$\frac{V_{out}}{i_{in}} = \frac{\Delta R_{res,1} - \Delta R_{res,2}}{2} \quad 4.13$$

Combining eqs. 4.7, 4.8, and 4.11-4.13, the bridge signal is given by:

$$\frac{V_{out}}{i_{in}} \approx \frac{\pi_l R_{res}}{2} (\sigma_{max} - \sigma_{center}) = \frac{\pi_l R_{res} \Delta P_{tensio} b^2}{2t_d^2} (\beta_1 + \beta_2). \quad 4.14$$

Diaphragm breaking pressure

The diaphragm will break when its maximum stress (σ_{max}) exceeds the silicon yield stress ($\sigma_y = 7,000$ MPa). The breaking pressure (ΔP_{break}) is calculated from eq. 4.8:

$$\Delta P_{break} = \frac{t_d^2}{\beta_1 b^2} \frac{\sigma_y}{SF} \quad 4.15$$

Where $SF = 15$ is the safety factor that takes into account the stress concentrations due to the etching process and the diaphragm corners, chosen from previous experience.

Pressure equilibration time

Given a step change in Ψ , the pressure in the microtensiometer reservoir relaxes to the final value over a characteristic time τ . This process is modeled like an RC circuit such that the predicted time dependence of the response is:

$$\frac{\Delta P_{tensio} - \Psi}{\Delta P_{tensio,0} - \Psi} = \exp\left(\frac{-t}{RC}\right) \quad 4.16$$

Where $\Delta P_{tensio,0}$ is the initial pressure reading in the diaphragm, t is time, C [m^3/Pa] is the system capacitance, and R [$\text{Pa}\cdot\text{s}/\text{m}^3$] is the resistance to flow from the reservoir to the outside. From eq. 4.16 the time constant for pressure equilibration is $\tau = RC$. To decrease τ for faster measurements, we designed the reservoir and channel structure to minimize both R and C . We

made the following assumptions: neglected boundary layer limitations outside the membrane, neglected resistance in the reservoir and channels, and assumed pressure in porous silicon equilibrates much faster than does ΔP_{tensio} .

Diaphragm capacitance

The system capacitance is given by the reciprocal sum of capacitances associated with stretching of the liquid water and deformation of the diaphragm:

$$C = \left(\frac{1}{B_w} + \frac{1}{B_r} \right) V_w \quad 4.17$$

Where $B_w = 2.2$ GPa is the bulk modulus of water, V_w is the total volume of water in the system (reservoir + channels + porous Si pores), and B_r is the effective modulus of the diaphragm. Since the volume of water in the channels is negligible, V_w is given by

$$\begin{aligned} V_w &= V_d + A_{poSi} d\phi \\ V_d &= abw_{etch} \end{aligned} \quad 4.18$$

Where A_{poSi} is the etched area of porous Si, with porosity $\phi = 0.45$, and $V_d = abw_{etch}$ the volume of water in the reservoir. B_r is given by:

$$B_r = V_d \frac{\Delta P}{\Delta V_d}, \quad 4.19$$

where the change in volume per unit pressure is governed by the 3-D deflection of the diaphragm and can be calculated using finite element analysis, or with an infinite sum series¹⁸⁵. Here, for simplicity, we approximate the diaphragm deflection as if it were a circular diaphragm with equal surface area to the rectangular diaphragm, such that its radius is $r = \sqrt{ab/\pi}$. The volume of water displaced by the diaphragm is given by the average deflection (w_{avg}) times the diaphragm area

$$\Delta V_d = abw_{avg} . \quad 4.20$$

w_{avg} in a circular diaphragm is¹³⁴

$$w_{avg} = \frac{r^4 \Delta P}{64D} , \quad 4.21$$

where D is the flexural rigidity, given by

$$D = \frac{Et_d^3}{12(1-\nu^2)} \quad 4.22$$

and $\nu = 0.27$ is the silicon Poisson ratio.

We combine Eqs 4.18-4.22 to get

$$B_r \approx V_d \left(\frac{1}{abw_{avg}} \right) = \frac{16}{3} \frac{w_{etch} Et_d^3}{r^4 (1-\nu^2)} . \quad 4.23$$

Equation 4.23 shows that the diaphragm bulk modulus scales with the cube of diaphragm thickness and the fourth power of the effective lateral dimension of the diaphragm, r . Although a wider or thinner diaphragm will have higher sensitivity (eq. 4.14), unfortunately it will also have higher system capacitance and thus response time, τ . To mitigate this compromise, we (1) minimized the total volume of water (V_w) in the system by etching a shallow reservoir and narrow channels, and (2) minimized the diaphragm deflection (and thus the $\Delta P / \Delta V_d$ term) by choosing a rectangular-shaped diaphragm. The final diaphragm size (length, width and thickness) is a compromise between sensitivity and equilibration time.

Porous membrane resistance and xylem-mimetic channels

The sensor channel structure was inspired by the vascular networks of plants, known as xylem. In plants, this structure consists of a highly redundant network of large vessels 10 to 50 μm in

diameter that are interconnected by thin membranes with nanometer sized pores. These thin membranes prevent cavitation in one vessel from spreading to another because capillary pinning in the nanopores only allows the movement of water—not gas—through the pores (eq. 4.5). Xylem thus transports water through large, low resistance vessels with short passages through nanoporous membranes; this segmented structure ensures cavitation events are localized.

Figure 4.3 presents our adaptation of the xylem structure to decrease the resistance to flow between the sensor reservoir and the sample, while also preventing cavitation; Figure 4.2C and E present images of these features. Our structure consists of multiple, parallel channels of micrometer cross-sectional dimension for water flow, interconnected by membranes of nanoporous silicon. This two-channel structure, where no reservoir-connected channel is near the device’s edge, minimizes the possibility of any single defect in the membrane from creating a continuous path from the outside to the reservoir (red dots in Figure 4.3). Sources of defects include oversized pores created by particles trapped in the Si-glass interface, poorly bonded areas, or errors in photolithography.

The flowrate (Q) between reservoir and outside is:

$$Q = \frac{1}{R}(\Delta P_{tensio} - \Psi) \quad 4.24$$

To derive an expression for the overall resistance R , we analyze this network as a hierarchy of effective resistances (see Figure 4.3). Starting from the reservoir, in each repeated unit of channels, water first travels to the T-shaped channel that is closest to the edge, following two parallel paths: through a resistance R_1 directly to this channel, or through the combination of resistances R_1

(reservoir to channel) and R_2 (channel to channel). Next, water travels between this channel and the device edge through a resistance R_2 . The resistances R_1 and R_2 are given by:

$$R_1 = \frac{w_1}{\kappa d L_1} \quad 4.25$$

and

$$R_2 = \frac{w_2}{\kappa d L_2} \quad 4.26$$

where $L_1 = 1250 \mu\text{m}$ and $L_2 = 400 \mu\text{m}$ are the vertical and horizontal lengths of one T-channel, $w_1 = 100 \mu\text{m}$ and $w_2 = 20 \mu\text{m}$ the distances crossed by water across porous silicon, $\kappa \approx 2 \times 10^{-17} \text{ m}^2/(\text{Pa}\cdot\text{s})$ the Darcy permeability of our porous Si¹³³ and $d \approx 5 \mu\text{m}$ the depth of porous Si. The overall resistance is thus given by:

$$R \approx \frac{1}{n} \left(\frac{1}{R_1} + \frac{1}{R_1 + R_2} \right)^{-1} + \frac{R_2}{n} \quad 4.27$$

where $n = 18$ is the number of repetitions of the T-channel and reservoir-connected channel pattern. To decrease overall system resistance, we (1) maximize the number of channels in parallel (n), (2) increase the channel-to-channel exchange area with a large L_1 , (3) increase the channel-to-edge exchange area with a large L_2 and (4) decrease the water path distance through the low-permeability porous silicon with small w_1 and w_2 .

Platinum wiring

All wiring is made of platinum to withstand corrosion. We found that aluminum wires would often corrode in wet conditions, even with passivation layers and packaging. We designed the PRT to

have similar resistance to the Wheatstone bridge such that it would be compatible with the same current source, in series. It is interrogated by 4 wires to minimize errors due to wire resistance.

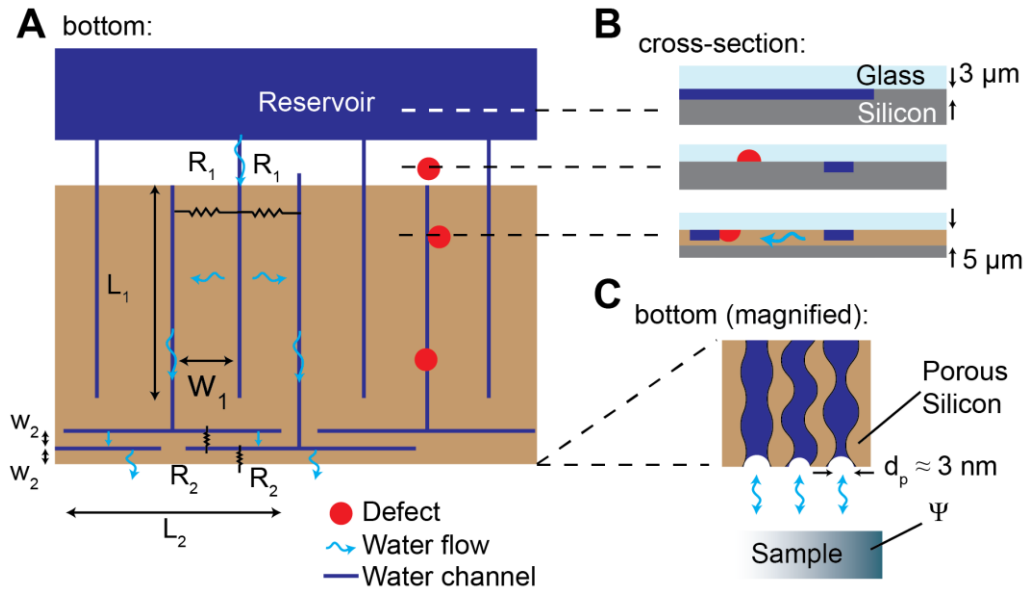


Figure 4.3: Xylem-mimetic channel network. (A) Illustration of xylem network, designed to lower flow resistance between environment and sensor reservoir, while preventing air invasion and isolating cavitation events. Drawing shows water-filled reservoir, zone of porous silicon membrane (brown), and array of channels. Channel array consists of channels connected to the main reservoir (vertical length through porous silicon $\sim L_1$) and two layers of 'T' shaped channels that terminate near the sensing edge (horizontal length $\sim L_2$). Water travels through porous silicon a distance w_1 between channels, a distance w_2 between 'T' channels, and a distance w_2 between 'T' channel and the sensed environment. Keeping reservoir-connected channels separated from the edge and other channels prevents defects (red circles) from connecting the sensed environment to the water reservoir, a flaw that would lower the device stability limit due to meniscus invasion. (B) Cross sectional view of the reservoir, a channel in plain silicon, and two channels in porous silicon. (C) Magnified view of the interface between porous silicon membrane and sample.

Microfabrication

The microtensiometer was fabricated using standard microfabrication processes in the Cornell NanoScale Science and Technology Facility cleanroom, with the exception of the electrochemical porous Si etch step that was done in a chemistry hood outside the cleanroom. The process is depicted in Figure 4, and described below; the numbered steps correspond to those in the figure.

(i) Piezoresistors and oxide insulation: Fabrication was done with 100 mm <111> 1-10 Ω -cm Si wafers. The wafers were first RCA cleaned. For electrical insulation, 800 nm of thermal SiO₂ was grown in a furnace (wet oxidation without HCl, T = 1000 °C) for 200 min. For the piezoresistors, 800 nm of p⁺-doped polySi (target: 6×10^{19} carriers/cm³) was deposited in a low pressure chemical vapor deposition (LPCVD) furnace with B₂H₆ and SiH₄ gases (B₂H₆:SiH₄ ~ 0.045) at 620 °C. Wafers were annealed at 900 °C for 30 minutes to increase polySi linearity. Piezoresistors were then patterned in the polySi layer with photolithography and dry etched in SF₆/O₂ plasma. SiO₂ was patterned, then dry etched with CHF₃/O₂ plasma. Then wafer front side was protected with layer of photoresist, and backside polySi + SiO₂ were removed with SF₆/O₂, followed by CHF₃/O₂ plasma.

(ii) Backside reservoir: The backside was patterned photolithographically with the reservoir/xylem mask, and this pattern was etched into the Si wafer with SF₆/O₂ plasma to a depth of ~3 μ m.

(iii) Pattern and etch porous Si: All photoresist was removed and wafers were cleaned in a Nanostrip bath, then dipped in buffered oxide etch (BOE) 6:1 for 5 seconds until front side wafer surface around the grown SiO₂ was hydrophobic to ensure good ohmic contact. Then 200 nm of

aluminum was conformally evaporated with e-beam on wafers to create a uniform electrical contact for the subsequent electrochemical porous silicon etch. This layer was annealed in a rapid thermal anneal machine (RTA) for 2 minutes at 400 °C to improve Al-Si ohmic contact. Annealing time was minimized, and temperature controlled carefully to minimize pitting of polySi piezoresistors by the aluminum. The wafer backside was patterned for the porous silicon etch with a special photoresist (AZ Electronic Materials, AZP4903) that can better withstand Hydrofluoric acid (HF)^{186,187}: 6 μm thick AZP4903 photoresist was spun, baked at 115 °C 3 min, was left to rest 30 – 60 min, then exposed in contact aligner, and developed with AZ421K developer for 4 minutes. We used a single-side wafer holder to develop the wafer, since developer etches the backside aluminum. Porous Si was then electrochemically etched 5 minutes in a solution of 50:50 of 49%HF:non-denatured Ethanol, with a current density of 20 mA/cm² of exposed area. Wafers were rinsed in water and cleaned with acetone then isopropanol to remove resist and left to dry. Topside aluminum was removed with AZ 300 MIF developer, only exposing the top side as developer attacks porous Si. Wafers were cleaned in Acetone, IPA, then spin rinsed. The porous silicon was annealed in pure oxygen at 700 °C for 30s in RTA tool.

(iv) Anodic bond of Si and borofloat: Si wafer side with porous Si was anodically bonded to a 100 mm, 500 μm thick borofloat wafer to create the water reservoir and xylem structure. The borofloat wafer was cleaned in Nanostrip, then both wafers were plasma cleaned at 150 W for 4 min. Wafers were placed in SuSS SB8e bonder under the following conditions: vacuum, top/bottom temperature of 400/378 °C to minimize stresses by matching the coefficient of thermal expansion in both wafers¹⁸⁸, -1500 V applied—high voltage was needed to bond with a porous Si layer—for

20 minutes to ensure a good bond, current limited to -15 mA, 3000 mbar of pressure applied to keep wafers in place.

(v) Platinum wires and PRT: Lift-off photoresist procedure was used to pattern the PRT and wires for the Wheatstone bridge. Wafers were dipped in 6:1 BOE ~5 seconds to remove surface oxide from polysilicon and ensure good ohmic contact with metals to be deposited. A sandwich of 15/200/15 nm of Ti/Pt/Ti was deposited with e-beam evaporation. Bottom Ti ensures adhesion to bottom substrate, top Ti ensures adhesion of passivation layer to be deposited subsequently. Platinum was not annealed because the bonded silicon-borofloat pair would break if exposed to high temperatures, but contact was still good because polySi was highly doped and the polySi-Pt contact area was large.

(vi) Passivation, vias and dicing: A passivation stack of $\text{SiO}_2/\text{SiN}_x/\text{SiO}_x\text{N}_y$ (400/300/200 nm) was deposited with PECVD at 200 °C. Layers were matched in thickness and intrinsic stress to give near zero total film stress. Vias—openings to make electrical connection with the platinum contact pads—were dry etched through the passivation using CHF_3/O_2 , and subsequently wet etched 1 min in BOE 30:1 to remove Ti layer on top of the contact pads. Wafer was diced carefully so that dicing edge falls ~20 microns below xylem structure. Dicing accuracy was crucial: if dicing cuts into the reservoir-connected channels the sensor will not hold tension, but dicing far from xylem T-channels would increase sensor response time.

(vii) Mounting on PCB, wirebonding, soldering, encapsulation: A custom PCB (Oshpark) was designed to interface with the sensor, consisting of a place to glue the sensor, wirebond pads, and

plated holes for soldering wires (Fig. 2D). All the wiring in the PCB was made with ENIG plating to enable wirebonding. Sensor was adhered to the PCB using epoxy, then the contact pads were ultrasonically wirebonded to the PCB with aluminum wire. Wires were soldered to the PCB, then board was cleaned by sonication in a 50:50 Acetone:IPA solution and plasma cleaning to ensure removal of solder flux and a pristine surface for encapsulation. The sensor and PCB were then encapsulated with urethane or epoxy while keeping the front (sensing) edge free of encapsulant.

(viii) Calibration of pressure and temperature, filling with water: Sensor pressure sensitivity (m) was calibrated in a pressure chamber using compressed air at room temperature (Figure 4.5). Sensor pressure offset (V_0) was calibrated for its slight temperature dependence by placing the sensor in a temperature controlled bath and measuring $V_0(T)$ at 3 temperatures that cover the range of interest: 15, 25 and 35 °C. Using these measurements, a linear fit with offset $V_0(0^\circ\text{C})$ and slope (m_T) was created. The final calibration equation for each sensor is the following:

$$V_{out}(P, T) = V_0(0^\circ\text{C}) + m_T T + m \Delta P_{tensio} \quad 4.28$$

The sensor PRT was also calibrated in a temperature-controlled bath with the previous 3 temperatures, and fitted to the linear equation (Figure 4.7):

$$R_{PRT}(T) = R_0(0^\circ\text{C}) + \alpha T \quad 4.29$$

Both pressure diaphragm and PRT were powered by a 200 μA current source, and their voltage output read by a multimeter.

Sensors were placed in 1000 psi high-pressure water overnight to fill with water. If the sensor was allowed to equilibrate with an environment where Ψ was below its stability limit ($\Psi < -8 \text{ MPa}$

), it would cavitate and need refilling. For instance, we found that sensors exposed to 50% humidity would cavitate within a minute. Therefore, full tensiometers are stored in liquid water.

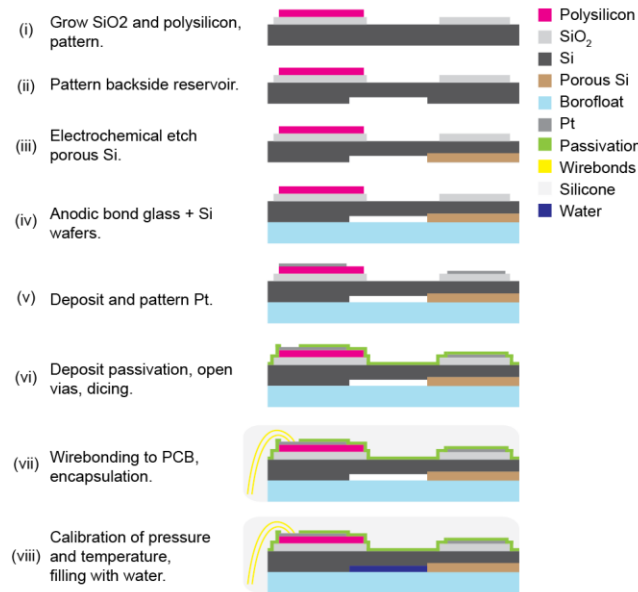


Figure 4.4: Sensor fabrication, simplified process flow.

Measurement in osmotic solutions

We prepared solutions of 1450 molecular weight polyethylene glycol (PEG1450) measured by weight to give a range of desired Ψ ¹⁸⁹. The solutions were mixed at room temperature until there was no trace of undissolved PEG1450, then measured with both a WP4C dewpoint hygrometer and a microtensiometer. For each measurement, a microtensiometer was submerged in the solution for ~20 minutes until ΔP_{tensio} plateaued and was recorded as Ψ . The sensor read this plateau value for an hour or more, but after long times ΔP_{tensio} began to drop as the PEG molecules infiltrated the porous Si membrane and contaminate the sensor water reservoir; therefore, the microtensiometer was removed from the solution as soon as a steady value of Ψ was recorded and placed in pure water to relax back to zero, then subsequently used to measure the next solution.

Measurement in soil

A water retention curve was measured in a core soil sample from Cornell grounds (Collamer silt loam) using a modified Wind/Schindler method¹⁹⁰ with only one tensiometer. Parallel measurements were taken on soil from the same area with a pressure plate extractor¹⁹¹. Soil samples were gathered from the Cornell grounds using metal cylinders 6 cm tall x 7.3 cm diameter. The metal cylinders were hammered into the soil and the cylinder bottom was carefully excavated to avoid disturbing the soil. The samples were covered on the top side with a mesh, weighed, and placed upside down in 5 cm deep water to fully hydrate over 2 days.

After the soil was fully hydrated from below, a 3 cm deep hole for microtensiometer placement was augered in the soil center. The hole was filled with water to prevent trapping of air bubbles, and a microtensiometer was pushed in all the way. Parafilm was used to cover the soil around the tensiometer and prevent water from seeping through or evaporating from this side of the cylinder. The cylinder and sensor system was then turned upside down and placed on top of a weight scale with a stand to begin taking data. Because of the parafilm, water only evaporated from the top side of the cylinder.

Over the course of a week, measured weight decreased and measured Ψ decreased until the sensor cavitated at -2 MPa, at which point the sensor was removed from the soil. Subsequently, the soil and ring system were weighted together, placed in a 110 °C oven overnight to remove all the water, then weighted again the next day. Finally, the soil was removed and the ring weighed by itself and

subtracted to get the dry soil mass. The water mass fraction (ϕ) is calculated as the weight of water divided by the weight of dry soil.

Measurement in plants

Measurements were taken in both apple and grape. We used potted apple trees 2.5 m tall with 3-5 cm diameter trunks and potted Cabernet Franc grapevines 1 m tall with 2-4 cm diameter trunks. The plants were kept in a temperature controlled greenhouse with summer conditions: 14 hours of light, temperatures above 18 °C, and watering 1 or 2 times a day at the discretion of the caretaker. A ceramic-based water potential sensor (MPS-6, Decagon Devices) was used to monitor soil Ψ and T in the apple pot. Solar radiation data was taken from the 'Ithaca Cornell' weather station from Cornell's Network for Environment and Weather Applications (NEWA)¹⁹² located ~2 km from the greenhouse.

Microtensiometers for plant measurements were encapsulated in a 9.5 mm OD cylinder of garrolite for easier embedding. A 1 cm-deep hole was drilled in the plant trunk 10 cm from the soil surface using a 9.5 mm drill bit that was flattened at the tip to produce a flat-bottomed hole in the stem. We note that in grape, the 1 cm hole was deep enough to hit the pith. The hole was wetted with water and the microtensiometer pushed in as far as it would go. The sensor was then sealed against the trunk with silicone caulking, thermally insulated with 3 layers of polyurethane foam rolled around the trunk and shielded from radiation with a cover of aluminum foil. The sensor was interrogated every 30 seconds by a datalogger (Campbell Scientific CR6) for 28 consecutive days, giving data on both Ψ and T . At the end of this period, the sensors were removed from the apple

and grape trunks and placed in pure water to measure their baseline pressure and check for drift. Both sensors drifted by -0.2 MPa.

Readings were taken about once an hour with a Scholander bomb (Soil Moisture Equipment Corp., 3005 PWSC model)¹⁰⁵ during one day to compare against the microtensiometer. For each measurement, leaves were bagged in aluminum foil-covered bags for at least 30 minutes, then the stem was cut with a razorblade and the bagged leaf immediately placed in the bomb for measurement.

Results and discussion

Sensor characteristics

In total, we designed and tested four rectangular diaphragm sizes in our search for a good compromise between sensitivity and equilibration time. Figure 4.5 shows the pressure calibration of a device with a 2 x 3.5mm diaphragm, and Figure 4.6 shows the equilibration of this device with a PEG1450 solution, from which we extract τ . Table 4.2 presents predictions and measurements of sensitivity, equilibration time and predicted break pressure for these 4 sizes. Sensors of the largest diaphragm size (3.5mm x 4mm) had low yields during fabrication because the diaphragm, being the most flexible, often bowed to the point that it bonded with the glass wafer during anodic bonding, and even devices that avoided this problem showed non-linear calibrations. For these reasons, we will focus our analysis on the other 3 diaphragm sizes.

As expected, larger diaphragms have higher sensitivities but also longer equilibration times. Measured sensitivity varied from 330 to 1400 $\mu\text{V/V/MPa}$ depending on the diaphragm size; taking

an applied voltage of 0.5 V ($V = iR = 200 \mu\text{A} \times 2500 \Omega = 0.5 \text{ V}$), our maximum sensitivity was $\sim 700 \mu\text{V}/\text{MPa}$, about a hundred times larger than the stated sensitivity for psychrometers of $\sim 7.9 \mu\text{V}/\text{MPa}$ ¹⁵⁷. Still, measured sensitivity was consistently $\sim 1/2$ of that predicted (eq. 4.14) for all diaphragms. Sensitivity could be lower because of process variations from those used in the references, which could lead to differences in the polysilicon doping level, distribution of dopants and grain structure. We note that even the sensitivity we predicted is at the lower end of possible sensitivities: K_I factors up to 40 ($2\times$ theoretical value used here, eq. 4.10) have been reported for ion-implanted polySi, and K_I for monocrystalline Si piezoresistors can be 100 ($5\times$ theoretical value used here)¹⁸⁰.

Measured τ was 1.4 to 6 times that predicted (eqs. 4.16, 4.17, 4.23, 4.24), with predictions successively becoming more accurate for larger diaphragms. Measurements of τ in the 2 mm \times 3.5 mm diaphragm showed large variation and we could not get an accurate value because of PEG infiltration of the porous Si membrane (discussed below).

Predicted values of breaking pressure (ΔP_{break}) are larger than the possible measurements for all diaphragm sizes. The 3 smallest diaphragm sizes cavitate before they reach the predicted breaking pressure, and the biggest diaphragm deflects enough to hit the bottom before reaching its predicted ΔP_{break} (-11 MPa).

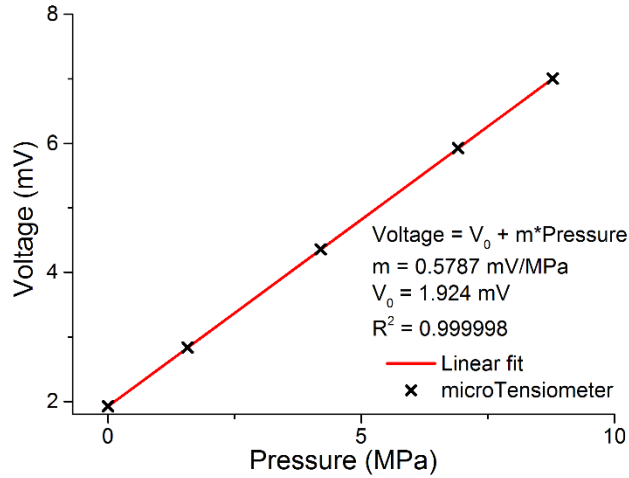


Figure 4.5: Calibration data for sensor in pressure chamber, powered by $i = 200 \mu\text{A}$. Red line shows linear fit for data, variables above show the offset (V_0) and slope (m) of linear fit.

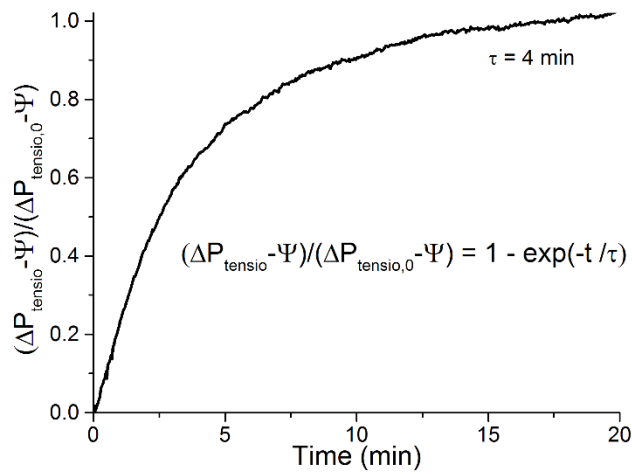


Figure 4.6: Microtensiometer equilibration time. Equilibration of sensor with a PEG1450 osmotic solution follows an exponential relaxation with characteristic time constant τ (eq. 4.16) that has some variability between sensors.

Diaphragm size (mm x mm)	Ψ sensitivity ($\mu\text{V}/\text{V}/\text{MPa}$)		Equilibration time, τ (s)		ΔP_{break} (MPa)
	Predicted	Measured	Predicted	Measured	
1×2	800	330	7	40	-84
1.5×3	1900	850	55	150	-37
2×3.5	3200	1400	180	250-600	-21
3.5×4	6100	1300-2300	3700	(150-900)	-11

Table 4.2: Comparison of diaphragm sensitivity, equilibration time, and breaking pressure. Measured sensitivity and equilibration times for the largest diaphragm size varied substantially due to intra device differences caused by excessive deflection and bonding of the diaphragm to the glass bottom.

The sensors tested could generally measure Ψ down to -8 MPa without cavitating, but some sensors remained stable to below -10 MPa. Sensors show large variability in this threshold (-5 MPa to -14 MPa), which could be explained by random defects in the fabrication and inhomogeneities in the porous Si membrane and bonding.

Figure 4.7 shows the calibration of a PRT. The PRT shows a temperature coefficient of ~ 3.3 $\text{m}\Omega/\Omega/^\circ\text{C}$, compared to that expected for pure bulk platinum of 3.9 $\text{m}\Omega/\Omega/^\circ\text{C}$. This discrepancy is commonly seen in thin film PRTs and is a function of the adhesion layer (Ti) and annealing temperature¹⁹³.

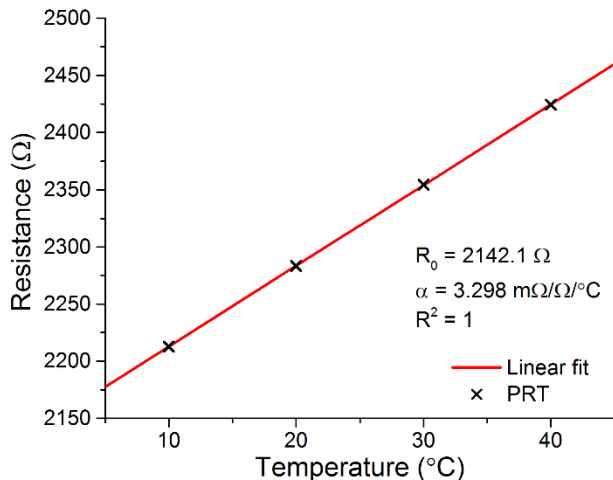


Figure 4.7: Calibration data for sensor platinum resistance thermometer (PRT). Red line shows linear fit for data, variables above show the offset (R_0) and slope (α) of the linear fit.

Osmotic solutions

Figure 4.8 presents the values of Ψ measured in PEG1450 with both the microtensiometer and the WP4C dewpoint hygrometer. Measurements performed with the microtensiometer along the whole range measured—from 0 MPa to -8 MPa—agree with measurements by the WP4C dewpoint hygrometer to within ± 0.3 MPa; the quoted uncertainty of the WP4C is ± 0.05 MPa. In all PEG1450 solutions, the microtensiometer measured a smaller magnitude Ψ than measured by the WP4C; agreement was best close to $\Psi = 0$, but worsened as the magnitude of Ψ increased.

Measurements in osmotic solutions, though accurate, show a number of problems. We chose to work with solutions of macromolecules (PEG1450) to prevent the osmolites from entering the nanopores in the porous Si membrane and contaminating the pure water in the sensor reservoir. Over short times (minutes), this condition holds, but over long times PEG1450 gets into the sensor, at which point ΔP_{tensio} returns toward zero. Larger PEG molecules, such as PEG8000, also infiltrate the porous membrane, though more slowly. Smaller molecules enter the reservoir faster: testing in

NaCl solutions shows the sensor measures an decreasing ΔP_{tensio} for ~20 seconds, then the reading comes back to zero in less than one minute. Therefore, measured values of Ψ depend on the solution measured and how quickly the measurement is taken. This infiltration of the sensor might partially explain the discrepancy between the WP4C and the sensor, as our measurements were always less negative than expected by WP4C measurements.

A related problem is that PEG solutions tend to foul the porous Si membrane and increase response time as the sensor is exposed to them. This fouling phenomena made it difficult to accurately measure τ , particularly for the slower diaphragms since even over the time it took to do one measurement the membrane became visibly slower. Thus for larger diaphragm sizes, the measured τ are likely longer than the τ for a clean membrane. Accurate measurements of τ could be achieved by measuring Ψ through the vapor phase, where there is no fouling, but this would necessitate a more complex setup (vacuum chamber), like the one used in our previous publication¹³⁰. Finally, in highly-concentrated electrolyte solutions, mobile ions infiltrate the packaging material and corrode the aluminum wirebonds, destroying the sensor over a period of hours.

If the problems stated above were solved, the microtensiometer could be used as an in-situ osmometer, and be calibrated with osmotic solutions—a process more easily done than pressure calibration. A potential solution to these problems is to add a vapor permeable liquid barrier membrane, such as expanded PTFE (ePTFE). This barrier would allow Ψ to equilibrate through vapor exchange, but keep solutes out, features that would allow measurement of small-solute solutions, prevent fouling of the porous membrane, and reduce ion-related corrosion of the sensor

electronics. We are in the process of testing the microtensiometer sensors with a covering of ePTFE.

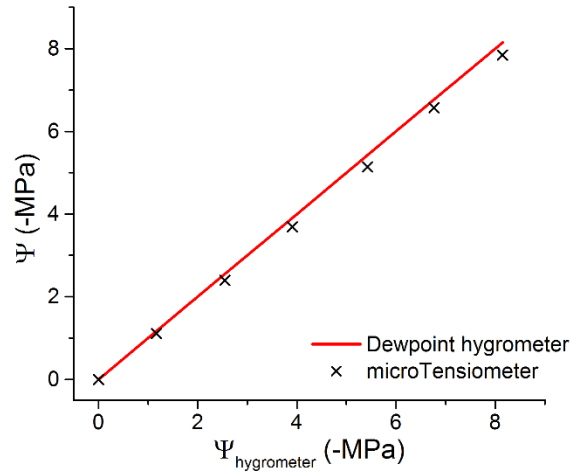


Figure 4.8: Measurements of PEG 1450 MW osmotic solutions with microtensiometer. Results are compared with dewpoint hygrometer measurements (red line with slope = 1).

Soils

Figure 4.9 shows the soil water retention curve, $\Psi(\theta)$, measured with the microtensiometer (black curve) and pressure plate (red squares). Our data follows the expected pattern for the soil type measured (silt loam)¹⁹⁴: at saturation ($\theta \approx 0.4$) Ψ has a steep slope; at lower mass fraction the slope becomes log-linear. We expect that the slope will become steep again at water potentials larger (more negative) than the range measured in this plot. To our knowledge, we are the first to measure a continuous water retention curve spanning the whole range of interest in agricultural soils ($-0.01 \text{ MPa} < \Psi < -2 \text{ MPa}$) with a single instrument.

Measured values of Ψ were generally lower than expected based on the pressure plate method, but the two measurements appear to converge as the soil dries. This discrepancy may be explained

by four factors. First, data at $\Psi > -0.1\text{MPa}$ is near the sensor accuracy. Second, as soil dries out, the connectivity of pores decreases and the soil sample becomes more heterogeneous. Therefore, a single tensiometer placed in the center of the soil column may not be representative of the whole sample. Third, errors in the experimental setup could have caused the curve in Figure 4.9 to be shifted to the right relative to the pressure plate measurements. Fourth, there could have been experimental errors in the pressure plate measurement, although reports generally propose that the pressure plate method tends to overestimate Ψ , not underestimate it. For instance, comparisons of the pressure plate method with psychrometry report that when -1.5 MPa of pressure were applied with the pressure plate, the average reading with the psychrometer was -1.1 MPa , and for -0.5 MPa pressure applied, the psychrometer read -0.48 MPa ¹⁹¹.

Given the nonlinear behavior of soil permeability, a full analysis of the drying process with the Wind/Schindler method is necessary to accurately determine the soil water retention curve. This method generally requires two or more tensiometer probes inserted at different depths in the soil. Using the additional data, in conjunction with a model of water potential gradients for the soil, functions for the soil hydraulic conductivity and water retention can be obtained^{195,196}.

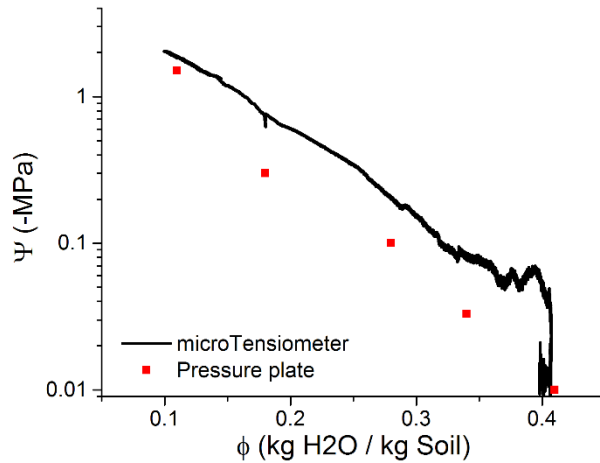


Figure 4.9: Measurement of soil water retention curve using Wind/Schindler evaporation method with microtensiometers (black line), and 5 measurements taken with a pressure plate extractor (red squares). x-axis shows the mass fraction of water in the soil (ϕ).

Plants

Figure 4.10 shows four days of consecutive data taken by the sensor in apple, including measurements of soil temperature and solar radiation. We note that there was a clear time-shifted correlation between the 4 measurements presented. In the morning, an increase in solar radiation was followed ~ 1 hour later by increasing soil temperature, ~ 1.5 hours later by increased stem temperature, and ~ 2 hours later by decreasing stem potential. In the afternoon, a decrease in solar radiation was followed by increasing stem potential, then soil temperature, and finally stem temperature. Baseline, pre-dawn values for Ψ during the night were about -0.3 MPa, but we note that baseline values were close to zero in the first 4 days following insertion (not shown), then steadily decreased to -0.3 MPa over 5 days and stayed near that value for the rest of the experiment. Sharp troughs in soil temperature occurred when the soil was watered, and each trough was followed by a dip in measured stem temperature and tension. There appears to be a relationship between temperature and measured Ψ : days with higher temperatures show lower Ψ .

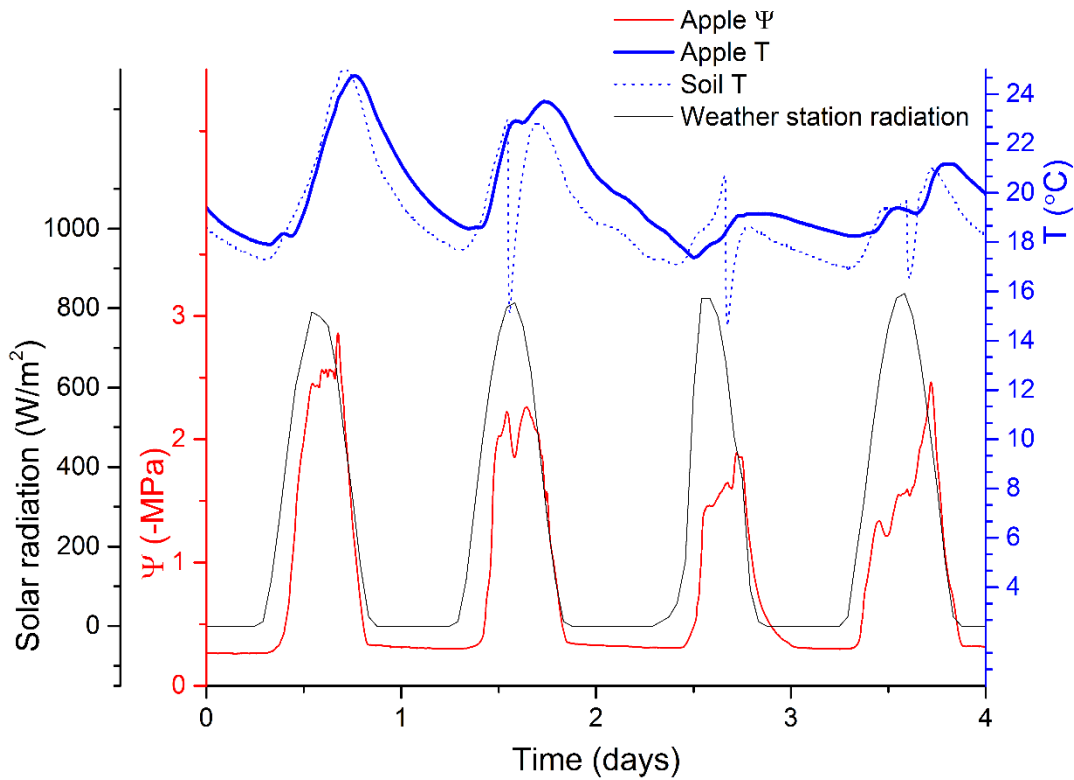


Figure 4.10: Measurement of apple stem water potential (Ψ , solid red line) and temperature (T , solid blue line) compared with solar radiation data (solid black line). Measurement of soil temperature also shown (dotted blue line), sharp troughs at 1.5, 2.5 and 3.5 days are when the apple soil was watered with cool tap water.

Figure 4.11 shows a day of measurements in both apple and grape, detailing a plot of solar radiation, temperature in the apple stem, grape stem and apple soil, and Ψ measurements in both apple and grape with the microtensiometer and pressure bomb. A few features stand out from the plot. First, the apple data taken by the sensor appears smoother, with clearly flat readings when there was no sunlight, and then a steadily raising Ψ reading over the solar noon that plateaus for 4 hours and then started descending as the sun goes down. The apple measurements agreed with the pressure bomb from midnight to about 11:00, when the pressure bomb readings plateaued but the microtensiometer readings continued to decrease and reach significantly lower values than the

bomb, then they agree again at about 19:00 hours once the sun was setting. Readings of Ψ thus follow the expected diurnal pattern, but were two times lower than bomb measurements during the hottest parts of the day.

The data on grape (blue curves) has a number of odd features. First, Ψ began decreasing around 2:00, before any sign of sunlight, and decreased to values substantially lower than measured by the pressure bomb. Second, the Ψ values measured throughout the day were clearly too low to be physiological—Cabernet franc grapes under deficit irrigation for months only show leaf $\Psi > -1.7\text{MPa}$ ¹⁹⁷—and clearly disagreed with the pressure bomb. We expect the grape leaves to look heavily wilted if Ψ drops below -2MPa , but the grapevine leaves looked unstressed. The lowest measured by the pressure bomb was -0.9MPa , whereas the microtensiometer measured values down to -4.2MPa .

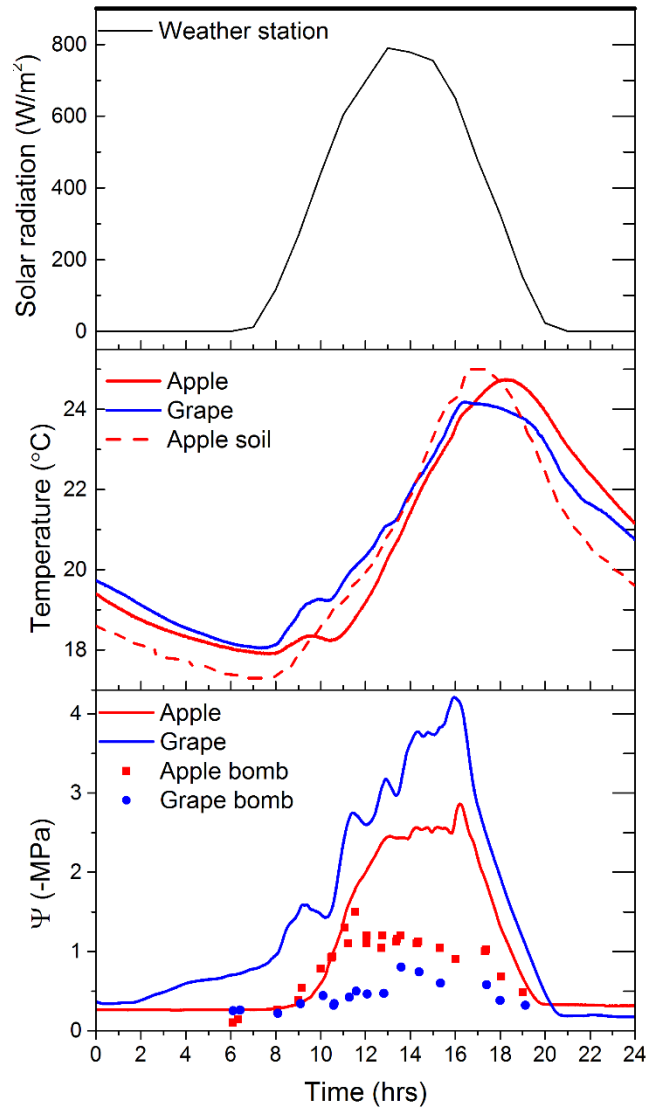


Figure 4.11: Measurements in apple and grape trunks over first day presented in Figure 7, compared with pressure bomb readings. (Top) Solar radiation measured an Ithaca weather station. (Middle) Temperature measured by microtensiometer in apple (solid red line) and grape (solid blue line), and temperature in the apple's soil pot measured by MPS-6 sensor (dashed red line). (Bottom) Measurements of Ψ in apple and grape by microtensiometer (red and blue solid lines) and pressure bomb (blue and red dots).

Discrepancies in plant measurements

Increasing pre-dawn tension in apple

The -0.3 MPa decrease in apple pre-dawn Ψ might have been caused by a localized drying of the tissue around the sensor or due to drift in the sensor. At least -0.2 MPa of this decrease can be explained by the measured sensor drift. The decrease could also have been a drop in actual pre-dawn Ψ , unlikely to be caused by drought since the apple was well-watered, but possibly due to a wounding response in the stem to the sensor.

Unexpectedly low mid-day Ψ : thermal effects

We hypothesize that the unexpectedly low Ψ readings in apple and grape, and the two hour lag between sunlight and apple Ψ have the same cause: differences in temperature between the sensor and the measured tissue. As discussed for psychrometry, a difference in temperature of 0.1 °C between the sensor and tissue would create an error of ~ 0.8 MPa in Ψ ¹⁵⁷. The sensor and stem could be at different temperatures due to a combination of transient and pseudo-steady state thermal effects.

Transient effects become important when changes in temperature occur faster than the typical thermal equilibration time for the system. To analyze transient effects, we model this system as an infinitely long solid cylinder made of the encapsulant material—ignoring axial heat transfer—that is surrounded by woody tissue. We assume uniform wood temperature, neglect contact resistance between the sensor and wood and assume the largest thermal resistance in the system is that of the thermally insulating packaging material (thermal conductance = 0.25 W/m.K). We take the cylinder of radius $r = 5$ mm, initially at a uniform temperature T_i , and apply a temperature T_∞ at

the cylinder outer wall. The temperature at the center (T_0) will equilibrate towards T_∞ over time, approximated by¹⁹⁸:

$$\theta = \frac{T_0 - T_\infty}{T_i - T_\infty} \approx A_1 \exp\left(\frac{-\lambda_1^2 \alpha t}{r^2}\right) \quad 4.30$$

where θ is how much the system has equilibrated, $\alpha = 1.18 \times 10^{-7} \text{ m}^2/\text{s}$ is the encapsulant thermal diffusivity and $A_1 = 1.6021$ and $\lambda_1 = 2.4048$ are coefficients for the transient one-dimensional heat conduction approximation. Setting $\theta = 0.01$ (T_0 equilibrated to within 1%) we solve for t and get $t \approx 3$ minutes. Therefore, this model predicts that for a step change in temperature of 1 °C, the sensor will come to thermal equilibrium ($|T_0 - T_\infty| < 0.01 \text{ °C}$) within 3 minutes. This small time to equilibrium appears to indicate that transient thermal effects between the sensor and stem are generally negligible in our system, therefore pseudo-steady state effects might be more important.

If the thermal contact between the sensor and tissue is poor, the sensor temperature will be set by a combination of the temperature of the insulation and the temperature of the tissue. This effect will be particularly strong during times when the tree is quickly gaining or losing large amounts of heat due to sunlight or radiative cooling. We analyze this effect as a pseudo-steady state heat transfer problem, where the temperature profile in the system is nearly constant and the temperature at the boundaries changes slowly. We model the insulation-sensor-stem system as a series of temperatures—outside temperature (T_1), sensor temperature (T_2), and stem temperature (T_3)—and resistances—insulation resistance (R_{12} , [°C/W]) and sensor-stem contact resistance (R_{23}). Assuming steady state heat flow, the temperatures and resistances are related as follows:

$$\frac{T_1 - T_3}{R_{12} + R_{23}} = \frac{T_2 - T_3}{R_{23}} \quad 4.31$$

For errors to be < 0.1 MPa, we require that $|T_2 - T_3| < 0.01$ °C. Applying this condition, and rearranging eq. 4.31 we get:

$$|T_2 - T_3| = |T_1 - T_3| \left(\frac{R_{23}}{R_{12} + R_{23}} \right) < 0.01 \text{ °C} . \quad 4.32$$

This equation shows that to minimize steady state heat gradients we can decrease the temperature difference between the outside and stem ($T_1 - T_3$), increase the insulation resistance (R_{23}), or decrease the sensor-stem contact resistance (R_{23}). Assuming a worst-case $T_1 - T_3 = 5$ °C, we require that $R_{23} < 0.002R_{13}$. In future experiments, we plan to measure the differences in temperature between the outside, the sensor and the stem, and develop models for the insulation and sensor-stem contact resistances.

If the sensor has poor thermal contact with the stem, then the sensor temperature will be influenced by the temperature of the insulation and outside ambient. It can be expected that, if heat transfer between sensor and stem is poor, the sensor temperature will lead the stem temperature. In this case, the sensor is hotter than the stem when the outside temperature is increasing (8:00 to 17:00 in Figure 4.11), and the sensor is colder than the stem when the outside temperature is decreasing (17:00 to 8:00). In the morning, a colder sensor would explain why Ψ readings only begin decreasing 2 hours after sunrise. In the afternoon, a hotter sensor would explain why Ψ readings continue to decrease until 17:00 whereas pressure bomb readings plateau at 14:00.

Figure 4.12 contains an analysis that sheds light on the ‘temperature difference’ hypothesis. Since we do not have an independent temperature measurement of the tissue surrounding the sensor, we use the next best thing: data on temperature from the sensor itself at $t = -30$ minutes as a surrogate

for stem temperature at $t = 0$. This figure shows the microtensiometer-measured Ψ and T in apple, plus a plot of the difference in sensor temperature between $t = 0$ and $t = t - 30$ min. Comparing this temperature difference with the shape of the Ψ curve at various points suggests that the lag is causing at least part of the discrepancy between the microtensiometer and the bomb: when the sensor is hotter than the stem, thus increasing in temperature, the measured Ψ is lower than expected and vice versa. We are designing a smaller sensor packaging that can be fully embedded in the trunk to decrease R_{23} / R_{12} and minimize this temperature lag.

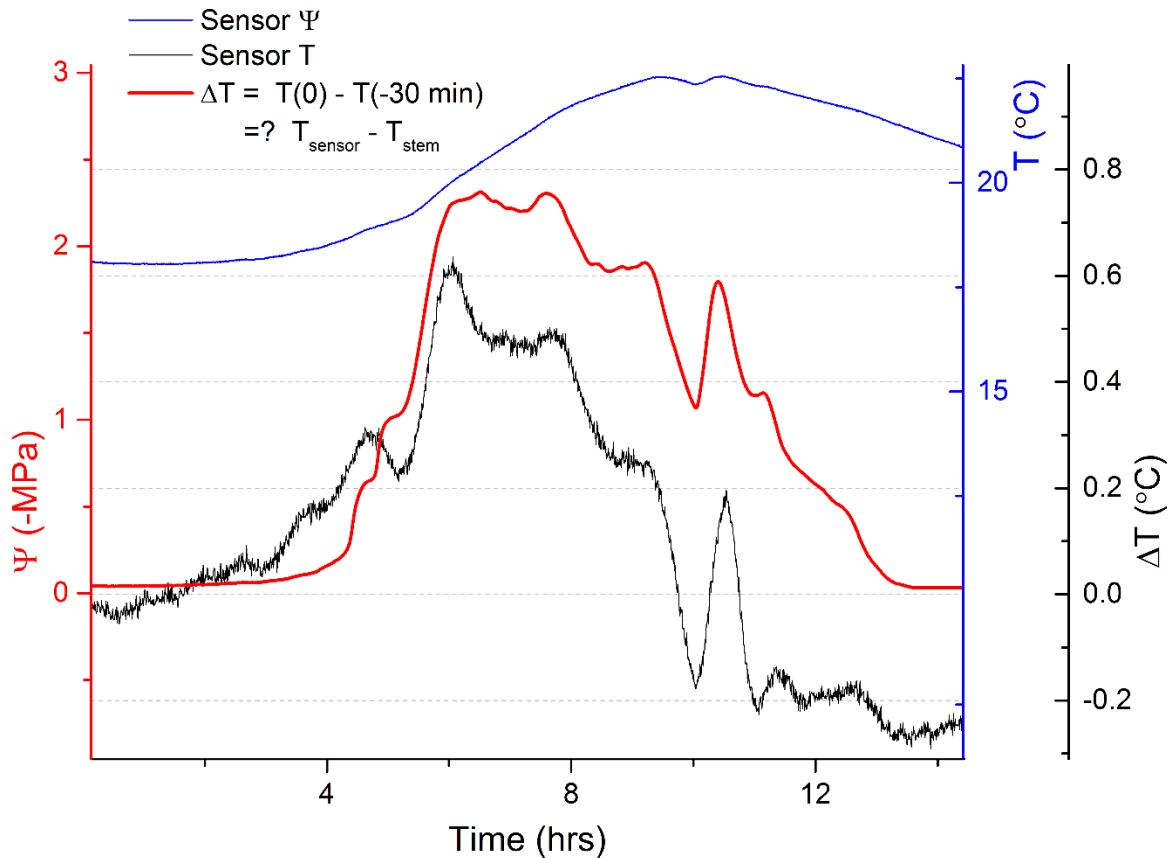


Figure 4.12: Effect of stem-sensor temperature lag on water potential measurements. Figure shows water potential (Ψ , red line) and temperature (T , blue line) measured by a microtensiometer in apple, and temperature difference between sensor at time zero and 30 minutes before (ΔT , black line). Temperature 30 minutes before is taken as a surrogate for stem temperature.

Conclusions

We have developed a water potential probe that enables measurements of Ψ in a variety of contexts. The probe is smaller than a pen, has accuracy comparable to laboratory instruments (0.3 MPa compared with the WP4C), takes continuous measurements, equilibrates in 20 minutes, is robust and rugged for field measurements, and has a range 80x of conventional tensiometers (-8 MPa). The sensor was tested in osmotic solutions, soil and living plants. There are still improvements to be made with regards to membrane fouling by osmolites, the measurements of

small-molecule osmotic solutions, and temperature equilibration. More testing is needed to determine the sensor viability for long-term, multi-month measurements in soil and plants, in particular sensor drift and accuracy.

We believe the microtensiometer opens up a plethora of research opportunities in the various contexts. In osmotic solutions, it could be developed into an accurate and easy to use in-situ osmometry probe. In concrete, it would enable measurement of curing during the first few hours. In soil, it allows in situ point-like measurements, monitoring water drainage, improved irrigation scheduling, and measurement of moisture retention curves with a single instrument for the whole range of interest. In plants, it could provide robust realtime monitoring of stem water potential, and mapping of in-vivo potential from roots to leaves.

Acknowledgements

The authors wish to thank Decagon for the Grant A. Harris Research Instrumentation Fellowship that provided the WP4C hygrometer, Glenn Swann for machining help in building the sensors and the soil measurement setup, Lailiang Cheng for donating apple trees for testing, and Robert R. Schindelbeck for the soil samples and pressure plate measurements. This work is supported by the NSF Graduate Research Fellowship under Grant DGE-1144153 (MS and WLB) and Alfred P. Sloan scholarship (MS and WLB), the National Science Foundation (CBET-0747993 and CHE-0924463), the Air Force Office of Scientific Research (FA9550-09-1-0188), the National Institute of Food and Agriculture, U.S. Department of Agriculture (under agreement no. 2010-51181-21599). It was performed in part at the Cornell NanoScale Facility, a member of the National Nanotechnology Coordinated Infrastructure (NNCI), which is supported by NSF (Grant ECCS-

15420819); and made use of the Cornell Center for Materials Research Shared Facilities which are supported through the NSF MRSEC program (DMR-1120296), and the Nanobiotechnology Center shared research facilities at Cornell.

Supplementary

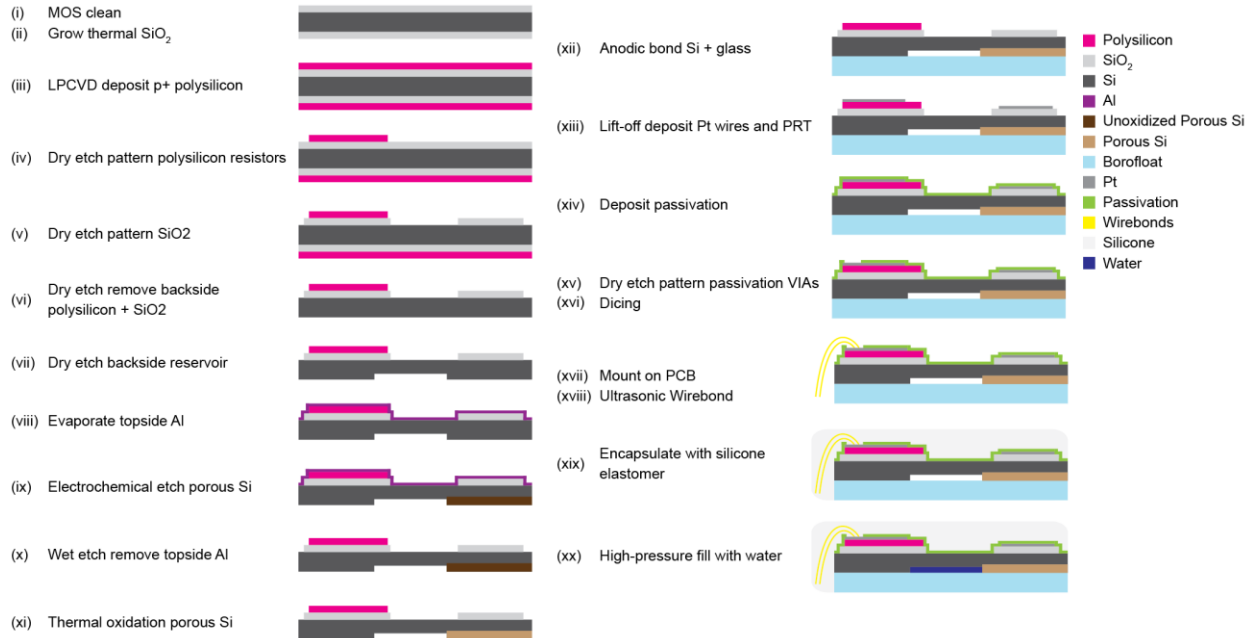


Figure 4.13: Detailed sensor fabrication process flow.

CHAPTER 5

CONCLUSION

We set out to study and develop tools for better understanding the properties of water and its behavior in porous materials of relevance in the biosphere. The main accomplishments were:

- (1) We developed a model of electrokinetic effects in plant xylem, and found that these effects may decrease hydraulic conductance up to 18% with the addition of ions to the perfusate. When compared to experiments, this decrease could explain conductance decreases seen under physiologically relevant conditions, but is too small to explain larger decreases seen in one experiment at low ionic concentrations. Experiments were proposed to determine how much of the ‘ionic effect’ is due to electrokinetic effects.
- (2) We developed a MEMS-based microlaboratory that uses the metastable vapor liquid equilibrium principle to measure the cavitation pressure and equation of state of liquids under tension, particularly water. We were able to measure the equation of state of water down to -15 MPa, and this platform could be extended to measure the equation of state of other liquids under tension.
- (3) We developed a tensiometry-based water potential probe that can reliably measure pressures down to -8 MPa, at least 80× the range of conventional tensiometers. The device could work as a generalized in situ probe for measuring water potential in field conditions. It was tested successfully in osmotic solutions and with partial success in soil and tree stems.

Limitations of the research

Measurements of the equation of state of water were limited in accuracy and range of temperatures, not only by the MEMS sensor, but also by the vacuum chamber system used to control the activity surrounding the sensor. This system is limited by the accuracy of the pressure gauge and computer controlled valve. It is also limited in the range of temperatures it can measure due to the capability of the vacuum gauge to withstand water vapor pressures above 25 °C, or the accumulation of ice below 0 °C. Finally, there are indications that the measured cavitation pressures are a function of not only the measured liquid, but also the microtensiometer sensor—its pore structure and presence of contaminants within it.

The water potential probe was developed under constraints of time, economic resources, and technical expertise. There are thus many areas in which it could be improved further. Unfortunately, packaging and MEMS sensor design was rudimentary because of limited expertise, and the complexity and cost involved in developing a MEMS package. A commercial effort might be needed to produce long-lasting easy to use sensors. Our longest experiment lasted 28 days, and the sensors showed a -0.2 MPa drift. The sensor longevity and drift need to be analyzed in longer studies, and it may be necessary to modify the sensor microfabrication and develop new encapsulation strategies to improve the sensor longevity. The sensor could be used in solutions containing electrolytes, but this avenue is closed by corrosion of the sensor electronics. This problem might also be solved by changes in packaging, such as adding an ePTFE membrane. We do not understand why sensors in the same wafer have different cavitation pressures, or how to improve our fabrication process to have a larger working range before cavitation without significantly increasing the response time.

There was insufficient time to study the sensor working in plants and why there was a discrepancy between the sensor and pressure bomb. It may take season-long detailed trials to test the hypothesis that discrepancies were caused by thermal effects, though it may be possible to correct for these effects. Another unanswered question is whether the plant wounding response will limit the sensor functioning over the course of weeks to months. For instance, callus formed might block the equilibration between sensor and xylem. Similarly, only one week-long soil measurement was performed, and compared to only one set of pressure plate measurements. The results are encouraging, but more careful studies are needed.

Implications

The tensiometer-based microlaboratory is the base of a system that could be further developed to perform a variety of measurements in pure liquids and mixtures under tension. The system could be modified to measure fluid viscosity, heat capacity, and speed of sound, in addition to studies on fluid evaporation and condensation. By changing the membrane properties, the system can be used to study how membrane properties such as contact angle, pore size distribution, and thickness affect the cavitation limit. It might even be modified to study biological molecules under tension, similar to previous studies using the Berthelot tube method^{199,200}, and possibly even microorganisms.

The water potential probe developed here will enable more widespread measurements of soil water potential, particularly in soils too dry for conventional tensiometers. Because of its small size, it serves as an in situ probe of water potential that has accuracy comparable to benchtop

instrumentation. It might enable study of the role of water potential in processes such as soil crusting²⁰¹, and detailed experimental study of driving forces and hysteresis in soil.

Our sensor gives researchers access to direct measurements of water potential in the xylem, in real time. As the microtensiometer is manufactured in larger quantities and better insertion methods are developed, it will become possible to ask more detailed questions about the movement of water in xylem and porous materials in general. Continuous data of water potential may lead to novel insights regarding water regulation.

The microtensiometer, if developed further, could be an easy to use, affordable tool with widespread use in agriculture. The sensor could be part of an automated irrigation system, but—having direct access to the plant water status— would allow very precise control of plant water status to either improve quality of produce, as in wine grapes, or reduce water use through deficit irrigation.

APPENDIX

Microtensiometer mask images

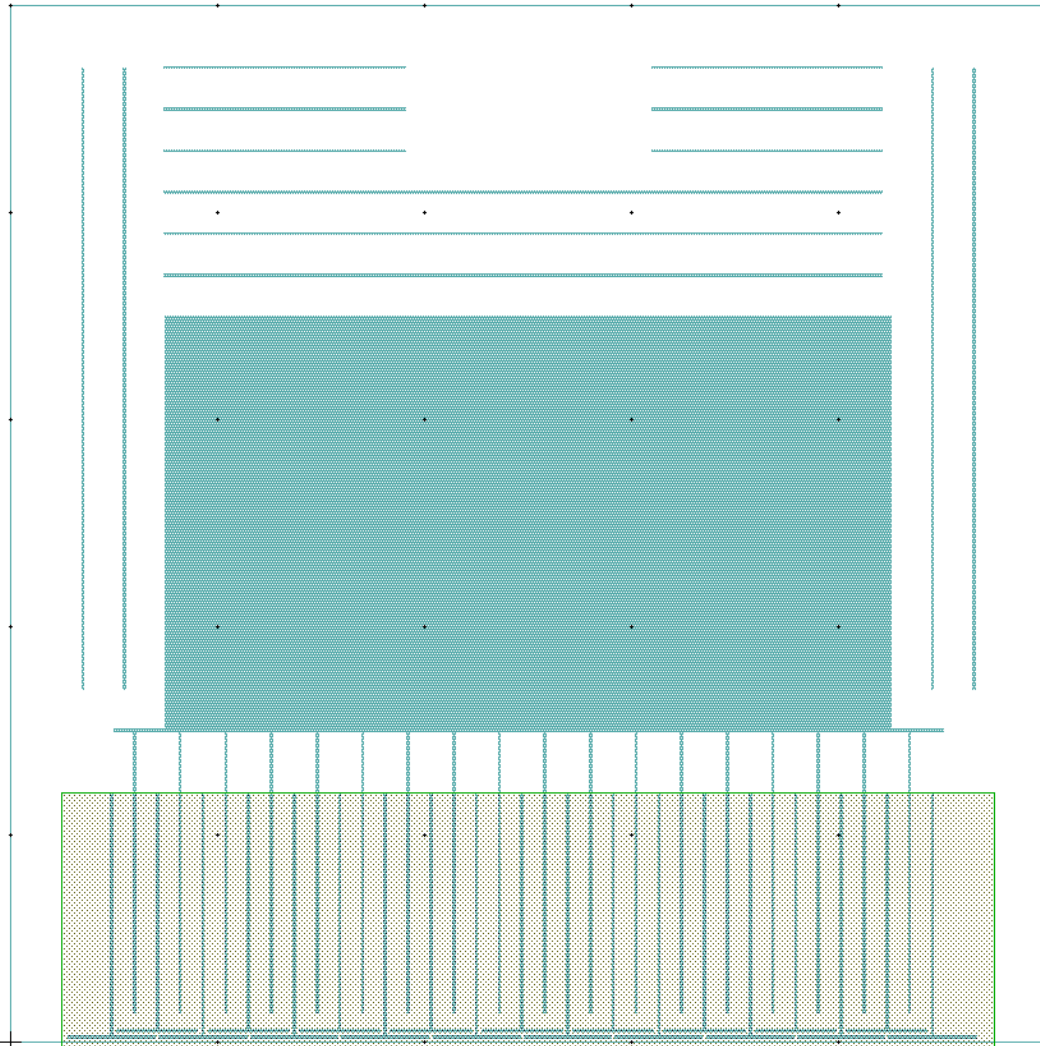


Figure 6.1: Water cavity with xylem structure (dark green). Patterned porous Si layer (transparent grey).

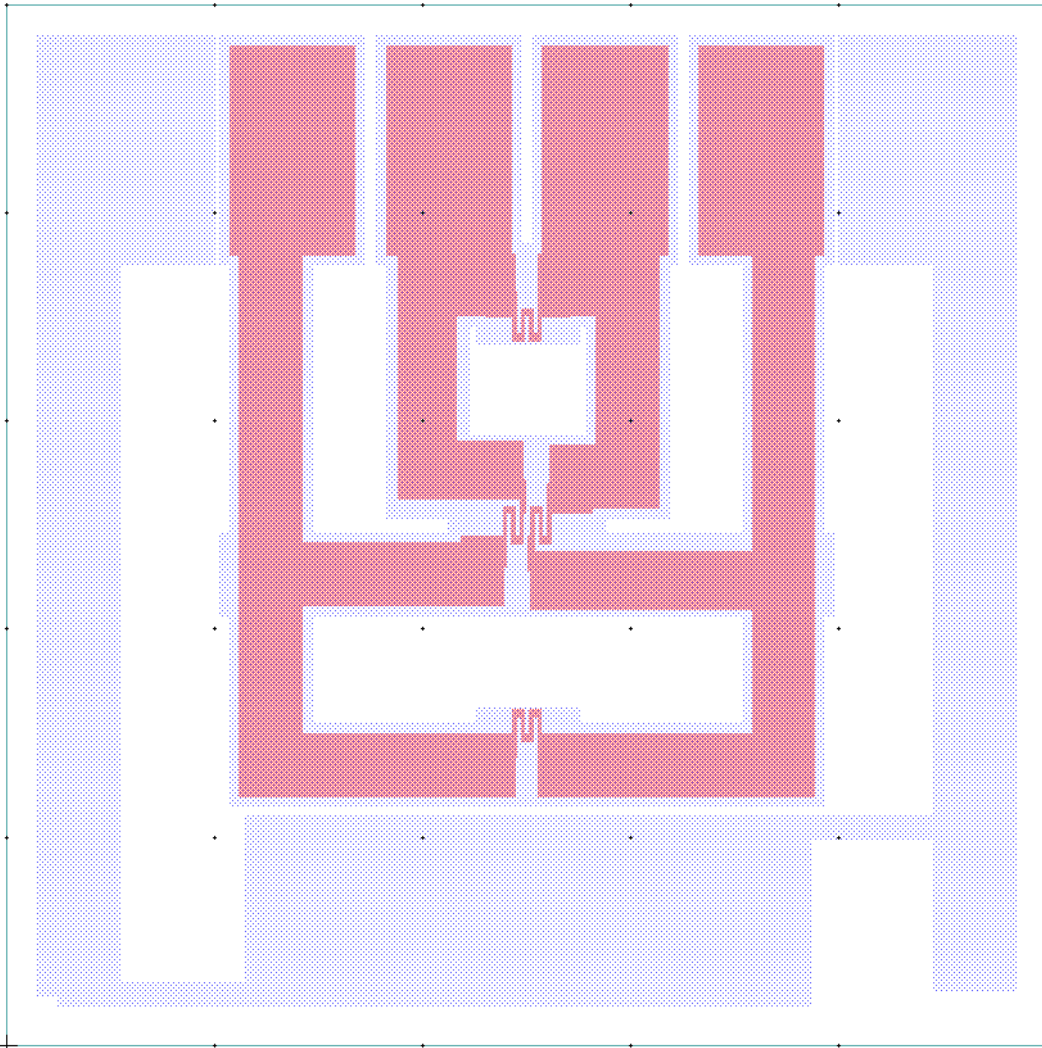


Figure 6.2: SiO₂ insulation (transparent blue) and polySi (red).

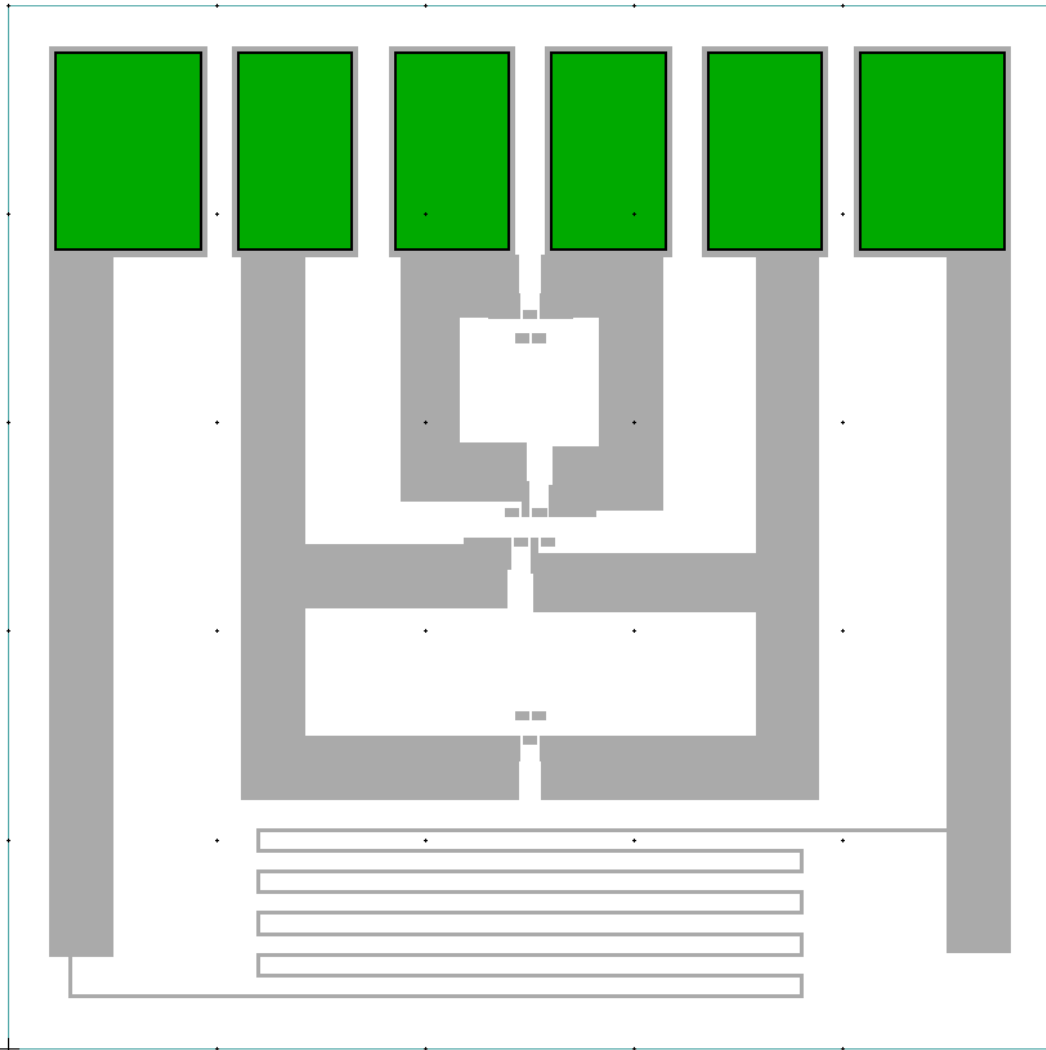


Figure 6.3: Platinum wires (solid grey) and VIA openings (green).

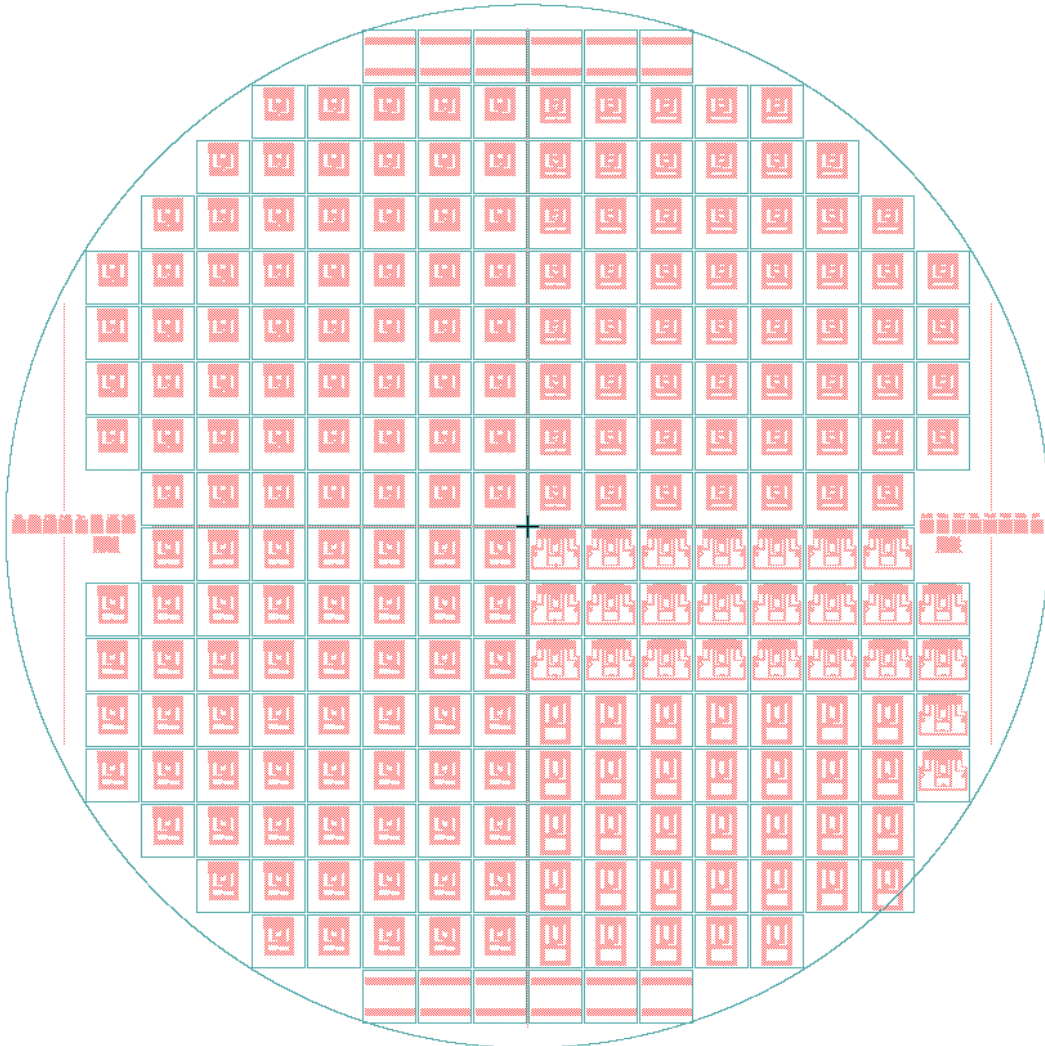


Figure 6.4: Full wafer mask with all devices. Only polySi layer shown for simplicity.

Microtensiometer process flow

General notes

- Process multiple wafers simultaneously to cover against unexpected losses.
- Keep processes clean for best electronics.
- Keep gloves clean. Avoid touching face & depositing oils on the wafers.
- Machines for photolithography, etching, deposition, etc. change over time. Test & verify.
- Check wafer features after every step to catch problems early.
- Reserve machines before and while using or you will get pushed out by the next user.
- Photoresist seems to corrode Aluminum if left on it for days. Avoid.
- The oxford 81/82 Si etch rates are ~400nm/min for SF6/O2 Si etch. Different from stated.
- Take copious, detailed notes on each process run. Will need them if something goes wrong (or right!).
- Default photolith process. Spin clean Acetone/Acetone+IPA/IPA, spin P20, spin resist: S1827, 3000 RPM, 5000 RPM/s, 30s. Soft bake 90s @ 115 °C on hot plate. Expose with desired mask in Or MA6: 8s exposure, soft contact, 10 μm alignment gap, Cont WEC type. Center stage: 10mm x-axis, 10mm y-axis, 0° theta. Or ABM: 16s exposure, vacuum contact, 100 μm alignment gap. Develop in Hamatech w/ 726 MIF, 60s, DP.
- To develop by hand: dip 2 minutes in 726MIF, rinse.
- Default resist strip: Aura 1000, recipe #8.
- Clean masks in Hamatech Hot Piranha if dirty.

Wafers

Silicon: 100mm DSP, 300-350 μm thick, P-type, Boron-doped, <111>, 1-10 Ω-cm resistivity

Glass: 100mm borofloat, 500 μm thick

Process steps

1. Deposit SiO₂ & p⁺-doped polysilicon on silicon wafers + 2x baffle wafers.
 - Measure wafer resistivity.
 - MOS clean Si + 2x baffle wafers
 - Grow SiO₂ for insulation in B2 thermal oxide furnace (800 nm). Wet Ox/No HCl, 1000 °C 'P', 200 min (check rates).
 - Deposit p⁺-doped polysilicon for resistors in LPCVD furnace C4 (800 nm, 6e19/cm³ carriers). Use baffle wafers. Gases are 70% of 1.5% B₂H₆ gas (270 sccm) & 30% SiH₄ (90 sccm) [B₂H₆:SiH₄ ~ 0.045], 620 °C 'P', 130 min (check rates). Rate 6nm/min. [In-situ doping is uneven, a better option is to deposit plain polySi, ion-implant Boron, and anneal.]
 - Anneal polySi to increase linearity in furnace B1. Inert gas (Ar), 900 °C 'P', 30 min.
 - Measure polySi/SiO₂ thickness in filmmetrics. Expected: 900nm/800nm
 - Measure polySi film resistivity in CDE 4-pt probe. Wafer map. Expected: $r = 0.01 \Omega\text{-cm}$. $r = \Omega/\text{sq} * \text{film thickness (0.000070 cm)}$.
2. Pattern resistors
 - Oxidize polySi slightly to make hydrophilic & improve photoresist adhesion. Aura resist descum #F + test drop.
 - Photolith frontside w/ RES mask.
 - Check features in microscope.
 - O₂ clean Oxford 81/82 for 5 min. Dry Etch polySi (SF₆/O₂) for 4 min. Check rates + etch 120%.
 - Check wafer oxide color. Expected: blue/purple/green. Look at backside to compare with un-etched polySi.

- Strip resist Aura 1000, recipe #8.
 - Check for resist residue.
 - Use pin probes to measure/note R across 4x resistors for reference.
3. Pattern oxide
- Photolith frontside w/ Oxide mask.
 - Check features in microscope.
 - O2 clean Oxford 82 for 5 min. Dry etch SiO2 (CHF3/O2) 20 min (rate ~40nm/min). Check rates, etch 120% layer thickness. Don't wet etch (undercut), nor use CHF3/Ar (leaves polymer).
 - Finish-off pattern with dip in BOE6:1 until surface hydrophobic. ~3mins, no much longer to prevent undercut. Dry etch does not remove all oxide. Don't use last 10% of BOE bottle, leaves residue.
 - Check wafer color. Expected: metallic grey.
 - Strip resist Aura 1000, recipe #8.
 - Check for resist residue. Check resistor/oxide condition.
 - Measure SiO2 + polySi thickness in profilometer. Expected: .7 μm + .8 μm .
4. Remove backside polySi/SiO2
- Protect frontside by spinning/baking/developing resist. Spin Acetone+IPA to clean backside, then spin rinse.
 - O2 clean Oxford 81/82 for 5 min. Dry etch polySi (SF6/O2) 4 min. Dry etch SiO2 (CHF3/O2) 20 min. Check rates, etch 120% layer thickness.
 - Finish off with BOE 6:1 dip until hydrophobic, ~3mins.
 - Check all polySi/SiO2 is gone. Expected color: shiny grey. If not keep etching.
5. Pattern backside cavity
- Photolith backside w/ CAV mask. Backside is still protected with photoresist.
 - Check features in microscope.
 - Resist descum in Aura, recipe #F.
 - Measure photoresist depth in profilometer P10. Expected 3,000nm.
 - O2 clean Oxford 81/82 for 5 min. Dry etch Si (SF6/O2) to 3 μm ~500nm/min. Check rates + etch 25%, measure in P10, etch rest.
 - Check cavity depth in profilometer. Expected: 3 μm resist + 3 μm = 6 μm . If not keep etching.
 - Strip resist Aura 1000, recipe #8.
 - Check for resist residue.
6. Cover frontside w/ Al for porous Si etch
- Clean wafers in Nanostrip to prepare for Al deposition and porous Si formation.
 - Dip wafers in 6:1 BOE ~5 seconds until surface around oxide is hydrophobic (don't leave more than 1-2mins!). Rinse 2x in water to remove BOE particulate.
 - CHA conformal deposit 200nm Al. Immediately. Layers #1 (1 $\text{k}\text{\AA}$). 3 $\text{\AA}/\text{s}$ rate.
 - Warm up RTA 15 mins. MOS SIDE ONLY. Anneal 2 min @ 400 $^{\circ}\text{C}$ with Ar/H gas in RTA (recipe: ms400). Short anneal only.
7. Pattern porous Si (OPTIONAL).
- Photolith w/ POSI mask: Acetone/IPA rinse, P20 prime, AZ P4903 photoresist, spin w/ recipe AZP4903 (200 rpm 5000 rpm/s 8s + 4000rpm 5000rpm/s 30s; gives 6 μm), bake @ 115C 3min, wait 30+ mins (<1 hr, resist goes bad after that), expose 15s in MA6, develop with AZ 421K 4 mins ONE SIDE ONLY (attacks aluminum), rinse/dry, bake 115C 1min.

- Check in microscope, ensure all photoresist removed.
 - Descum in Aura.
 - Etch porous silicon as usual, except (1) use less current according to open area ($20 \text{ mA/cm}^2 = 240 \text{ mA}$ for poSi mask w/ area of 12 cm^2), (2) mix ethanol and HF solution together before pouring on top of wafer in etch bath [otherwise the photoresist will be impossible to remove].
 - Wash w/ acetone then IPA to remove photoresist.
8. Make porous Si, remove aluminum, oxidize pores
- Sonicate in Acetone/IPA, then plasma clean in Olin (not patterned porous Si).
 - Etch porous Si 5 mins, 20 mA/cm^2 (0.9 A for 3" bath), 49%HF/Ethanol 150/150 mL. Use non-denatured Ethanol. Mix solution. Keep top electrode centered and 1" away from wafer for uniform field. Polish bottom electrode to prevent scratching of metal & improve contact. Don't rotate wafer. Short etch for better stability (?).
 - IPA-rinse wafers and dry thoroughly. Keep in dry-box so HF in pores can evaporate.
 - Remove topside Aluminum with developer AZ 300 MIF (312 MIF is even more concentrated). [Use Glenn-jig]. Place wafer on wipe, aluminum side up, and pipette a 2-3mm thick film of 300MIF on top. Move with swab. Takes ~10mins to remove 100nm Al. Careful with solution, it can damage the pores if it spills under the wafer by wicking the napkin. Spin rinse.
 - Check features under microscope, look for junk on wafer.
 - Clean Si: Acetone dip 1 min, IPA dip 1 min, spin rinse.
 - Warm up RTA 15min. MOS SIDE ONLY. Test porous piece, then anneal PoSi in RTA @ $700 \text{ }^\circ\text{C}$ for 30s in O₂, ramp 10C/s. Remember to press O₂ on button every few minutes.
 - Check resistors & SiO₂ in microscope. Expected: look clean.
9. Anodically bond porous side with borofloat glass wafer.
- Clean glass in nanostrip.
 - Plasma clean Glass + Si w/ descum in Anatech @ 150W 4 mins.
 - Anodic bond at CNF: Use 'ms2343-anisothermal' recipe [add details here].
 - Check bonding for cracks.
10. Deposit & pattern metal with LOR
- Pirahna clean wire side to prepare for lift-off.
 - Spin LOR 5A in class2 spinner, SU8 room: 3,000 RPM, 10,000 RPM/s, 45s (recipe 3000-45S). Bake 180C 5min.
 - Photolith w/ MET mask. Expose 1.5x dose. No acetone, no P20; they damage the LOR.
 - Develop for 2x as usual, 120s DP, maybe more. Need extra time for LOR to dissolve.
 - Check features in microscope. Ensure all photoresist + LOR gone and can see oxide color below.
 - Descum in Aura.
 - Dip wafers in 6:1 BOE (will not be hydrophobic). Rinse 2x in water to remove BOE particulate. BOE helps clean glass wafers.
 - Odd/even hour deposit 15/200/15nm Liftoff Ti/Pt/Ti. Immediately. $0.6\text{-}1 \text{ \AA/s}$ rate for Pt (14-15% PWR), ramp slowly to avoid spitting.. $\$0.08/\text{\AA}$ for Pt. Wait 10-15min for machine to cool down before venting to decrease film stress
 - Lift-off resist in 1165 overnight, constant stirring. Or place in sonicator w/ 1165 @ 60C for ~30mins (check). IPA rinse and swab clean each wafer to remove particulate. Spin rinse.
 - Check for resist residue.

- IV probe or normal probes. Measure resistances. Expected: 3000 Ω . Check linearity. Measure contact resistance. Expected: < 1 Ω .
- IV probe measure bridge resistance (3000 Ω), PRT resistance (3000 Ω), Si contact resistance (~10 Ω), polySi contact resistance (~10 Ω), polySi contact linearity.

11. Deposit & pattern passivation layer

- Clean wire side to prepare for passivation w/ Acetone, then IPA 1min (not piranha, removes Ti).
- Oxford PECVD: run dummy wafer to cool machine to 200 °C. Deposit 400nm oxide (1.5 min), 300nm nitride (5 min) [**HIGH RATE, CHANGE RECIPE, pulse time 12s**], 200nm oxynitride (2 min) [**N2O flow = 50**], 100nm oxide (30s) @ 200 °C. Rates: 250nm/min SiO₂, 40nm/min SiN_x, 100nm/min SiON. Check recipe temperature in all steps. Clean machine for deposition time after every 2 wafers +10 min.
- Photolith w/ VIA mask.
- Check features in the microscope.
- O₂ clean Oxford 81 for 5 min. O₂ descum 1 min. Etch SiO₂ + SiON + SiN_x + SiO₂ with CHF₃/O₂. Check rates + etch 120%, total ~20 min. Finish dry etch with 1+ min BOE 30:1 etch to ensure complete removal of oxide and Ti on top of Pt (and Cr etch if there is chrome).
- Measure resistances with multimeter & compare with previously measured values. Expected: same.
- Strip resist with Acetone, IPA, Hot Piranha.
- Check wafer in microscope for resist residue.

12. Ensure everything is alright with wafer

- Microscope check wafer is clean, features are aligned, bonding is good.
- Probe resistances. Expected same value.
- Test wirebond to wafer to ensure vias are open and pads are clean.

13. Dice wafer

- Place wafer in white tape with silicon side facing the tape to protect electronics, see cavities. Dice settings: all purpose blade, circular wafer, 100mm diameter, 800 μ m thick, depth = 35, cut pitch is 5.3 mm & 5.3 mm. (BLUE TAPE HEATED UP TO 50C MAY WORK BETTER0)
- Dice at bottom (or top) line to measure where the blade edge hits, goal is for blade edge to hit the middle line in the center. Dice 150-microns below this middle line, and shift the dicing position accordingly. If the blade hits 20 microns below the middle line, shift the dicing 20 microns 'up'.
- Cut out wafer. Dry in napkin. UV 3 min to weaken tape (necessary).

14. Mount on PCB, wirebond & solder connections

- Adhere chip to PCB with 5-min epoxy. (Instant adhesive is removed by acetone)
- Sonicate in Acetone/IPA 10 mins, flush in IPA, airgun dry.
- Plasma clean 5 min.
- Wirebond in Westbond ultrasonically: (1) Gold on PCB, Time = 4, Power = 3; (2) Platinum pads on sensor, Time = 3, Power = 4.5
- Solder solid-core wire (stranded causes vacuum problems when curing encapsulation).

15. Seal front edge, encapsulate, vacuum out bubbles.

- Sonicate in Acetone/IPA, flush in IPA, airgun dry.
- Seal front pores with tape (or not, if using viscous epoxy)
- Plasma clean 5 min.

- Place thin film of Marine/Black-PDMS on PCB top (thinnest possible to decrease volume that holds water). Wait ~15mins for marine to 'thicken' before use.
- Place in vacuum oven, pull out all air bubbles from package (slowly to prevent covering the front), then cure. Marine in ambient overnight, Black-PDMS at 70C 150min.

Other processes:

1. Deposit SiO₂ membrane
 - Deposit 1µm SiO₂ in Oxford PECVD @ 200 °C, ~4 min @ 250nm/min. Lower temperature makes layer more porous.
2. Pattern Pt with Ion Mill
 - Piranha clean wire side to prepare for metal deposition
 - Dip wafers in 6:1 BOE (until hydrophobic). Rinse 2x in water to remove BOE particulate. BOE helps clean glass wafers.
 - CHA deposit 15/100/15nm Conformal Ti/Pt/Ti. Immediately. Layers # (0.15 kÅ), # (1 kÅ), # (0.15 kÅ). 2 Å/s rate. Ti on top helps adhesion of passivation layer. [Check AJA Sputter tool for cheaper Pt: \$0.25/sec for 1 wafer].
 - Photolith w/ MET mask [reverse for current mask].
 - Check features in microscope.
 - Descum in Aura.
 - Pattern Ti/Pt/Ti w/ Ion mill: 400V, 45°, ~15nm/min Pt etched. Etched 8 min straight without problem, but longer may bake resist enough to make it irremovable. May need longer to etch both layers of Ti.
 - Finish off pattern with dip in BOE 6:1 until hydrophobic.
 - Remove resist with Acetone dip + Piranha clean.
 - Check for resist residue. Check resistor/oxide condition.
3. Etch Cr
 - Photolith.
 - Use PT740 Cr etch recipe (kwame.bch). Etches ~13nm/min.
 - Wet etch tends to have large undercut.
4. Etch Pt with Ion-mill. Problems with fencing.
 - Photolith.
 - 400V, 45°, ~15nm/min Pt etched. Did 8 min straight etch without problem. Longer may bake resist enough to make it irremovable.
5. Etch Pt with hot Aqua regia [not very accurate, damages the metal layers]
 - Dip Pt in BOE 6:1 to remove surface oxide.
 - Aqua Regia (3:1 HNO₃:HCl) heated up to 60 °C, etches Pt at ~50nm/min
6. LOR pattern and cover frontside w/ Al for porous Si etch
 - Clean wafers in Nanostrip to prepare for Al deposition and porous Si formation.
 - Spin LOR 5A in class2 spinner, SU8 room: 3,000 RPM, 10,000 RPM/s, 45s (recipe 3000-45S). Bake 180C 5min.
 - Photolith w/ ALU mask. Expose 1.5x dose. No acetone, no P20; they damage the LOR.
 - Develop for 2x as usual, 120s DP, maybe more. Need extra time for LOR to dissolve.
 - Check features in microscope. Ensure all photoresist + LOR gone and can see oxide color below.
 - Descum in Aura.
 - Dip wafers in 6:1 BOE (will not be hydrophobic). Rinse 2x in water to remove BOE particulate. BOE helps clean glass wafers.
 - CHA conformal deposit 200nm Al. Immediately. Layers # (2 kÅ). 2 Å/s rate.

- Lift-off resist in 1165 overnight, constant stirring. IPA rinse and swab clean each wafer to remove particulate. Spin rinse.
 - Check for resist residue.
 - Warm up RTA 15 mins. MOS SIDE ONLY. Anneal 2 min @ 400 °C with Ar/H gas in RTA (recipe: ms400). Short anneal only.
7. Encapsulate in PDMS
- Dip in 1200red adhesion promoter, dilute promoter 2-4x if surface looks white/chalky (too much deposited).
 - Bake at 115C to evaporate water (check this).
 - Prepare 10:1 Sylgard 184 solution, vacuum out bubbles.
 - Place chip in test tube, encapsulate with silicone (add no more than needed), place in vacuum oven to remove all air.
 - Cure at 80C for ~2-3 hours (or 48hrs room temperature, thermal stress may damage bonds).
 - Cut & remove front protection. Do not remove from capsule lest the PDMS deform and break the wirebonds.
8. Encapsulate in adhesion + parylene + Epoxy
- Mask the chip membrane with latex or kapton tape.
 - Can use YES HDMS oven for parylene adhesion, easier.
 - In 1000 mL glass beaker, mix 400 mL of isopropanol, 400 mL of DI water, and 4 mL of A-174 adhesion promoter. Mix for 2.5 hours, or overnight.
 - Dip PCB in mixture 30 min. Dry in ambient air 30 min.
 - Dip PCB in IPA 5min, test for hydrophobicity, dry with N2 gun.
 - Bake in oven at 115°C for 30 min.
 - Deposit 5g parylene (?), takes 4.5 hours from start.
9. Pattern porous Si w/ image reversal (OLD)
- Photolith w/ POSI mask, image reversal: after exposure, run image reversal oven (~90min), UV-expose for 3x usual dose, then develop 726MIF 120s DP.
 - Check in microscope, ensure all photoresist removed. If not, develop further.
 - Descum in Aura.
 - Hard bake photoresist for 5 min @ 150 °C.
 - Etch porous silicon as usual, except (1) use less current according to open area ($20 \text{ mA/cm}^2 = 390\text{mA}$ for poSi mask w/ area of 19.5 cm^2), (2) mix ethanol and HF solution together **before** pouring on top of wafer in etch bath [otherwise the photoresist will be impossible to remove].
 - Wash w/ acetone then IPA to remove photoresist.
10. CHA LOR:
- Deposit 15/100/15nm Liftoff Ti/Pt/Ti. Immediately. Layers #14 (0.15 kÅ), #15 (1 kÅ), #14 (0.15 kÅ). 2 Å/s rate. Ti on top helps adhesion of passivation layer.
11. S1818 photolithography: expose 4s in MA6.
12. Anodic bond at Olin:
- Clip Si+glass together & bring to Olin, avoids any dust from getting into devices. Cleanliness is vital to holding large tensions!
 - Clean and polish top electrode.
 - Place Si+glass on hotplate, 470 °C (so that wafers are at ~400 °C) w/ 95mm electrode, weight on top (ensure is centered), metal pieces to keep everything from sliding, wait 50+ min for top electrode to heat up (check w/ thermometer). Connect to top electrode by top side to prevent arcing. Remove metal pieces, apply -1500V limited by 26mA. Bond for 30min. Remove wafer from hot plate and place on

counter to cool down, glass-side down to keep wire-side clean. Wait for electrode to cool down before placing next wafer sandwich to avoid sliding

REFERENCES

- (1) Borrell, a; Garside, a; Fukai, S. Improving Efficiency of Water Use for Irrigated Rice in a Semi-Arid Tropical Environment. *F. Crop Res* **1997**, *52*, 231–248.
- (2) Pye, V. I.; Patrick, R. Ground Water Contamination in the United States. *Science* **1983**, *221*, 713–718.
- (3) Lebissonais, Y.; Renaux, B.; Delouche, H. Interactions between Soil Properties and Moisture Content in Crust Formation, Runoff and Interill Erosion from Tilled Loess Soils. *Catena* **1995**, *25*, 33–46.
- (4) Han, M. Y.; Lytton, R. L. Theoretical Prediction of Drying Shrinkage of Concrete. *J. Mater. Civ. Eng.* **1995**, *7*, 204–207.
- (5) Katz, E. .; Labuza, T. . Effect of Water Activity on the Sensory Crispness and Mechanical Deformation of Snack Food Products. *J. Food Sci.* **1981**, *46*, 403–409.
- (6) Gervais, P.; Belin, J. M.; Grajek, W.; Sarrette, M. Influence of Water Activity on Aroma Production by *Trichoderma Viride* Growing on a Solid Substrate. *J. Ferment. Technol.* **1988**, *66*, 403–407.
- (7) Abdullah, N.; Nawawi, A.; Othman, I. Fungal Spoilage of Starch-Based Foods in Relation to Its Water Activity (A(w)). *J. Stored Prod. Res.* **2000**, *36*, 47–54.
- (8) Avedisian, C. T. The Homogeneous Nucleation Limits of Liquids. *J. Phys. Chem. Ref. Data* **1985**, *14*, 695–729.
- (9) Debenedetti, P. G. Supercooled and Glassy Water. *J. Phys. Condens. Matter* **2003**, *15*, 1669–1726.
- (10) Speedy, R. J.; Angell, C. A. Isothermal Compressibility of Supercooled Water and Evidence for a Thermodynamic Singularity at -45°C . *J. Chem. Phys.* **1976**, *65*, 851.
- (11) Stanley, H. E.; Angell, C. A.; Essmann, U.; Hemmati, M.; Poole, P. H.; Sciortino, F. Is There a Second Critical Point in Liquid Water? *Physica A* **1994**, *205*, 122–139.
- (12) Limmer, D. T.; Chandler, D. The Putative Liquid-Liquid Transition Is a Liquid-Solid Transition in Atomistic Models of Water. II. *J. Chem. Phys.* **2013**, *138*, 0–15.
- (13) Zheng, Q.; Durben, D. J.; Wolf, G. H.; Angell, C. A. Liquids at Large Negative Pressures: Water at the Homogeneous Nucleation Limit. *Science* **1991**, *254*, 829–832.
- (14) Caupin, F.; Herbert, E. Cavitation in Water: A Review. *Comptes Rendus Phys.* **2006**, *7*, 1000–1017.
- (15) Liu, Y.; Palmer, J. C.; Panagiotopoulos, A. Z.; Debenedetti, P. G. Liquid-Liquid Transition

- in ST2 Water. *J. Chem. Phys.* **2012**, *137*, 0–10.
- (16) Fisher, L. R.; Gamble, R. a.; Middlehurst, J. The Kelvin Equation and the Capillary Condensation of Water. *Nature* **1981**, *290*, 575–576.
 - (17) Xu, J.; Louge, M. Y. Statistical Mechanics of Unsaturated Porous Media. *Phys Rev E* **2015**, *92*, 062405.
 - (18) Naor, a. Midday Stem Water Potential As a Plant Water Stress Indicator for Irrigation Scheduling in Fruit Trees. *Methods* **2000**, *537*, 447–454.
 - (19) Prichard, T. L. *Imposing Water Deficits To Improve Wine Quality and Reduce Costs*.
 - (20) Lampinen, B. D.; Shackel, K. A.; Southwick, S. M.; Olson, W. H. Deficit Irrigation Strategies Using Midday Stem Water Potential in Prune. *Irrig. Sci.* **2001**, *20*, 47–54.
 - (21) Osakabe, Y.; Osakabe, K.; Shinozaki, K.; Tran, L.-S. P. Response of Plants to Water Stress. *Front. Plant Sci.* **2014**, *5*, 86.
 - (22) Leeuwen, C. Van; Tregoat, O.; Choné, X.; Bois, B.; Pernet, D.; Gaudillère, J. P. Vine Water Status Is a Key Factor in Grape Ripening and Vintage Quality for Red Bordeaux Wine. How Can It Be Assessed for Vineyard Management Purposes? *J. Int. des Sci. la Vigne du Vin* **2009**, *43*, 121–134.
 - (23) Choat, B.; Jansen, S.; Brodribb, T. J.; Cochard, H.; Delzon, S.; Bhaskar, R.; Bucci, S. J.; Feild, T. S.; Gleason, S. M.; Hacke, U. G.; *et al.* Global Convergence in the Vulnerability of Forests to Drought. *Nature* **2012**, *491*, 752–755.
 - (24) Nimmo, J. R.; Landa, E. R. The Soil Physics Contributions of Edgar Buckingham. *Soil Sci. Soc. Am. J.* **2005**, *69*, 328.
 - (25) Buckingham, E. *Studies on the Movement of Soil Moisture*; 1907.
 - (26) Miller, F. P. History of Soil Science : 1927 – 2000. *Soil Sci.* **2000**, *65*, 821–825.
 - (27) Larter, M.; Brodribb, Timothy, J.; Pfautsch, S.; Burlett, R.; Cochard, H.; Delzon, S. Extreme Aridity Pushes Trees to Their Physical Limits. *Plant Physiol.* **2015**, *168*, pp.00223.2015.
 - (28) Stroock, A. D.; Pagay, V. V.; Zwieniecki, M. A.; Michele Holbrook, N. The Physicochemical Hydrodynamics of Vascular Plants. *Annu. Rev. Fluid Mech.* **2014**, *46*, 615–642.
 - (29) Holbrook, N. M.; Zwieniecki, M. a. Embolism Repair and Xylem Tension: Do We Need a Miracle? *Plant Physiol.* **1999**, *120*, 7–10.
 - (30) Brodersen, C. R.; McElrone, A. J.; Choat, B.; Lee, E. F.; Shackel, K. A.; Matthews, M. A. In Vivo Visualizations of Drought-Induced Embolism Spread in *Vitis Vinifera*. *Plant Physiol.* **2013**, *161*, 1820–1829.

- (31) Brodersen, C. R.; McElrone, A. J.; Choat, B.; Matthews, M. A.; Shackel, K. A. The Dynamics of Embolism Repair in Xylem: In Vivo Visualizations Using High-Resolution Computed Tomography. *Plant Physiol.* **2010**, *154*, 1088–1095.
- (32) Wheeler, T. D.; Stroock, A. D. The Transpiration of Water at Negative Pressures in a Synthetic Tree. *Nature* **2008**, *455*, 208–212.
- (33) Bailey, I. W. The Structure of the Bordered Pits of Conifers and Its Bearing upon the Tension Hypothesis of the Ascent of Sap in Plants. *Bot. Gaz.* **1916**, *62*, 133–142.
- (34) Wheeler, J. K.; Sperry, J. S.; Hacke, U. G.; Hoang, N. Inter-Vessel Pitting and Cavitation in Woody Rosaceae and Other Vessel Led Plants: A Basis for a Safety versus Efficiency Trade-off in Xylem Transport. *Plant, Cell Environ.* **2005**, *28*, 800–812.
- (35) Choat, B.; Brodie, T. W.; Cobb, A. R.; Zwieniecki, M. A.; Holbrook, N. M. Direct Measurements of Intervessel Pit Membrane Hydraulic Resistance in Two Angiosperm Tree Species. *Am. J. Bot.* **2006**, *93*, 993–1000.
- (36) Zwieniecki, M. A. Bordered Pit Structure and Vessel Wall Surface Properties. Implications for Embolism Repair. *Plant Physiol.* **2000**, *123*, 1015–1020.
- (37) Pesacreta, T.; Groom, L.; Rials, T. Atomic Force Microscopy of the Intervessel Pit Membrane in the Stem of *Sapium Sebiferum* (Euphorbiaceae). *Iawa J.* **2005**, *26*, 397–426.
- (38) Halis, Y.; Djehichi, S.; Senoussi, M. M. Vessel Development and the Importance of Lateral Flow in Water Transport within Developing Bundles of Current-Year Shoots of Grapevine (*Vitis Vinifera* L.). *Trees - Struct. Funct.* **2012**, *26*, 705–714.
- (39) Tyree, M.; Ewers, F. The Hydraulic Architecture of Trees and Other Woody Plants. *New Phytol.* **1991**, *119*, 345–360.
- (40) Konrad, W.; Roth-Nebelsick, A. The Significance of Pit Shape for Hydraulic Isolation of Embolized Conduits of Vascular Plants during Novel Refilling. *J. Biol. Phys.* **2005**, *31*, 57–71.
- (41) Choat, B.; Cobb, A. R.; Jansen, S. Structure and Function of Bordered Pits: New Discoveries and Impacts on Whole-Plant Hydraulic Function. *New Phytol.* **2008**, *177*, 608–626.
- (42) Jansen, S.; Choat, B.; Pletsers, A. Morphological Variation of Intervessel Pit Membranes and Implications to Xylem Function in Angiosperms. *Am. J. Bot.* **2009**, *96*, 409–419.
- (43) Roper, M. C.; Greve, L. C.; Warren, J. G.; Labavitch, J. M.; Kirkpatrick, B. C. *Xylella Fastidiosa* Requires Polygalacturonase for Colonization and Pathogenicity in *Vitis Vinifera* Grapevines. *Mol. Plant-Microbe Interact.* **2007**, *20*, 411–419.
- (44) Christman, M. A.; Sperry, J. S.; Smith, D. D. Rare Pits, Large Vessels and Extreme Vulnerability to Cavitation in a Ring-Porous Tree Species. *New Phytol.* **2012**, *193*, 713–

720.

- (45) Tyree, M. T.; Salleo, S.; Nardini, A.; Gullo, M. A. Lo; Mosca, R. Refilling of Embolized Vessels in Young Stems of Laurel. Do We Need a New Paradigm?1. *Plant Physiol.* **1999**, *120*, 11–22.
- (46) Zimmermann, M. H. Hydraulic Architecture of Some Diffuse-Porous Trees. *Can. J. Bot.* **1978**, *56*, 2286–2295.
- (47) Lopez-Portillo, J.; Ewers, F. W.; Angeles, G. Sap Salinity Effects on Xylem Conductivity in Two Mangrove Species. *Plant, Cell Environ.* **2005**, *28*, 1285–1292.
- (48) Pittermann, J.; Sperry, J. S.; Hacke, U. G.; Wheeler, J. K.; Sikkema, E. H. Torus-Margo Pits Help Conifers Compete with Angiosperms. *Science (80-.)*. **2005**, *310*, 1924–1924.
- (49) Hacke, U. G.; Sperry, J. S.; Wheeler, J. K.; Castro, L. Scaling of Angiosperm Xylem Structure with Safety and Efficiency. *Tree Physiol.* **2006**, *26*, 689–701.
- (50) Domec, J.-C.; Meinzer, F. C.; Lachenbruch, B.; Housset, J. Dynamic Variation in Sapwood Specific Conductivity in Six Woody Species. *Tree Physiol.* **2007**, *27*, 1389–1400.
- (51) Nardini, A.; Gascò, A.; Trifilò, P.; Lo Gullo, M. A.; Salleo, S. Ion-Mediated Enhancement of Xylem Hydraulic Conductivity Is Not Always Suppressed by the Presence of Ca²⁺ in the Sap. *J. Exp. Bot.* **2007**, *58*, 2609–2615.
- (52) Aasamaa, K.; SÖBER, A. Sensitivity of Stem and Petiole Hydraulic Conductance of Deciduous Trees to Xylem Sap Ion Concentration. *Biol. Plant.* **2010**, *54*, 299–307.
- (53) Zwieniecki, M. A.; Melcher, P. J.; Holbrook, N. M. Hydrogel Control of Xylem. *Science (80-.)*. **2001**, *291*, 1059–1062.
- (54) van Ieperen, W. Fluid Ionic Composition Influences Hydraulic Conductance of Xylem Conduits. *J. Exp. Bot.* **2000**, *51*, 769–776.
- (55) Gascó, A.; Nardini, A.; Gortan, E.; Salleo, S. Ion-Mediated Increase in the Hydraulic Conductivity of Laurel Stems: Role of Pits and Consequences for the Impact of Cavitation on Water Transport. *Plant, Cell Environ.* **2006**, *29*, 1946–1955.
- (56) Neumann, P. M.; Weissman, R.; Stefano, G.; Mancuso, S. Accumulation of Xylem Transported Protein at Pit Membranes and Associated Reductions in Hydraulic Conductance. *J. Exp. Bot.* **2010**, *61*, 1711–1717.
- (57) Van Meeteren, U.; Van Gelder, H.; Van Ieperen, W. Reconsideration of the Use of Deionized Water as Vase Water in Postharvest Experiments on Cut Flowers. *Postharvest Biol. Technol.* **1999**, *17*, 175–187.
- (58) Cochard, H.; Herbette, S.; Hernández, E.; Hölttä, T.; Mencuccini, M. The Effects of Sap Ionic Composition on Xylem Vulnerability to Cavitation. *J. Exp. Bot.* **2010**, *61*, 275–285.

- (59) Zwieniecki, M. a; Melcher, P. J.; Feild, T. S.; Holbrook, N. M. A Potential Role for Xylem-Phloem Interactions in the Hydraulic Architecture of Trees: Effects of Phloem Girdling on Xylem Hydraulic Conductance. *Tree Physiol.* **2004**, *24*, 911–917.
- (60) Trifilò, P.; Lo Gullo, M. a; Salleo, S.; Callea, K.; Nardini, A. Xylem Embolism Alleviated by Ion-Mediated Increase in Hydraulic Conductivity of Functional Xylem: Insights from Field Measurements. *Tree Physiol.* **2008**, *28*, 1505–1512.
- (61) van Ieperen, W. Ion-Mediated Changes of Xylem Hydraulic Resistance in Planta: Fact or Fiction? *Trends Plant Sci.* **2007**, *12*, 137–142.
- (62) Van Ieperen, W.; Van Gelder, A. Ion-Mediated Flow Changes Suppressed by Minimal Calcium Presence in Xylem Sap in Chrysanthemum and Prunus Laurocerasus. *J. Exp. Bot.* **2006**, *57*, 2743–2750.
- (63) Lee, J.; Holbrook, N. M.; Zwieniecki, M. a. Ion Induced Changes in the Structure of Bordered Pit Membranes. *Front. Plant Sci.* **2012**, *3*, 55.
- (64) van Doorn, W. G.; Hiemstra, T.; Fanourakis, D. Hydrogel Regulation of Xylem Water Flow: An Alternative Hypothesis. *Plant Physiol.* **2011**, *157*, 1642–1649.
- (65) Rice, C. L.; Whitehead, R. Electrokinetic Flow in a Narrow Cylindrical Capillary. *J. Phys. Chem.* **1965**, *69*, 4017–4024.
- (66) Kirby, B. J. *Micro-and Nanoscale Fluid Mechanics: Transport in Microfluidic Devices*; 1st ed.; Cambridge University Press: New York, 2010.
- (67) Brien, T. P. O.; Thimann, K. V. Observations on the Fine Structure Of the Oat Coleoptile III . Correlated Light and Electron Microscopy of the Vascular Tissues (Received July I , 1966) Introduction. *Protoplasma* **1966**, *63*, 443–478.
- (68) O’Brien, T. P. Further Observations on Hydrolysis of the Cell Wall in the Xylem. *Protoplasma* **1970**, *69*, 1–14.
- (69) Stamm, A. J. Electroendosmose through Wood Membranes. *Colloid Symposium Monograph*, 1926, 246–257.
- (70) Tyree, M. T.; Fensom, D. S. Methods of Measuring Hydrokinetic Pressure Gradients in the Xylem of Plants *in Situ*. *Can. J. Bot.* **1968**, *46*, 310–315.
- (71) Tyree, M. T.; Zimmermann, M. H. The Theory and Practice of Measuring Transport Coefficients and Sap Flow in the Xylem of Red Maple Stems (*Acer Rubrum*). *J. Exp. Bot.* **1971**, *22*, 1–18.
- (72) Jansen, S.; Gortan, E.; Lens, F.; Lo Gullo, M. A.; Salleo, S.; Scholz, A.; Stein, A.; Trifilò, P.; Nardini, A. Do Quantitative Vessel and Pit Characters Account for Ion-Mediated Changes in the Hydraulic Conductance of Angiosperm Xylem? *New Phytol.* **2011**, *189*, 218–228.

- (73) Nardini, A.; Salleo, S.; Jansen, S. More than Just a Vulnerable Pipeline: Xylem Physiology in the Light of Ion-Mediated Regulation of Plant Water Transport. *J. Exp. Bot.* **2011**, *62*, 4701–4718.
- (74) Kuljanin, T. A.; Lević, L. B.; Mišljenović, N. M.; Koprivica, G. B. Electric Double Layer and Electrokinetic Potential of Pectic Macromolecules in Sugar Beet. *Acta Period. Technol.* **2008**, *39*, 21–28.
- (75) Nakauma, M.; Funami, T.; Noda, S.; Ishihara, S.; Al-Assaf, S.; Nishinari, K.; Phillips, G. O. Comparison of Sugar Beet Pectin, Soybean Soluble Polysaccharide, and Gum Arabic as Food Emulsifiers. 1. Effect of Concentration, pH, and Salts on the Emulsifying Properties. *Food Hydrocoll.* **2008**, *22*, 1254–1267.
- (76) Dong, D.; Fricke, A. L.; Moudgil, B. M.; Johnson, H. Electrokinetic Study of Kraft Lignin. *Tappi J.* **1996**, *79*, 191–197.
- (77) Kim, Y.; Teng, Q.; Wicker, L. Action Pattern of Valencia Orange PME de-Esterification of High Methoxyl Pectin and Characterization of Modified Pectins. *Carbohydr. Res.* **2005**, *340*, 2620–2629.
- (78) Bellmann, C.; Caspari, A.; Albrecht, V.; Loan Doan, T. T.; Mäder, E.; Luxbacher, T.; Kohl, R. Electrokinetic Properties of Natural Fibres. *Colloids Surfaces A Physicochem. Eng. Asp.* **2005**, *267*, 19–23.
- (79) Behrens, S. H.; Grier, D. G. The Charge of Glass and Silica Surfaces. *J. Chem. Phys.* **2001**, *115*, 6716–6721.
- (80) Choat, B.; Ball, M.; Luly, J.; Holtum, J. Pit Membrane Porosity and Water Stress-Induced Cavitation in Four Co-Existing Dry Rainforest Tree Species. **2016**, *131*, 41–48.
- (81) Pérez-Donoso, A. G.; Sun, Q.; Roper, M. C.; Greve, L. C.; Kirkpatrick, B.; Labavitch, J. M. Cell Wall-Degrading Enzymes Enlarge the Pore Size of Intervessel Pit Membranes in Healthy and Xylella Fastidiosa-Infected Grapevines. *Plant Physiol.* **2010**, *152*, 1748–1759.
- (82) Schurr, U.; E.D.Schulze. The Concentration of Xylem Sap Constituents in Root Exudate, and in Sap from Intact, Trnspiring Castor Bean Plants (*Ricinus Communis* L.). *Plant, Cell Environ.* **1995**, *18*, 409–420.
- (83) Siebrecht, S.; Herdel, K.; Schurr, U.; Tischner, R. Nutrient Translocation in the Xylem of Poplar - Diurnal Variations and Spatial Distribution along the Shoot Axis. *Planta* **2003**, *217*, 783–793.
- (84) Herdel, K.; Schmidt, P.; Feil, R.; Mohr, A.; Schurr, U. Dynamics of Concentrations and Nutrient Fluxes in the Xylem of *Ricinus Communis* - Diurnal Course, Impact of Nutrient Availability and Nutrient Uptake. *Plant, Cell Environ.* **2001**, *24*, 41–52.
- (85) Marschner, H. *Mineral Nutrition of Higher Plants*; 2nd ed.; Academic Press: London, 2008; Vol. 11.

- (86) Sun, Q.; Rost, T. L.; Matthews, M. A. Wound-Induced Vascular Occlusions in *Vitis Vinifera* (Vitaceae): Tyloses in Summer and Gels in Winter. *Am. J. Bot.* **2008**, *95*, 1498–1505.
- (87) Gascó, A.; Gortan, E.; Salleo, S.; Nardini, A. Changes of pH of Solutions during Perfusion through Stem Segments: Further Evidence for Hydrogel Regulation of Xylem Hydraulic Properties? *Biol. Plant.* **2008**, *52*, 502–506.
- (88) Sperry, J. S.; Donnelly, J. R.; Tyree, M. T. Seasonal Occurrence of Xylem Embolism in Sugar Maple (*Acer Saccharum*). *Am. J. Bot.* **1988**, *75*, 1212–1218.
- (89) Huisman, I. H.; Prádanos, P.; Calvo, J. I.; Hernández, A. Electroviscous Effects, Streaming Potential, and Zeta Potential in Polycarbonate Track-Etched Membranes. *J. Memb. Sci.* **2000**, *178*, 79–92.
- (90) Stellan Hjertén. Free Zone Electrophoresis. *Chromatogr. Rev.* **1967**, *9*, 122–143, 147–219.
- (91) Kirby, B. J.; Hasselbrink, E. F. Zeta Potential of Microfluidic Substrates: 1. Theory, Experimental Techniques, and Effects on Separations. *Electrophoresis* **2004**, *25*, 187–202.
- (92) Werner, C.; Zimmermann, R.; Kratzmuller, T. Streaming Potential and Streaming Current Measurements at Planar Solid/liquid Interfaces for Simultaneous Determination of Zeta Potential and Surface Conductivity. *Colloids Surfaces A Physicochem. Eng. Asp.* **2001**, *192*, 205–213.
- (93) Bob B Buchanan; Gruissem, W.; Jones, R. L. *Biochemistry and Molecular Biology of Plants*; 1st ed.; American Society of Plant Physiologists: Rockville, 2002.
- (94) Zwieniecki, M. A.; Holbrook, N. M. Confronting Maxwell's Demon: Biophysics of Xylem Embolism Repair. *Trends Plant Sci.* **2009**, *14*, 530–534.
- (95) Secchi, F.; Zwieniecki, M. a. Analysis of Xylem Sap from Functional (Nonembolized) and Nonfunctional (Embolized) Vessels of *Populus Nigra*: Chemistry of Refilling. *Plant Physiol.* **2012**, *160*, 955–964.
- (96) Schmid, R.; Machado, P. Pit Membranes in Hard Woods - Fine Structure and Development. *Protoplasma* **1968**, *66*, 185–204.
- (97) Gregory, S. C.; Petty, J. A. Value Action of Bordered Pits in Conifers. *J. Exp. Bot.* **1973**, *24*, 763–765.
- (98) Spanner, D. C. The Translocation of Sugar in Sieve Tubes. *J. Exp. Bot.* **1958**, *9*, 332–342.
- (99) Fensom, D. The Bioelectric Potentials of Plants and Their Functional Significance: Iv. Changes in the Rate of Water Absorption in Excised. *Can. J. Bot.* **1962**, *40*, 573–582.
- (100) Spanner, D. The Electroosmotic Theory of Phloem Transport: A Final Restatement. *Plant Cell Environ.* **1979**, *2*, 107–121.

- (101) Yao, S.; Santiago, J. G. Porous Glass Electroosmotic Pumps: Theory. *J. Colloid Interface Sci.* **2003**, *268*, 133–142.
- (102) Grahame, D. C. The Electrical Double Layer and the Theory of Electrocapillarity. *Chem. Rev.* **1947**, *41*, 441–501.
- (103) Bowen, W. R.; Jenner, F. Electroviscous Effects in Charged Capillaries. *Journal of Colloid and Interface Science*, 1995, *173*, 388–395.
- (104) Butler, J. N. *Carbon Dioxide Equilibria and Their Applications*; 1st ed.; Addison-Wesley: Reading, 1982.
- (105) Scholander, P. F.; Hammel, H. T.; Bradstreet, E. D.; Hemmingsen, E. A. Sap Pressure in Vascular Plants: Negative Hydrostatic Pressure Can Be Measured in Plants. *Science (80-)*. **1965**, *148*, 339–346.
- (106) Tobiessen, P.; Rundel, P. W. Water Potential Gradient in a Tall Sequoiadendron. *Plant Physiol.* **1971**, *48*, 303–304.
- (107) Smith, A. M. Negative Pressure Generated By Octopus Suckers: A Study of the Tensile Strength of Water in Nature. *J. Exp. Biol.* **1991**, *157*, 257–271.
- (108) Guan, Y.; Fredlund, D. G. Use of the Tensile Strength of Water for the Direct Measurement of High Soil Suction. *Can. Geotech. J.* **1997**, *34*, 604–614.
- (109) Roedder, E. Metastable Superheated Ice in Liquid-Water Inclusions under High Negative Pressure. *Science (80-)*. **1967**, *155*, 1413–1417.
- (110) Arndt, R. E. a. Cavitation in Fluid Machinery and Hydraulic Structures. *Annu. Rev. Fluid Mech.* **1981**, *13*, 273–328.
- (111) Choi, J. H.; Penmetsa, R. C.; Grandhi, R. V. Shape Optimization of the Cavitator for a Supercavitating Torpedo. *Struct. Multidiscip. Optim.* **2005**, *29*, 159–167.
- (112) Lamminen, M. O.; Walker, H. W.; Weavers, L. K. Mechanisms and Factors Influencing the Ultrasonic Cleaning of Particle-Fouled Ceramic Membranes. *J. Memb. Sci.* **2004**, *237*, 213–223.
- (113) Group, E.; Museum, A. Morphological Phylogeny of Alpheid Shrimps: Parallel Preadaptation and the Origin of a Key Morphological Innovation ., **2010**, *60*, 2507–2528.
- (114) Pallares, G.; El Mekki Azouzi, M.; González, M. A.; Aragonés, J. L.; Abascal, J. L. F.; Valeriani, C.; Caupin, F. Anomalies in Bulk Supercooled Water at Negative Pressure. *Proc. Natl. Acad. Sci. U. S. A.* **2014**, *111*, 7936–7941.
- (115) Hayward, A. T. J. Mechanical Pump with a Suction Lift of 17 Metres. *Nature* **1970**, *225*, 376–377.

- (116) Chen, I.; Pharkya, A.; Stroock, A. Analysis of Superheated Loop Heat Pipes Exploiting Nanoporous Wick Membranes. *AIChE J.* **2014**.
- (117) Revised Release on the IAPWS Formulation 1995 for the Thermodynamic Properties of Ordinary Water Substance for General and Scientific Use, 2009.
- (118) Pallares, G.; Gonzalez, M. A.; Abascal, J. L. F.; Valeriani, C.; Caupin, F. Equation of State for Water and Its Line of Density Maxima down to -120 MPa. *Phys. Chem. Chem. Phys.* **2016**, *18*, 5896–5900.
- (119) Caupin, F.; Stroock, A. The Stability Limit and Other Open Questions on Water at Negative Pressure. *Adv. Chem. Physics, Liq. ...* **2013**, *152*, 51–80.
- (120) Galloway, W. J. An Experimental Study of Acoustically Induced Cavitation in Liquids. *J. Acoust. Soc. Am.* **1954**, *26*, 849–857.
- (121) Caupin, F.; Balibar, S. Cavitation Pressure in Liquid Helium. *Phys. Rev.* **2001**, *64*, 11.
- (122) Davitt, K.; Rolley, E.; Caupin, F.; Arvengas, A.; Balibar, S. Equation of State of Water under Negative Pressure. *J. Chem. Phys.* **2010**, *133*, 174507.
- (123) Henderson, S. J.; Speedy, R. J. A Berthelot-Bourdon Tube Method for Studying Water under Tension. *J. Phys. E.* **1980**, *13*, 778–782.
- (124) Rovetta, M. R.; Blacic, J. D.; Hervig, R. L.; Holloway, J. R. An Experimental Study of Hydroxyl in Quartz Using Infrared Spectroscopy and Ion Microprobe Techniques. *J. Geophys. Res.* **1989**, *94*, 5840–5850.
- (125) Briggs, L. J. Limiting Negative Pressure of Water. *J. Appl. Phys.* **1950**, *21*, 721.
- (126) Huang, H. S. PVT Behavior of Water at Negative Pressures: Capillary Tube Deformation Effects. *J. Chem. Phys.* **1973**, *59*, 6191.
- (127) Macdonald, J. R. Reconsideration of an Experiment on Water under Negative Pressure. *J. Chem. Phys.* **1972**, *57*, 3793.
- (128) Dixon, H.; Joly, J. On the Ascent of Sap. *Philos. Trans. R. Soc.* **1895**.
- (129) Machin, W. D. A Simple Method for the Generation of Negative Pressure in Liquids. *Can. J. Chem.* **1998**, *76*, 1578–1580.
- (130) Pagay, V.; Santiago, M.; Sessoms, D. a; Huber, E. J.; Vincent, O.; Pharkya, A.; Corso, T. N.; Lakso, A. N.; Stroock, A. D. A Microtensiometer Capable of Measuring Water Potentials below -10 MPa. *Lab Chip* **2014**, *14*, 2806–2817.
- (131) Arvengas, A.; Herbert, E.; Cersoy, S.; Davitt, K.; Caupin, F. Cavitation in Heavy Water and Other Liquids. *J. Phys. Chem. B* **2011**, *115*, 14240–14245.
- (132) Wheeler, T. D.; Stroock, A. D. Stability Limit of Liquid Water in Metastable Equilibrium

- with Subsaturated Vapors. *Langmuir* **2009**, *25*, 7609–7622.
- (133) Vincent, O.; Szenicer, A.; Stroock, A. D. Capillarity-Driven Flows at the Continuum Limit. *Prepr. arXiv1510.00411* **2015**, 1–5.
- (134) Wygant, I. O. Analytically Calculating Membrane Displacement and the Equivalent Circuit Model of a Circular CMUT Cell. *IEEE Int. Ultrason. Symp.* **2008**, 2111–2114.
- (135) Murphy, D. M.; Koop, T. Review of the Vapour Pressures of Ice and Supercooled Water for Atmospheric Applications. *Q. J. R. Meteorol. Soc.* **2005**, *131*, 1539–1565.
- (136) NIST. Thermophysical Properties of Fluid Systems <http://webbook.nist.gov/chemistry/fluid/>.
- (137) Vincent, O.; Sessoms, D. A.; Huber, E. J.; Guioth, J.; Stroock, A. D. Drying by Cavitation and Poroelastic Relaxations in Porous Media with Macroscopic Pores Connected by Nanoscale Throats. *Phys. Rev. Lett.* **2014**, *113*, 1–5.
- (138) I-Tzu Chen, David Sessoms, Zachary Sherman, Eugene Choi, O. V. and A. S. Stability Limit of Water by Metastable Liquid-Vapor Equilibrium with Nanoporous Silicon Membranes. *Prep.* **2015**.
- (139) Caupin, F.; Arvengas, A.; Davitt, K.; Azouzi, M. E. M.; Shmulovich, K. I.; Ramboz, C.; Sessoms, D. a; Stroock, A. D. Exploring Water and Other Liquids at Negative Pressure. *J. Phys. Condens. Matter* **2012**, *24*, 284110.
- (140) Henderson, S.; Speedy, R. Temperature of Maximum Density in Water at Negative Pressure. *J. Phys. Chem.* **1987**, *17*, 3062–3068.
- (141) Malaeb, L.; Ayoub, G. M. Reverse Osmosis Technology for Water Treatment: State of the Art Review. *Desalination* **2011**, *267*, 1–8.
- (142) Loeb, S. Large-Scale Power Production by Pressure-Retarded Osmosis, Using River Water and Sea Water Passing through Spiral Modules. *Desalination* **2002**, *143*, 115–122.
- (143) Millionis, H. J.; Liamis, G. L.; Elisaf, M. S. The Hyponatremic Patient: A Systematic Approach to Laboratory Diagnosis. *Cmaj* **2002**, *166*, 1056–1062.
- (144) Lemp, M. A.; Bron, A. J.; Baudouin, C.; Bentez Del Castillo, J. M.; Geffen, D.; Tauber, J.; Foulks, G. N.; Pepose, J. S.; Sullivan, B. D. Tear Osmolarity in the Diagnosis and Management of Dry Eye Disease. *Am. J. Ophthalmol.* **2011**, *151*, 792–798.
- (145) Jensen, O. M.; Hansen, P. F. Autogenous Deformation and RH-Change in Perspective. *Cem. Concr. Res.* **2001**, *31*, 1859–1865.
- (146) Lura, P.; Jensen, O. M.; Van Breugel, K. Autogenous Shrinkage in High-Performance Cement Paste: An Evaluation of Basic Mechanisms. *Cem. Concr. Res.* **2003**, *33*, 223–232.

- (147) Lura, P.; Jensen, O. M.; Igarashi, S.-I. Experimental Observation of Internal Water Curing of Concrete. *Mater. Struct.* **2007**, *40*, 211–220.
- (148) Mugnier, J.; Jung, G. Survival of Bacteria and Fungi in Relation to Water Activity and the Solvent Properties of Water in Biopolymer Gels. *Appl. Environ. Microbiol.* **1985**, *50*, 108–114.
- (149) Philip, J. R. Plant Water Relations: Some Physical Aspects. *Annu. Rev. Plant Physiol.* **1966**, *17*, 245–268.
- (150) Plaut, Z.; Ben-Hur, M.; Meiri, A. Yield and Vegetative Growth as Related to Plant Water Potential of Cotton Irrigated with a Moving Sprinkler System at Different Frequencies and Wetting Depths. *Irrig. Sci.* **1992**, *13*, 39–44.
- (151) Stewart, W. L.; Fulton, A. E.; Krueger, W. H.; Lampinen, B. D.; Shackel, K. A. Regulated Deficit Irrigation Reduces Water Use of Almonds without Affecting Yield. *Calif. Agric.* **2011**, *65*, 90–95.
- (152) Sterling, E. M.; Arundel, A.; Sterling, T. D. Criteria for Human Exposure to Humidity in Occupied Buildings. In *ASHRAE Transactions*; 1985; Vol. 91, pp. 611–622.
- (153) Beuchat, L. Microbial Stability as Affected by Water Activity. *Cereal Foods World* **1981**, *26.7*, 345–349.
- (154) Duffy, G. A.; Lundsten, L.; Kuhnz, L. A.; Paull, C. K. A Comparison of Megafaunal Communities in Five Submarine Canyons off Southern California, USA. *Deep. Res. Part II Top. Stud. Oceanogr.* **2014**, *104*, 259–266.
- (155) Doneen, L. D.; MAcGillivray, J. . Germination of Vegetable Seed As Affected By Different Soil Moisture Conditions. *Plant Physiol.* **1943**, 524–529.
- (156) Roveti, D. K. Choosing a Humidity Sensor: A Review of Three Technologies. *Sensors* **2001**, *18*, 54–58.
- (157) Dixon, M. A.; Tyree, M. T. A New Stem Hygrometer, Corrected for Temperature Gradients and Calibrated against the Pressure Bomb. *Plant, Cell Environ.* **1984**, *7*, 693–697.
- (158) Agus, S. S.; Schanz, T. Comparison of Four Methods for Measuring Total Suction. *Vadose Zo. J.* **2005**, *4*, 1087.
- (159) Kiyosawa, K. Theoretical and Experimental Studies on Freezing Point Depression and Vapor Pressure Deficit as Methods to Measure Osmotic Pressure of Aqueous Polyethylene Glycol and Bovine Serum Albumin Solutions. *Biophys. Chem.* **2003**, *104*, 171–188.
- (160) Sereno, A. M.; Hubinger, M. D.; Comesaña, J. F.; Correa, A. Prediction of Water Activity of Osmotic Solutions. *J. Food Eng.* **2001**, *49*, 103–114.
- (161) Chahine, N. O.; Chen, F. H.; Hung, C. T.; Ateshian, G. a. Direct Measurement of Osmotic

- Pressure of Glycosaminoglycan Solutions by Membrane Osmometry at Room Temperature. *Biophys. J.* **2005**, *89*, 1543–1550.
- (162) Tyree, M. T.; Hammel, H. T. The Measurement of the Turgor Pressure and the Water Relations of Plants by the Pressure-Bomb Technique. *J. Exp. Bot.* **1972**, *23*, 267–282.
- (163) Richards, L. A. Porous Plate Apparatus for Measuring Moisture Retention and Transmission by Soil. *Soil Sci.* **1948**, *66*, 105–110.
- (164) Cassel, D. K.; Carolina, N.; Klute, A. Water Potential : Tensiometry. **1986**, *9*.
- (165) Bittelli, M.; Flury, M. Errors in Water Retention Curves Determined with Pressure Plates. *Soil Sci. Soc. Am. J.* **2009**, *73*, 1453.
- (166) Louge, M. Y.; Valance, A.; Babah, H. M.; Moreau-Trouve, J. C.; El-Moctar, A. O.; Dupont, P.; Ahmedou, D. O. Seepage-Induced Penetration of Water Vapor and Dust beneath Ripples and Dunes. *J. Geophys. Res. Earth Surf.* **2010**, *115*, F02002.
- (167) Rotronic HC2-SH <http://www.rotronic.com/hc2-sh.html>.
- (168) Louge, M. Y.; Valance, A.; El-moctar, A. O.; Xu, J.; Hay, A. G.; Richer, R. Temperature and Humidity within a Mobile Barchan Sand Dune, Implications for Microbial Survival. *J. Geophys. Res. Earth Surf.* **2013**, *118*, 2392–2405.
- (169) Farahani, H.; Wagiran, R.; Hamidon, M. N. *Humidity Sensors Principle, Mechanism, and Fabrication Technologies: A Comprehensive Review*; 2014; Vol. 14.
- (170) WP4C Water Potential Meter <https://www.decagon.com/en/soils/benchtop-instruments/wp4c-water-potential-meter/>.
- (171) Elitech (Acquired Wescor). Vapro Vapor pressure Osmometer <http://www.elitechgroup.com>.
- (172) Dixon, M.; Downey, A. . PSY1 Stem Psychrometer Manual <http://au.ictinternational.com/products/psy1/psy1-stem-psychrometer/>.
- (173) Advanced® Model 3250 Single-Sample Osmometer <http://www.aicompanies.com/index.cfm/products/?productId=3>.
- (174) Grattoni, A.; Canavese, G.; Montevecchi, F. M.; Ferrari, M. Fast Membrane Osmometer as Alternative to Freezing Point and Vapor Pressure Osmometry. *Anal. Chem.* **2008**, *80*, 2617–2622.
- (175) T4 Field Tensiometer <https://www.decagon.com/en/soils/water-potential/t4-field-tensiometer/>.
- (176) Analysis, P. Standard Test Methods for Determination of the Soil Water Characteristic Curve for Desorption Using a Hanging Column , Pressure Extractor , Chilled Mirror

- Hygrometer , and / or Centrifuge 1. *Water* **2003**, 04, 20.
- (177) Boyer, J. S. Leaf Water Potentials Measured with a Pressure Chamber. *Plant Physiol.* **1967**, 42, 133–137.
- (178) Schindler, U.; Durner, W.; von Unold, G.; Mueller, L.; Wieland, R. The Evaporation Method: Extending the Measurement Range of Soil Hydraulic Properties Using the Air-Entry Pressure of the Ceramic Cup. *J. Plant Nutr. Soil Sci.* **2010**, 173, 563–572.
- (179) Kaajakari, C. V. *Practical MEMs Book*; Small Gear Publishing, 2009.
- (180) Mosser, V.; Suski, J.; Goss, J.; Obermeier, E. Piezoresistive Pressure Sensors Based on Polycrystalline Silicon. *Sensors Actuators A. Phys.* **1991**, 28, 113–132.
- (181) Kumar, S. S.; Pant, B. D. Design Principles and Considerations for the “Ideal” Silicon Piezoresistive Pressure Sensor: A Focused Review. *Microsyst. Technol.* **2014**, 20, 1213–1247.
- (182) Obermeier, E. Polysilicon Layers Lead to a New Generation of Pressure Sensors. In *Proc. 3rd Int. Conf. Solid-State Sensors and Actuators (Transducers ' 85)*; Philadelphia, PA, USA, 1985; pp. 527–536.
- (183) Khakpour, R.; Mansouri, S. R. M.; Bahadorimehr, A. R. Analytical Comparison for Square, Rectangular and Circular Diaphragms in MEMS Applications. *2010 Int. Conf. Electron. Devices, Syst. Appl. ICEDSA 2010 - Proc.* **2010**, 297–299.
- (184) Gridchin, V. a.; Lubimsky, V. M.; Sarina, M. P. Piezoresistive Properties of Polysilicon Films. *Sensors and Actuators A: Physical*, 1995, 49, 67–72.
- (185) Olszacki, M. *Modelling and Optimization of Piezoresistive Pressure Sensors*, 2009.
- (186) Hourdakis, E.; Nassiopoulou, a G. Single Photoresist Masking for Local Porous Si Formation. *J. Micromechanics Microengineering* **2014**, 24, 117002.
- (187) Krüger, M.; Arens-Fischer, R.; Thönissen, M.; Münder, H.; Berger, M. G.; Lüth, H.; Hilbrich, S.; Theiss, W.; Krtiger, M.; Liith, H.; *et al.* Formation of Porous Silicon on Patterned Substrates. *Thin Solid Films* **1996**, 276, 257–260.
- (188) Yadav, M.; Lin, T.-W.; Johnson, H. T.; Horn, G. P. Anisothermal Anodic Bonding: A Method to Control Global Curvature and Residual Stress. In; 2010; Vol. 33, pp. 563–572.
- (189) Ninni, L.; Camargo, M. S.; Meirelles, A. J. A. Water Activity in Poly (Ethylene Glycol) Aqueous Solutions. *Thermochim. Acta* **1999**, 328, 169–176.
- (190) Schindler, U.; Müller, L. Simplifying the Evaporation Method for Quantifying Soil Hydraulic Properties. *J. Plant Nutr. Soil Sci.* **2006**, 169, 623–629.
- (191) Cresswell, H. P.; Green, T. W.; McKenzie, N. J. The Adequacy of Pressure Plate Apparatus

- for Determining Soil Water Retention. *Soil Sci. Soc. Am. J.* **2008**, 72, 41.
- (192) Ithaca Cornell NEWA weather station <http://newa.cornell.edu/index.php?page=all-weather-data>.
- (193) Lago, A. Platinum Metallization for MEMS Application: Focus on Coating Adhesion for Biomedical Applications. *Biomatter* **2014**, 4, 2–8.
- (194) Tuller, M.; Or, D. Retention of Water in Soil and the Soil Water Characteristic Curve. *Encycl. soils Environ.* **2004**, 4, 278–289.
- (195) Šimůnek, J. Parameter Estimation Analysis of the Evaporation Method for Determining Soil Hydraulic Properties. *Soil Sci. Soc. ...* **1998**, 894–905.
- (196) Wendroth, O.; Ehlers, W.; Kage, H.; Hopmans, J. W.; Halbertsma, J.; Wösten, J. H. M. Reevaluation of the Evaporation Method for Determining Hydraulic Functions in Unsaturated Soils. *Soil Sci. Soc. Am. J.* **1993**, 57, 1436.
- (197) Lorenz, M.; Granke, O. Deposition Measurements and Critical Loads Calculations: Monitoring Data, Results and Perspective. *IForest* **2009**, 2, 11–14.
- (198) Cengel, Y. a. *Introduction to Thermodynamics and Heat Transfer*; 2nd ed.; McGraw-Hill Education, 2008.
- (199) Gleeson, J.; Polcyn, A.; Gruner, S. Structure of Phospholipid Suspensions under Negative Pressure. *J. colloid interface* **1993**, 156, 430–432.
- (200) Larios, E.; Gruebele, M. Protein Stability at Negative Pressure. *Methods* **2010**, 52, 51–56.
- (201) Lemos, P.; Lutz, J. F. Soil Crusting and Some Factors Affecting It. *Soil Sci. Soc. Am. J.* **1957**, 21, 485–491.

